Spring 2023

The Extremes of Galaxy Formation & Evolution

Kelly E. Whalen
Dartmouth College, kelly.e.whalen.gr@dartmouth.edu

Recommended Citation

Whalen, Kelly E., "The Extremes of Galaxy Formation & Evolution" (2023). *Dartmouth College Ph.D Dissertations*. 192.
https://digitalcommons.dartmouth.edu/dissertations/192

THE EXTREMES OF GALAXY FORMATION & EVOLUTION

A Thesis
Submitted to the Faculty
in partial fulfillment of the requirements for the
degree of

Doctor of Philosophy

in

Physics and Astronomy

by Kelly E. Whalen

Guarini School of Graduate and Advanced Studies
Dartmouth College
Hanover, New Hampshire

April 2023

Examining Committee:

Ryan C. Hickox, Ph.D. (chair)

Burçin Mutlu-Pakdil, Ph.D.

John R. Thorstensen, Ph.D.

Aleksander Diamond-Stanic, Ph.D.

F. Jon Kull, Ph.D.
Dean of the Guarini School of Graduate and Advanced Studies

Abstract

Galaxy populations are shaped by the physical processes that regulate their star formation and central black hole growth throughout cosmic time. The primary aim of this thesis is to understand how these processes occur and how they shape evolution in some of the most extreme galaxies in the Universe including quasars, compact starbursts, and ultra-diffuse dwarfs. Gas-rich major mergers funnel large amounts of gas towards the nucleus, triggering rapid AGN accretion and compact star formation. In this work, I study powerful quasars and extreme, massive, compact starburst galaxies within the context of merger-driven galaxy evolution scenarios. One aim of this work was to place constraints on the nature of obscuration in AGN. Quasar clustering results suggest that obscured quasars reside in more massive dark matter halos than their unobscured counterparts. However, it is unclear if this discrepancy is tied to galaxy evolution processes, or is a result of other physical and selection effects. Here, I find that models that allow for obscuration to evolve on timescales typical of galaxy evolution are favored. Using similar modeling techniques, I also study a population of extremely compact, massive starburst galaxies that show extreme nuclear star formation and large-scale, energetic outflows. In order to make the first determination of their intrinsic space density, I construct a model population of these galaxies and assess the targeting criteria and selection effects to uncover the timescales over which these sources could be detected. The results indicate that extreme stellar feedback could be responsible for quenching a small but significant fraction of extremely star forming post-merger galaxies. Lastly, this work focuses on spectroscopy of ultra-diffuse galaxies (UDGs) with the Southern African Large Telescope (SALT). Understanding UDGs as a population could provide insight on how the faintest galaxies form and if weak stellar feedback could stunt the growth of what would be Milky Way-like galaxies. I use SALT to measure redshifts of UDG candidates to determine the effectiveness of selection techniques and add to the still small but growing known population of UDGs.

The light in the dark is the search
for the resolution.
— Jack's Mannequin

Preface

I am so grateful for all of the wonderful people in my life whose support has led to me completing my Ph.D. here at Dartmouth. I especially want to begin by saying that none of this would have been possible without the support and guidance of my advisor, Ryan Hickox. When I met with Ryan and his research group on my visit day in 2017, I immediately knew I wanted to work with him. However, there was one small problem; his reputation for being such a great advisor preceded him and his group was very oversubscribed. It was unclear if he would take new students during my first year. I decided to attend Dartmouth anyway in hopes that I could transfer into his group in my second or third year. That was one of the best choices I ever made, as I ended up being able to join his group upon my arrival. Ryan, thank you so much for taking me on my first year in spite of having a full research group. Thank you for all of the opportunities you have given me, including all of the meetings we have attended and all of the collaborators you have introduced to me. Thank you for not only being an intellectual role model, but for being an advisor who sees the humanity in all of his students. Lastly, thank you for recording an EP while in a band in the 2000s, it became the unofficial soundtrack for me applying to graduate school six years ago. I'm very happy to be staying in the AGN community to be able to continue to work in the same professional circles.

I also want to express my gratitude for all of the my other collaborators and professors who have supported me in this journey throughout the years. Thank you to my undergraduate advisor, Rose Finn, who encouraged me to start doing research with her as a freshman at Siena College. Rose was to first person to show me what a future in astronomy could look like, and I deeply appreciate the time and effort she spent on helping me take my first steps towards becoming the scientist I strive to be. Also, thank you to all of my wonderful collaborators in the HizEA compact starbursts group, especially to Alison Coil and John Moustakas who very kindly wrote tens of letters of recommendation for me during job application season, and to Aleks Diamond-Stanic who has taken the time to serve on this thesis committee. I have really enjoyed my time in this collaboration, and I hope to continue working with you all in the future.

Graduate school in the Upper Valley would not have been nearly as enjoyable if it weren't for all of the wonderful friends I've made along the way. I could not have gotten more lucky with my fellow PandA grads, past and present. I want to give a major shout out to my office 305 homies, Vivian Sabla, Avery Tishue, and (honorarily) Riley Chien. You guys have always brought immaculate vibes and I wouldn't have wanted anyone else to be my daily distraction. Crank the salt lamp, diffuse those essential oils, inflate the palm trees, sway in the beads, and most importantly hit the hype. I also have *no choice* but to stan all of the other incredible friends my time here has brought me including Nicki Loeven, Savannah Woolston, Corrie Shearin, Kate Fergusson, Jackson Yant, Ben Barto, plus the office 305 homies mentioned above. You have all made the Upper Valley feel like home to me and were truly the best people to have been quarantined with for over a year. I love you all so much. We need to twirl into it and hit up Lucky's when this is all over.

Last but certainly not least, I wouldn't be here without the love and support of my entire family, but especially my parents, Eileen and Tom Whalen. Thank you for always encouraging me to follow my dreams. Thank you so much for showing nothing but support to your seven year old daughter in an astronaut costume who said she wanted to work for NASA one day. You have done so much for me throughout my life and I cannot even begin to express the gratitude I have for you. I am so proud to have you as my parents. My love for you is as big as the Universe.

Contents

List of Tables

List of Figures

Chapter 1

Introduction

1.1 Galaxies and their central black holes

1.1.1 A diverse population of galaxies

Galaxies are collections of stars, gas, and dust, all gravitationally bound to each other within a larger dark matter halo. Characterizing the processes that allow for galaxies to form and change over cosmic time has been a widely studied field in astronomy for over a century. Although astronomers have been interested in the differences between galaxies for ages, it hasn't been until the dawn of wide-field optical and infrared surveys when galaxy evolution could be robustly probed on population level. Among the first galaxy surveys was the Smithsonian Astrophysical Observatory's (SAO's) Center for Astrophysics (CfA) galaxy redshift survey. Beginning in 1977 and generating a catalog of $\sim 2,200$ galaxies, the CfA redshift survey was revolutionary in enabling astronomers to map the positions of galaxies across the sky (e.g., Davis et al. 1982). By the turn of the millennium, galaxy surveys, such as the Sloan Digital Sky Survey (SDSS; York et al. 2000) and the Dark Energy Survey (DES; Dark Energy Survey Collaboration et al. 2016) have evolved to observe millions of targets. In the future, surveys such as the Vera Rubin Legacy Survey of Space and Time

(LSST; Ivezić et al. 2019), will be even deeper, allowing astronomers to peer earlier into the Universe to understand how some of the earliest galaxies have formed.

However as mentioned earlier, millions of galaxies across a wide range of redshifts have already been observed and cataloged. One interesting result of these wide-field galaxy surveys is that the distributions of various galaxy properties such as color, star formation rate (SFR), gas fraction, and morphology are bimodal out to $z \sim 3$ (e.g., Kauffmann et al. 2003a; Blanton et al. 2003; Baldry et al. 2004; Whitaker et al. 2011; see Figure 1.1). These various galaxy properties are typically correlated with each other, meaning that galaxies can broadly be placed into one of two populations. The first is a population of galaxies whose emitted light is dominated by young stars, making them blue in color. They are star forming, gas-rich, and have disk-dominated morphologies. The other population consists of galaxies with older stellar populations (red color) that are gas-poor, no longer star forming (quiescent), and bulge-dominated.

This distribution in galaxy properties has largely been interpreted as the result of galaxies existing along an evolutionary sequence in which blue, gas-rich, star forming disk galaxies undergo some process which can cease, or quench, star formation and disturb their morphologies, causing them to transition into red, gas-poor, bulge-dominated systems (e.g., Vulcani et al. 2015). The bimodality in these properties also highlights that the quenching likely occurs on timescales that are relatively short compared to that of the star forming and quiescent phases. (e.g., Nogueira-Cavalcante et al. 2018).

1.1.2 Active Galactic Nuclei

Diversity in galaxies can extend beyond differences in the properties of their stellar populations. Analyzing images and spectral energy distributions (SEDs) for large samples of galaxies show that the energy emitted from a fraction of them is dominated by a non-stellar

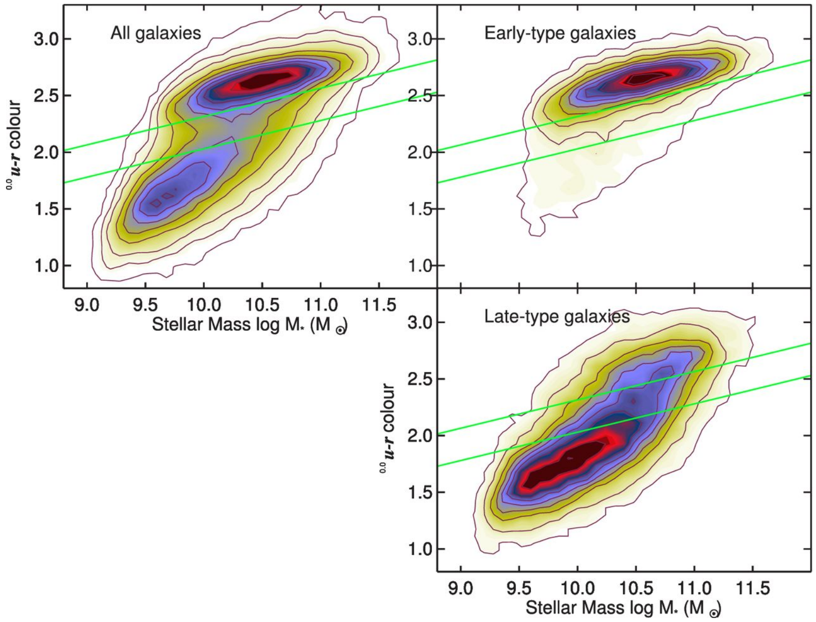

Figure 1.1 Color-stellar mass distribution for a population of low-redshift galaxies observed in SDSS. The top left panel contains the full sample, the top right just early-type, or bulge-dominated galaxies (“red cloud”), and the bottom right late-type, disk-dominated galaxies (“blue sequence”) This bimodality in galaxy properties is evident in observations as far back as $z \sim 3$. (Figure 2; Schawinski et al. 2014)

nuclear component. These galaxies are hosts to what are referred to as active galactic nuclei (AGN).

AGN are accreting supermassive black holes (SMBHs). SMBHs are ubiquitous in the centers of massive galaxies (e.g. Kormendy & Ho 2013). Characterizing how galaxies and their central black holes influence and evolve with one another is an active field of research that is important to understanding how observed populations of galaxies have formed. There are two main pathways through which SMBHs can grow; they can either coalesce with other galactic nuclei via mergers or they can gain mass via the accretion of nearby material (e.g. Alexander & Hickox 2012).

In the case of growth via accretion, material within the sphere of influence of the SMBH will be drawn towards the galactic nucleus. Due to conservation of angular momentum, this bulk of this infalling material will collapse to form a geometrically thin, optically thick

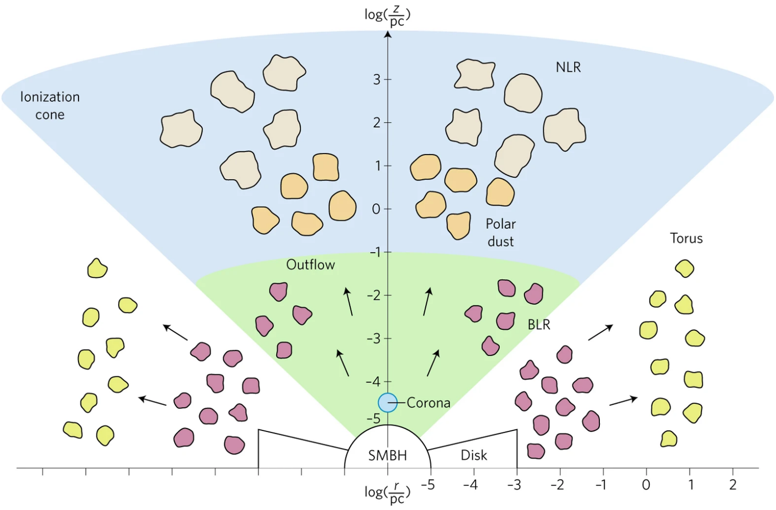

Figure 1.2 Schematic representation of the structure of a typical AGN. The AGN consists of a supermassive black hole being fed by a luminous accretion disk of material. Broad and narrow line-emitting gas clouds surround the black hole and accretion disk in nearby and outer regions of the AGN system, respectively. Out on $\sim 1 - 10$ parsec radii is a torus of gas and dust that can obscure the central accreting black hole and narrow-line region from an observer. (Figure 1; Ramos Almeida & Ricci 2017)

accretion disk that will feed the central black hole. Viscosity within the accretion disk thermally produces copious amounts of radiation across all wavelengths of the electromagnetic spectrum (e.g., Shakura & Sunyaev 1973), making accreting supermassive black holes, otherwise known as active galactic nuclei (AGN), among the most luminous objects in the universe. The innermost ~ 0.1 pc of the AGN is surrounded by clouds of broad line-emitting gas that is under gravitational influence of the central black hole (e.g. Peterson et al. 2004). Farther out on $\sim 1 - 10$ kpc scales, there are clouds of narrow-line emitting gas that have also been ionized by the AGN (e.g., Humphrey et al. 2015; Joh et al. 2021) The central AGN engine is also surrounded by geometrically and optically thick "dusty" tori on $\sim 1 - 10$ pc scales (e.g., Padovani et al. 2017; Hickox & Alexander 2018) AGN tori can potentially obscure radiation from the narrow-line region and the accretion disk along certain lines-of-sight to an observer. A schematic representation of this physical model for AGN can be seen in Figure 1.2.

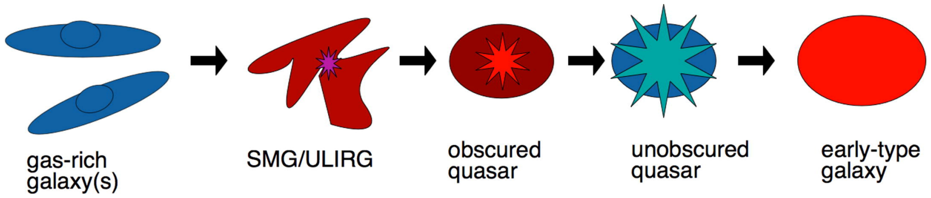

Figure 1.3 Schematic representation of a galaxy merger triggering obscured nuclear star formation and AGN activity. As the AGN more rapidly accretes, its luminosity increases, allowing it to rid the nuclear regions of obscuring material via radiative blowout, hence transitioning into an unobscured phase of its evolution. This scenario allows for statistical differences in the properties of obscured and unobscured AGN (Figure 6 of Alexander & Hickox 2012).

AGN host galaxies can be further sub-divided into narrower classifications based on differences in their observed spectral and photometric properties. Broadly speaking, there is a whole zoology of the various subtypes of AGN that can be observed. Many of the major differences between these subclasses can be attributed by the amount of obscuring material along a given line-of-sight to an observer. However, the nature of obscuration is not well understood (e.g., Ramos Almeida & Ricci 2017) One possibility is that obscuration is a line-of sight-orientation effect that is caused by an observer's random position relative to the axis-symmetric dusty torus (e.g., Antonucci 1993; Urry & Padovani 1995; Netzer 2015). There is also evidence that obscuration cold be a relatively short-lived phase along an evolutionary pathway in which a violent event, such as a galaxy merger, can funnel gas towards the nucleus of the galaxy, hence triggering increased AGN activity within a shroud of obscuring gas and dust. As the AGN grows more luminous, it can rid the nucleus of its obscuring material via radiative blowout (see Fig 1.3; Alexander & Hickox 2012). Chapter 2 of this dissertation directly addresses the nature of AGN obscuration.

1.1.3 How do galaxies quench?

As discussed in Section 1.1.1, bimodal distributions of galaxy properties suggest that the timescale over which galaxies have their star formation quenched is relatively short compared to the lifetime of a galaxy. Characterizing the processes that quench star formation and drive galaxy evolution is an active field of study in extragalactic astrophysics. In order for galaxies to form stars, dense clouds of cold molecular gas need to be able to collapse under their own gravity to ignite fusion (e.g., Krumholz & McKee 2005; McKee & Ostriker 2007). Disrupting or removing gas from star forming galaxies is essential to regulating their future star formation and initiating to their transition to quiescence.

It is possible that for some galaxies, star formation quenching is an externally driven process in which galaxies in high-density environments such as clusters have their gas stripped due to ram-pressure stripping or tidal interactions, thus rapidly shutting down star formation (e.g., Gunn & Gott 1972; Larson et al. 1980; Koopmann & Kenney 2004; Mihos 2004; van Gorkom 2004; Pérez-Millán et al. 2023). However, there are also galaxies with little to no ongoing star formation that exist in the field, suggesting that star formation quenching can be driven by internal processes such as active galactic nuclei (AGN) or stellar feedback (e.g. Springel et al. 2005b; Di Matteo et al. 2005).

1.2 The regulation of star formation via feedback

Generally, feedback has been shown to be necessary in cosmological galaxy formation simulations, as models that exclude it over-predict the present day baryon fraction and do not reproduce the local stellar mass function (SMF) (e.g., Moustakas et al. 2013; Hopkins et al. 2018). Feedback mechanisms in galaxies suppress star formation by injecting energy into the surrounding interstellar medium (ISM), preventing gas from cooling into dense star forming clouds or by expelling it altogether. The main drivers of feedback in galaxies are accreting supermassive black holes (SMBHs) at galactic centers and stellar processes.

1.2.1 AGN feedback

Generally, AGN feedback has been proposed to be the dominant mechanism for regulating star formation in massive galaxies (e.g., Davé et al. 2019) There are two primary modes of galaxy-scale AGN feedback; radiative and kinetic. Radiative feedback is also referred to as quasar-mode feedback because it occurs when the AGN is most efficiently accreting material and is highly luminous. When an AGN is in quasar mode, emitted photons are capable of exerting radiation pressure on surrounding electrons, gas, and dust, thus shocking ISM gas and driving winds. Winds that originate from the innermost regions of the AGN, such as the accretion disk or broad line region (BLR) can be classified as either "energy" or "momentum" driven depending on how quickly the thermal energy generated from shocks can be dissipated via radiation (e.g., King 2005; Ostriker et al. 2010; Choi et al. 2014) Either way, radiative feedback is capable of launching large-scale ($\sim$ tens of kpc), high-velocity ($\gtrsim 10^4$ km/s) outflows that can eject large amounts of multi-phase gas, thus rapidly quenching star formation (e.g., King & Pounds 2015).

Kinetic-mode AGN feedback becomes dominant when accretion onto the central SMBH slows and becomes radiatively inefficient. This mode of feedback is also known as "radio mode" or "jet mode" feedback, as the AGN is launching large-scale, highly collimated, relativistic jets (e.g., Fabian 2012; Heckman & Best 2014) While an AGN is in this state, the jets are energetically dominant over thermal emission from the accreting black hole. AGN jets are capable of interacting with material in a galaxy's halo as well as even the intracluster medium (ICM) for galaxies in high-density environments, as evident by radio galaxies often hosting bubbles visible in X-ray observation that indicate shocked gas on large spatial scales (e.g., Cattaneo et al. 2009; McNamara & Nulsen 2012a,b; Best et al. 2014) This suppresses star formation by heating what would otherwise be star forming gas. A schematic represntation of AGN driven feedback is given in Figure 1.4.

1.2.2 Stellar feedback

Stellar feedback has been shown to be a necessary ingredient in galaxy formation models, as simulations that do not include it tend to form galaxies ~ 10 times more massive than observed at a given redshift (e.g., Springel & Hernquist 2003; Hopkins et al. 2012). Like

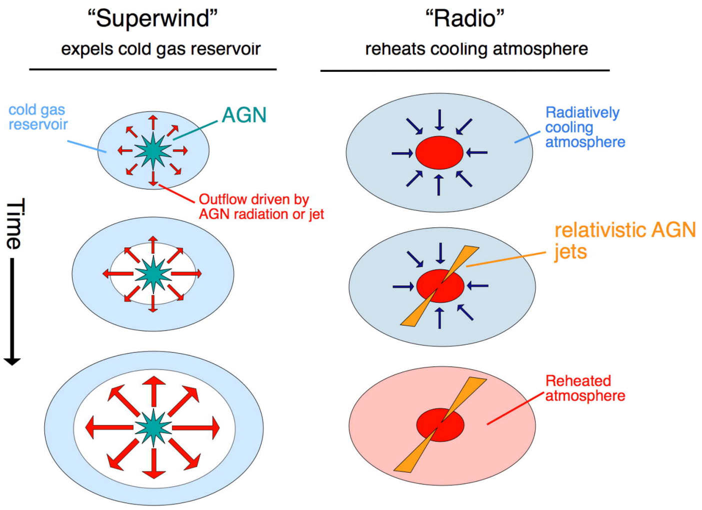

Figure 1.4 Schematic representation of the two types of AGN feedback. *Left panel:* Radiative AGN feedback in which winds originating in the accretion disk of broad-line emitting gas sweep up and shock the ISM, driving large-scale galactic winds and outflows. *Right panel:* Kinetic AGN feedback in which the kinetic energy of a relativistic jet being launched by an inefficiently accreting AGN heats the ISM and circumgalactic medium (CGM), preventing star formation (Figure 7; Alexander & Hickox 2012)

.

AGN feedback, stellar feedback can also be radiative or mechanical in nature. Short-lived, massive stars emit large amounts of ultraviolet (UV) radiation. In dusty star forming regions, this UV radiation can be absorbed by and impart radiation pressure on dust grains, thus initiating radiatively driven winds (e.g., Thompson et al. 2005; Murray et al. 2011; Raskutti et al. 2017). When these massive stars die, they will undergo core-collapse and explode as supernovae (SNe). A SN explosion can eject up to $\sim 10\ M_\odot$ of material and shock the surrounding ISM to induce mechanical outflows (e.g., Kim & Ostriker 2015; Zhang 2018).

Stellar feedback can effect star formation across a range of physical scales. On small (giant molecular cloud) scales, stellar feedback can slow the local star formation rate by decreasing the gas surface density in a region. This flattens out the faint end of the galaxy luminosity function in cosmological simulations, better matching observations (e.g., Heckman et al. 2000; Bertone et al. 2007). This is a form of preventative feedback. However, in order to achieve agreement between the simulated and observed high-mass end of the stellar mass function, strong, ejective feedback needs to be invoked either from AGN or star formation, consistent with the presence of large-scale, multi-phase winds in rapidly star forming and AGN host galaxies (e.g., Veilleux et al. 2005, 2020; Rupke 2018; Perrotta et al. 2021). For massive galaxies, this is strong feedback is typically attributed to AGN (e.g. Davé et al. 2019), but it is becoming increasingly clear that extreme star formation can play significant role in driving these powerful, ejective outflows (e.g., Gabor & Bournaud 2014; Harrison et al. 2018). Studies of rapidly star forming galaxies show that there is a correlation between star formation rate, morphological compactness, and outflow velocity (e.g., Heckman et al. 2015; Petter et al. 2020). Feedback from extremely compact, rapid star formation can be energetically consistent with driving galactic winds with speeds greater than the escape velocity, suggesting that stellar feedback can also impact the high-mass slope of the observed galaxy stellar mass function (e.g., Murray et al. 2011; Diamond-Stanic et al. 2012).

1.3 Constraints on stellar feedback with extreme galaxies

As mentioned in the previous section, stellar feedback is a process that is responsible for regulating star formation throughout diverse sets of galaxies. It is also a mechanism that can give insight as to how some of the most extrene galaxies form, from the faintest, most diffuse dwarfs, to extremely compact, massive starbursts. Being able to characterize galaxy formation for outlier populations of galaxies will uncover new aspects as to how feedback interacts with the ISM, giving better constraints on galaxy formation models in general.

One reason why outlier galaxies in the more “local” universe are important is that they can act as proxies for galaxies that were more common in the early universe but are not as readily observable. For example, understanding the assembly history of massive galaxies going back to the early universe is an open question in the field of galaxy formation. Observations of $z \gtrsim 1.5$ quiescent galaxies show that they are typically more compact than local galaxies of a similar mass by a factor of ~ 5 (e.g. Zirm et al. 2007; van Dokkum et al. 2008; van der

Wel et al. 2014). A proposed formation scenario for these galaxies is that their progenitors were compact star forming galaxies that were formed in gas-rich mergers of disk galaxies and were then rapidly quenched via dissipative feedback (e.g., Barro et al. 2013; Stefanon et al. 2013; van Dokkum et al. 2015b; see Figure 1.5). It is difficult to determine if this feedback was driven by AGN or rapid star formation since their high redshifts and large columns of obscuring dust make it nearly impossible to observe UV spectral signatures of outflows (e.g., van Dokkum et al. 2015b; Kocevski et al. 2017).

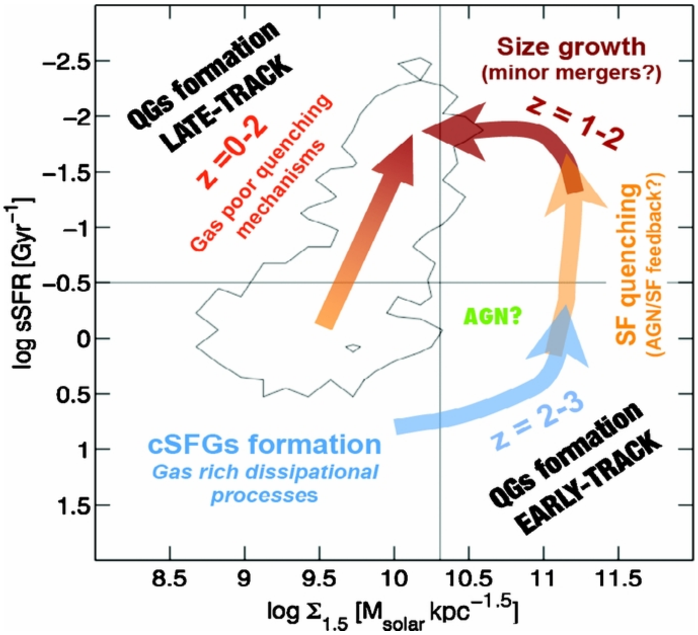

Figure 1.5 Hypothetical quenching pathway for a $z > 2$ compact star forming galaxy. This scheme suggests that many of the local Universe population of massive quiescent galaxies likely began as compact star forming galaxies that quickly quenched through dissipative feedback to form compact quiescent galaxies that would grow in size via gas-poor minor mergers (Figure 6; Barro et al. 2013)

.

Chapter 3 of this dissertation explores a "nearby" ($z \sim 0.5$) population of similarly massive, compact starburst galaxies (see Figure 1.6a) that could be local analogs to these galaxies more common at high-z. These local compact starburst galaxies provide us with a unique observational test space to understand strong feedback and its role in quenching some of the earliest massive galaxies, as they are nearby and bright enough to be able to directly observe outflow signatures.

Extreme galaxies are also important for constructing galaxy formation models as they provide new observable constraints. At the other star formation extreme are ultra-diffuse dwarf galaxies (UDGs). UDGs are the faintest low-surface brightness galaxies (LSBGs), with average surface brightnesses that are on the order of or below that of the ambient night sky (e.g. Impey et al. 1988). UDGs are especially unusual because they have stellar masses that would classify them as dwarfs ($\lesssim 10^8\ M_\odot$), but radii on the order of that of the Milky Way (e.g., van Dokkum et al. 2015a), an example of which can be seen in Figure 1.6b. The discrepancy between their stellar mass and half-light radii suggests that they are unable to efficiently form stars throughout the entirety of their stellar disks.

The recent discovery of UDGs provides galaxy formation models with a new population of galaxies whose properties they need to be able to reproduce. The formation mechanism behind UDGs is largely unknown, but the prevailing hypotheses are that they are either failed L_* galaxies that were gas-stripped at some point early in their lifetimes (e.g. van Dokkum et al. 2015a) or that are the victims of secular gas outflows driven by stellar winds, supernovae, or AGN feedback (e.g., Di Cintio et al. 2017). UDGs are preferentially found in groups and clusters, but they have also been detected in the field (e.g. Koda et al. 2015; van der Burg et al. 2016; Ruiz-Lara et al. 2018; Greco et al. 2018).

Understanding the formation of field UDGs in particular could be important for informing how disruptive stellar feedback is implemented in simulations, as it is more likely that their star formation is being regulated by internal processes. However, one major observational issue with UDGs is that their extreme faintness makes them very difficult to blindly detect in the field via wide-field surveys. Before we can characterize UDGs on a population level, we need to first construct a more statistically complete sample. In Chapter 4, I spectroscopically confirm a sample of UDGs to add to the known population. This will be able to help pave the way for more complete studies on their formation mechanisms and prevalence in the Universe.

1.4 Overview

The overarching aim of this work is to better understand the processes that regulate black hole and galaxy growth over cosmological timescales using some of the most extreme galaxies in the universe. In Chapter 2, I focus on forward modeling clustering measurements for populations of mid-infrared selected obscured and unobscured quasars at $z \sim 1$. This work suggests that quasar obscuration is a phase along an evolutionary pathway rather than being a random orientation effect relative to an observer. In Chapter 3, I incorporate modeling tools I developed in Chapter 2 to calculate an intrinsic space density for intermediate-z, extremely compact, massive starburst galaxies to place constraints on the importance of star formation feedback in quenching massive galaxies. In chapter 4, I present redshift measurements for a local population of ultra-puffy galaxy candidates, with the future aim of computing a luminosity function for these unique dwarfs. I summarize this thesis in Chapter 5, and I discuss my plans for continuing this work in the future.

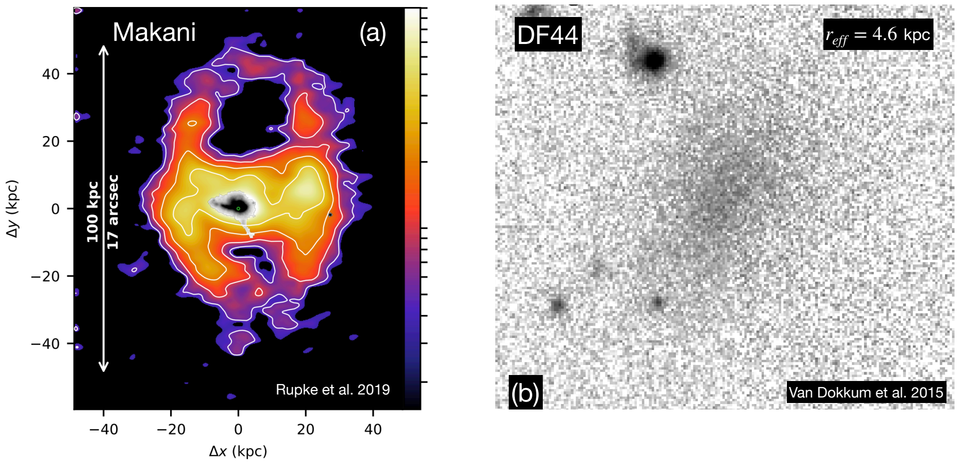

Figure 1.6 *Panel (a)*: Image of massive, compact starburst galaxy SDSS J211824.06+001729.4 (Makani) from Rupke et al. (2019). This galaxy's stellar core has an effective radius of ~ 400 pc and exhibits gas outflows with velocities > 1000 km s^{-1} that extend to ~ 40 kpc. *Panel (b)*: Optical image of ultra-diffuse galaxy DF44 from van Dokkum et al. (2015a). This galaxy has a surface brightness of $\mu \sim 24.5$ mag arcsec^{-1} over a radius of ~ 4.6 kpc.

Chapter 2

Physical Models for the Clustering of Obscured and Unobscured Quasars

Kelly E. Whalen (Dartmouth College), Ryan C. Hickox (Dartmouth College), Michael A. DiPompeo (Dartmouth College), Gordon T. Richards (Drexel University), Adam D. Myers (University of Wyoming)

This work first appeared in The Astrophysical Journal 2020, volume 888, page 71.

2.1 Introduction

Quasars, the highly luminous subclass of active galactic nuclei (AGN), are among the most energetic objects in the universe, and they are powered by supermassive black holes (SMBHs) that are rapidly accreting matter (e.g., Alexander & Hickox 2012). AGN are often characterized in optical observations by the presence of broad emission features in their spectra, as well as a luminous continuum at rest-frame ultraviolet and optical wavelengths (e.g., Baldwin 1977; Netzer 2015; Padovani et al. 2017). However, there are many observed AGN that appear to lack one or both of these features. Spectropolarimetric measurements have shown that these "missing" features are still present, but these photons have been scattered off of some obscuring material before they were observed (e.g., Antonucci & Miller 1985). This leads to understanding that quasars can be classified as either "obscured" or "unobscured." Here, we define a quasar as being obscured if it is shielded by a line-of-sight (LOS) column density ($N_{\rm H}$) of at least 10^{22} cm^{-2} (e.g. Usman et al. 2014; Hickox & Alexander 2018).

The simplest picture of quasar obscuration is that it is an effect due to quasars being randomly oriented relative to an observer. This model of unification by orientation (e.g., Antonucci 1993; Urry & Padovani 1995; Netzer 2015; Ramos Almeida & Ricci 2017) suggests that all AGN, including quasars, consist of a SMBH with an accretion disk and an axis-symmetric distribution of dust, also known as a "dusty torus." The non-spherical geometry of the dusty torus can obscure the nucleus of the AGN for some lines-of-sight, meaning that orientation alone could determine whether or not a quasar is obscured to an observer.

Constraints on this unified picture can be obtained through statistical measurements of the properties of large populations of quasars, both obscured and unobscured. A particularly useful measurable property is spatial clustering, which can determine the masses of the dark matter halos that host quasars and their connection to the large-scale environment, independent of the detailed properties of the individual host galaxies which can be difficult to measure for luminous AGN (e.g. Conroy & White 2013; Veale et al. 2014). Until recently, these measurements have focused on optically-selected unobscured sources or X-ray selected AGN (Croom et al. 2004; Richards et al. 2006; Myers et al. 2007; Shen et al. 2009; Ross et al. 2009; Eftekharzadeh et al. 2015). The dawn of deep, wide mid-infrared (IR) surveys has allowed us to better understand the environments of obscured quasars (e.g., Werner et al. 2004; Hickox et al. 2007, 2009; Wright et al. 2010; Krumpe et al. 2012; Hainline et al. 2014; DiPompeo et al. 2014, 2016a, 2017a). With a large sample of mid-IR selected obscured quasars, we can perform statistical analyses to determine if obscured and unobscured quasars are fundamentally different from one another. For unobscured quasars, spatial clustering measurements have shown that their parent dark matter halo masses are roughly constant across a a redshift range of $0 < z < 5$ (e.g., Croom et al. 2005; Myers et al. 2007; Shen et al. 2007; Coil et al. 2007; da Ângela et al. 2008; Ross et al. 2009; Hickox et al. 2011; Powell et al. 2018). For obscured quasars selected by the *Wide-field Infrared Survey Explorer* (*WISE*) (e.g., Wright et al. 2010), it has been measured that for a given redshift, obscured quasars typically reside in higher mass dark matter halos than their unobscured counterparts (e.g., Hickox et al. 2011; Donoso et al. 2014; DiPompeo et al. 2014, 2016a, 2017a; Powell et al. 2018). For this paper, we will adopt recent measurements from DiPompeo et al. (2017a) that indicate obscured quasars reside in dark matter halos that have an average mass of $\log M_{\rm halo}/M_{\odot} = 12.94^{+0.10}_{-0.11}$, while unobscured quasars on average reside in dark matter halos of $\log M_{\rm halo}/M_{\odot} = 12.49^{+0.08}_{-0.08}$.[1] These results provide observational constraints for any model that tries to explain the relationship between obscured and unobscured quasars.

In contrast with the simplest cases of the unified model of AGN, quasar obscuration may be a phase in an evolutionary scenario that occurs on timescales of roughly a Salpeter

---

[1] We note that DiPompeo et al. (2017a) defined quasar obscuration using an optical/mid-IR color cut of $r - W2 = 6$ (Vega) (e.g., Hickox et al. 2007, 2017) This cut takes advantage of the fact that obscured and unobscured quasars occupy different parts of SDSS/*WISE* color space (e.g., Hickox et al. 2007). Hickox et al. (2017) showed that SED models are able to predict optical/mid-IR colors for obscured and unobscured quasars that are consistent with observations. The color cut used in DiPompeo et al. (2017a) corresponds to the output of Hickox et al. (2017) SED model that assumed $A_V = 20$. Based on equation (3) in Draine (2003), this gives $N_{\rm H} \sim 3.7 \times 10^{22}$ cm^{-2}, which is consistent with our adopted definition of quasar obscuration.

(*e*-folding) time for black hole growth at Eddington-limited accretion. This obscuration phase can be associated with dust structures produced during major galaxy mergers (e.g., Silk & Rees 1998; Springel et al. 2005a; Hopkins et al. 2006; Goulding et al. 2012; Treister et al. 2012; Blecha et al. 2018), or it can also be tied to an early phase in a quasar's lifetime at which it is not luminous enough to rid its nucleus of obscuring material (e.g., Hopkins et al. 2008; King 2010).

Many evolutionary models postulate that as dark matter halos grow, black hole growth lags behind (e.g., Alexander et al. 2008; Woo et al. 2008; Kormendy & Ho 2013; DiPompeo et al. 2017b). As these black holes grow in mass, they transition from an obscured phase to an unobscured phase via radiatively-driven blowout (e.g., Hopkins et al. 2006, 2008). DiPompeo et al. (2017b) presented a simple evolutionary model in which black hole growth lagged behind galaxy growth. In the DiPompeo et al. (2017b) model, the host dark matter halo grows continuously, while the black hole grows in brief episodes. Here, the black hole's change in mass determines the quasar's evolution from obscuration to being unobscured. Hickox et al. (2007, 2011) showed that bolometric luminosities were similar for populations of obscured and unobscured quasars selected in the mid-IR with *Spitzer Space Telescope* (Werner et al. 2004). Since luminosity is just a function of Eddington ratio and black hole mass, assuming similar Eddington ratio distributions implies that both unobscured and obscured quasars of a given luminosity should have the same black hole mass, independent of obscuration. In this model, a black hole will begin to grow if it falls too far off the $M_* - M_{\rm BH}$ relation. As the black hole gains mass, the quasar will become luminous enough to rid its nucleus of some obscuring material, and it will then transition from an obscured to an unobscured stage in its evolution. Because the black hole masses of obscured quasars are similar to that of their unobscured counterparts, their dark matter halo masses are predicted to be larger, which is what is empirically seen.

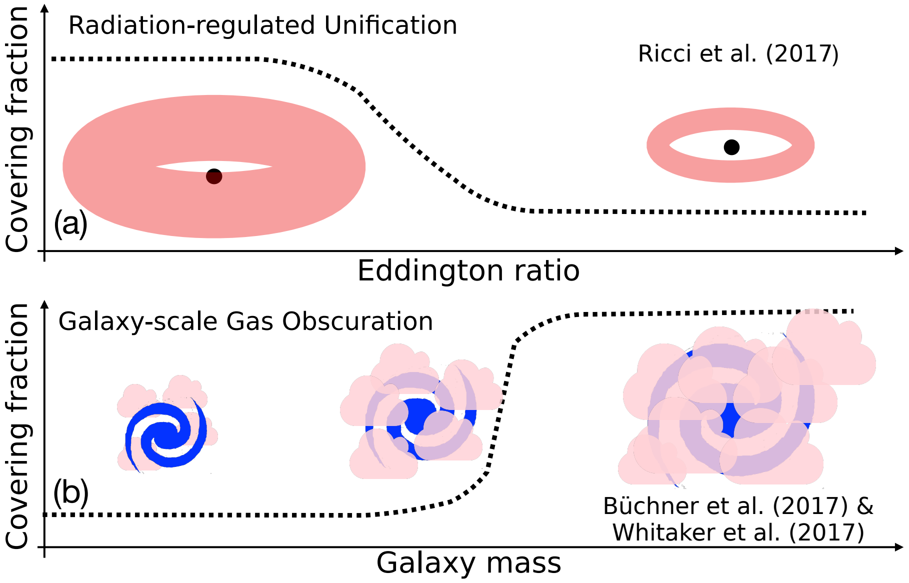

Figure 2.1 *Panel (a)*: Schematic of radiation-regulated unification (Ricci et al. 2017). Studies of X-ray selected AGN show that there is a possible relationship between an AGN's covering fraction and its Eddington ratio. Quasars accreting at high fractions of their Eddington luminosities could blow away some of their obscuring, dusty-tori via increased radiative pressure, producing a lower fraction of obscured quasars at higher Eddington ratios. *Panel (b)*: Schematic of galaxy-scale gas obscuration (Buchner et al. 2017; Pannella et al. 2009). Empirical relationships between $N_{\rm H}$/covering fraction and galaxy stellar mass have been presented in which less massive galaxies host less obscuring gas than their more massive counterparts. We study these scenarios as possible causes for the mass difference seen in clustering measurements of mid-IR selcted quasars.

However, it is unclear if modeling obscuration as an evolutionary stage is the only way to be able to reproduce the difference in average dark matter halo mass ($M_{\rm halo}$) between obscured and unobscured quasars. Although the simplest iterations of the unified model are inconsistent with clustering measurements, the dusty torus clearly plays an important role in quasar obscuration (e.g., Netzer 2015; Ricci et al. 2017; Hickox & Alexander 2018). Ricci et al. (2017) showed that radiative feedback from an AGN could allow for the expulsion of nuclear obscuring dust, thus reducing the number of obscured lines-of-sight between the quasar and observer. Since the amount of radiation pressure exerted on the torus is dependent on the quasar's Eddington ratio ($\lambda_{\rm Edd}$), it is possible that $\lambda_{\rm Edd}$ is driving quasar obscuration. The top panel of Figure 2.1 shows a schematic of "radiation-regulated unification," in which $\lambda_{\rm Edd}$ determines how much of the quasar is covered by nuclear gas and dust.

It is also possible that quasar obscuration could be taking place in regions outside of the host galaxy's nucleus, but is not associated with a specific galaxy's evolutionary stage. Buchner et al. (2017) analyzed the X-ray afterglows of extragalactic long-duration ($>$ 2s) Gamma ray bursts (LGRBs) to derive host galaxy gas column densities. From this, they determined a relationship between the stellar mass of a host galaxy and its gas column density in which more massive galaxies have larger average $N_{\rm H}$, thus more of a probability of obscuring a central quasar. Pannella et al. (2009) and Whitaker et al. (2017) found a similar dependence on the fraction of obscured star formation on host galaxy stellar mass. Since star formation in massive galaxies is being obscured by interstellar gas and dust, it may be expected that a central quasar would also be obscured. A schematic of galaxy-scale obscuration is shown in the bottom panel of Figure 2.1.

In this work, we test these simple models of radiation-regulated unification and galaxy-scale obscuration to determine if they can generate populations of simulated quasars that are consistent with observations of mid-IR selected quasars. We also probe the effect that a luminosity cut that is representative of the limits of *WISE* has on the M_{halo} of our simulated obscured and unobscured quasar populations.

Definitions to frequently used terms are given in Table 2.1. We adopt a cosmology of $H_0 = 70.2$ kms^{-1}Mpc^{-1}, $\Omega_M = \Omega_{CDM} + \Omega_b = 0.229 + 0.046 = 0.275$, and $\Omega_\Lambda = 0.725$ (Komatsu et al. 2011).

2.2 The Models

In this section we describe how we construct our simple models of quasar obscuration based on known halo mass and λ_{Edd} distributions, as well as empirical relationships between obscuring fraction and λ_{Edd} and obscuring fraction and host galaxy stellar mass.

2.2.1 Generating the Quasar Sample

We begin by generating a model population of 10 million dark matter halos randomly and uniformly distributed in logarithmic space in the mass range, $10^{10}\ M_\odot < M_{\text{halo}} < 10^{16}\ M_\odot$. Each of these sample halos was assigned a weight using the $z = 1$ halo mass function (HMF) detailed in Tinker et al. (2010) so that each halo's contribution to the total average is proportional to the space density of halos of that mass. We used a CAMB (Lewis et al. 2000) generated matter power spectrum to compute the HMF. Weighting our uniformly and randomly distributed sample of host halos by the HMF eliminates shot noise in our simulated data. This is because that even though our rare, high mass halos will have a small contribution to the average host halo mass, they are still equally as numerous in our simulation as their low mass counterparts.

Table 2.1 Definitions of terms used throughout this work.

Term	Definition
Obscured quasar	Quasar that is shielded by LOS $N_{\text{H}} \gtrsim 10^{22}$ cm^{-2} (e.g., Usman et al. 2014; Hickox & Alexander 2018).
Covering fraction (f_{cov})	Probability of an observer having an obscured LOS to a quasar based on the physical distribution of obscuring material. (e.g., Ricci et al. 2017)
Obscured fraction (f_{obsc})	Fraction of quasars in a given population that are obscured.

Once we produced a weighted sample of halos across a wide mass range, we calculated the stellar masses of their corresponding galaxies using the $z = 1$ halo mass-stellar mass relationship presented in Moster et al. (2010). The distribution of our simulation galaxies in stellar mass-space is consistent with observed $z \sim 1$ stellar mass functions (e.g., Pérez-González et al. 2008; Behroozi et al. 2010). We then calculated the masses of the central black holes of each galaxy with the stellar mass-black hole mass relationship detailed in Häring & Rix (2004). Again, we find that the black hole mass distribution of our simulated quasars is broadly consistent with observed black hole mass functions (e.g., Shankar et al. 2009; Kelly & Merloni 2012). There is intrinsic scatter in both the halo mass-stellar mass and stellar mass-black hole mass relationships, so we included these effects in our models. We adopted an intrinsic scatter of 0.2 dex for the halo mass-stellar mass and 0.3 dex for the stellar mass-black hole mass relationships (Häring & Rix 2004; Moster et al. 2010).

We generated a separate sample of 10 million Eddington ratios that are randomly and uniformly distributed in logarithmic space in the range, $-4 < \log \lambda_{\rm Edd} < 1$. Just as we assigned weights to each dark matter halo based on the HMF, we also assigned weights to each $\lambda_{\rm Edd}$ that correspond to the double power law-$\lambda_{\rm Edd}$ distribution presented in Jones et al. (2019) to limit the contribution of rare, high Eddington systems to the overall distribution. The overall probability of a halo of a given mass containing a quasar accreting at a particular $\lambda_{\rm Edd}$ is the product of the HMF and the $\lambda_{\rm Edd}$ distribution function.

Although we can use this treatment to generate quasars of all luminosities, observational surveys are limited by their capabilities to detect faint sources. Our model therefore needs to include a lower luminosity limit so we can match our quasar distributions to observations. We first calculate the bolometric luminosities for all of our generated quasars. Since we are interested in mid-IR selected quasars, we implement a luminosity threshold that is representative of the detection limits of *WISE*. Bolometric luminosities for *WISE*-selected quasars at $z = 1$ are typically greater than 10^{46} erg s^{-1} (e.g., Hickox et al. 2007; Assef et al.

2013), so we impose a luminosity limit of $10^{45.8}$ erg s^{-1} following DiPompeo et al. (2017b) unless otherwise stated.

2.2.2 Identifying Obscured Sources

Creating obscured and unobscured populations of quasars from the simulated sample requires us to adopt a model that parameterizes obscuration as a function of one of the physical properties of either the quasars or their host galaxies. Broad band observations of quasars can tell us whether or not a given source is obscured (e.g., Merloni et al. 2014), but they do not necessarily yield information on what scale the light emitted from the quasar is being absorbed. We first assume that our quasars are being obscured by their dusty tori, and adopt the radiation-regulated unification model in which obscuration is parameterized by the $\lambda_{\rm Edd}$ of our quasars (Ricci et al. 2017). For galaxy-scale interstellar material, we parameterize obscuration as a function of host galaxy stellar mass (Pannella et al. 2009; Buchner et al. 2017; Whitaker et al. 2017). We also present a model that allows our simulated quasars to be obscured by both, their tori and the interstellar material in their host galaxies. In what follows, we describe the details of each model.

2.2.2.1 Radiation-regulated Unification Model

Ricci et al. (2017) presented the relationship between the covering fractions of AGN and their $\lambda_{\rm Edd}$. This relationship was derived from a multi-wavelength study of 836 AGN identified by the *Swift*/Bat X-ray survey (e.g., Gehrels et al. 2004; Barthelmy et al. 2005; Krimm et al. 2013; Baumgartner et al. 2013). We used the observed relationship shown in in Figure 4 of Ricci et al. (2017) to model a population of obscured and unobscured AGN where the obscured fraction depends on $\lambda_{\rm Edd}$. We chose to use this relationship over the one detailed in Figure 1 of Ricci et al. (2017) to account for the existence of Compton-thick material that might obscure the most highly accreting quasars. Although this was originally presented for AGN at $z \sim 0.1$, we expect it to hold for our model at $z = 1$. Observations of high redshift quasars have shown that there is not much evolution over cosmic time on the $\lesssim 1$ parcsec scale at which radiation-regulated feedback would be significant (e.g., Fan 2006; Lusso & Risaliti 2016).

The data bins used in Ricci et al. (2017) to average covering fractions at a given $\lambda_{\rm Edd}$ were broad, so we made this relationship more continuous over a range of $\lambda_{\rm Edd}$ by fitting a series of error functions to the original data, as seen in Figure 2.2. Each fit corresponds to varying the minimum $f_{\rm cov}$ for high accreting quasars (the covering fractions in the Compton-thick regime are not well constrained). The grey, shaded region in Figure 2.2 represents the errors on the $f_{\rm cov} - \log \lambda_{\rm Edd}$ relationship shown in Figure 4 of Ricci et al. (2017). Using these $f_{\rm cov} - \log \lambda_{\rm Edd}$ relationships, we then randomly assigned the quasars to obscured and unobscured populations. We do this by assigning each quasar a random number between zero and one. If this number is less than or equal to $f_{\rm cov}$ at a quasar's $\lambda_{\rm Edd}$, then it is classified as obscured. Otherwise, it is classified as unobscured.

We also note that for some populations of quasars at higher redshifts that it is possible for the accretion disk to have a "slim disk" geometry in which the accretion disk is puffed up for the quasars that are accreting at high-$\lambda_{\rm Edd}$ (e.g., Frank et al. 2002; Leighly 2004; Luo et al. 2015). The thin disk is geometrically thin and optically thick, so in principle this could contribute to obscuration in addition to the dusty-torus. As for the $f_{\rm cov} - \lambda_{\rm Edd}$ relationships in Figure 2.2, this effect would increase $f_{\rm cov}$ again at high-$\lambda_{\rm Edd}$. We consider the effect of slim-accretion disk geometries below, but this scenario is more applicable for luminous quasars at $z \sim 2$ than the population we are simulating (e.g., Netzer & Trakhtenbrot 2014).

2.2.2.2 Galaxy-Scale Obscuration

The radiation-regulated unification model assumes that the quasars are being obscured by the parsec-scale dusty torus, and that the $\lambda_{\rm Edd}$ of the quasar could change the covering fraction of the torus. However, toroidal dust is not the only obscuring material in front of

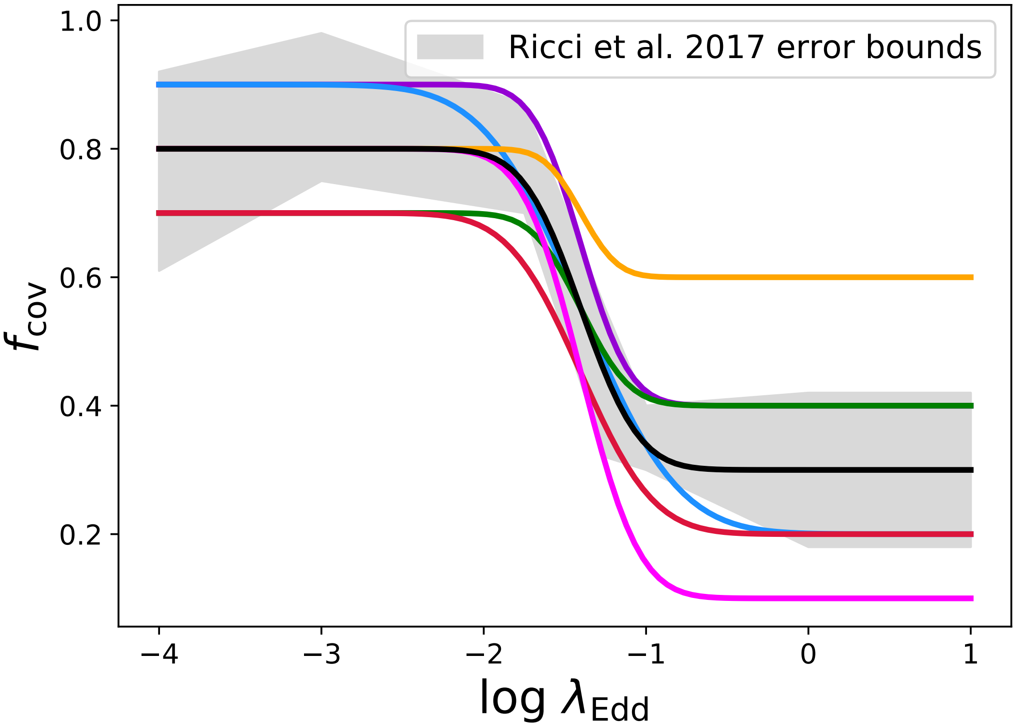

Figure 2.2 Relationship between covering fraction and $\lambda_{\rm Edd}$ for the radiation-regulated unification model presented in Ricci et al. (2017). The error bounds from Figure 4a in Ricci et al. (2017) are shown in grey. We modeled this relationship as error functions that spanned the parameter space occupied by the error bounds in Ricci et al. (2017). We also included 2 model fits that fall outside of the Ricci et al. (2017) error bounds to account for the uncertainty on the Compton-thick fraction.

the quasar along the LOS of an observer. Interstellar gas and dust within a galaxy could have the ability to obscure a quasar at the galactic center (e.g., Hickox & Alexander 2018). Buchner et al. (2017) measured the attenuation of X-ray afterglows from extragalactic LGRBs to derive an empirical relationship between the mean column densities of gas in galaxes and their stellar masses. This relationship shows that more massive galaxies contain deeper obscuring columns of gas. Knowing the $N_{\rm H}$ of gas in galaxies can allow us to determine the likelihood of obscuration for a given quasar. Buchner & Bauer (2017) used the $\log\ N_{\rm H} - \log\ M_*$ relationship derived in Buchner et al. (2017) to construct a simple model of obscuring covering fractions for AGN. Here, we study this model to determine if it is capable of recreating clustering measurements of mid-IR selected quasars.

We start by using the GRB-derived $\log\ N_{\rm H} - \log\ M_*$ relationship from Buchner et al. (2017) to assign each of our simulated galaxies a mean $N_{\rm H}$. We assume that the assigned $N_{\rm H}$ is the mean of a column density probability distribution. Here, we use a Gaussian probability density function with $\sigma = 0.5$, as well as a 1 degree-of-freedom Student's t-distribution. The Student's t-distribution acts as a proxy for the broader, less peaked SingleEllipse model detailed in Buchner et al. (2017) since the two models have a similar analytic form (private communication; J. Buchner). X-ray selected AGN are typically detected as obscured when $N_{\rm H} > 10^{22}$ cm^{-2} (e.g. Predehl & Schmitt 1995; Burtscher et al. 2016; Schnorr-Müller et al. 2016), and this generally corresponds to the $N_{\rm H}$ of mid-IR selected quasars (e.g., Hickox et al. 2007; Usman et al. 2014). We convert the mean column densities from the $\log N_{\rm H} - \log M_*$ relationships to effective covering fractions by integrating each of the $N_{\rm H}$ probability density functions on the interval $10^{22} < N_{\rm H}/\text{cm}^{-2} < \infty$, as depicted in Figure 2.3. The covering fraction-stellar mass relationships derived using the Gaussian and Student's t-distributions are shown as the blue and red curves in Figure 2.4, respectively.

In addition to the GRB X-ray afterglow attenuation-derived models described above, we also calculated a $f_{\rm cov} - \log M_*$ relationship based on the galaxy mass dependence of the

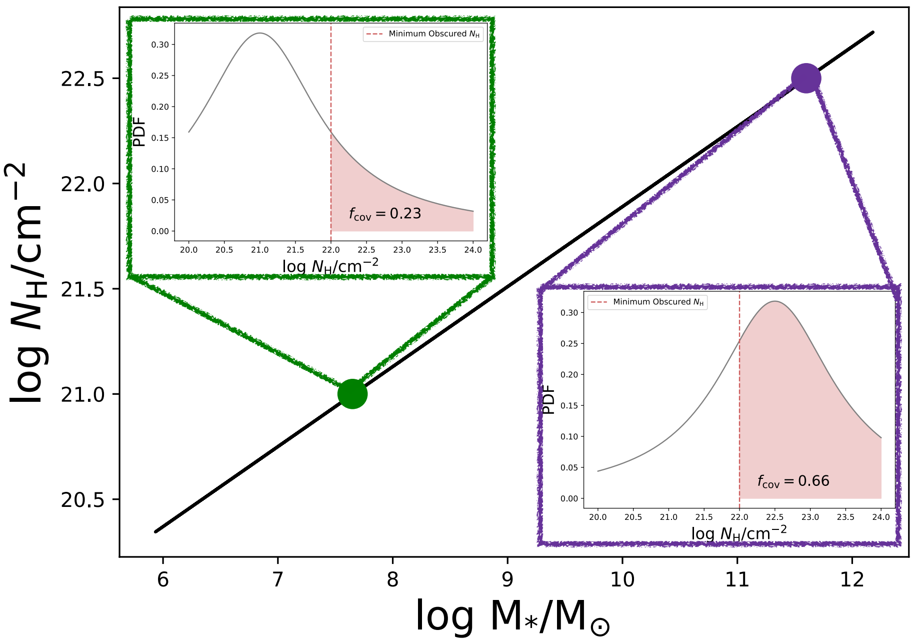

Figure 2.3 Schematic of how covering fractions are calculated from assigned $N_{\rm H}$ values. Each galaxy is assigned a mean $N_{\rm H}$ based on its M_*. Each galaxy's mean $N_{\rm H}$ is then used as the mean of a column density probability density function (PDF) that is then integrated on the interval $10^{22} < N_{\rm H}/{\rm cm}^{-2} < \infty$ to determine covering fraction at each given M_*.

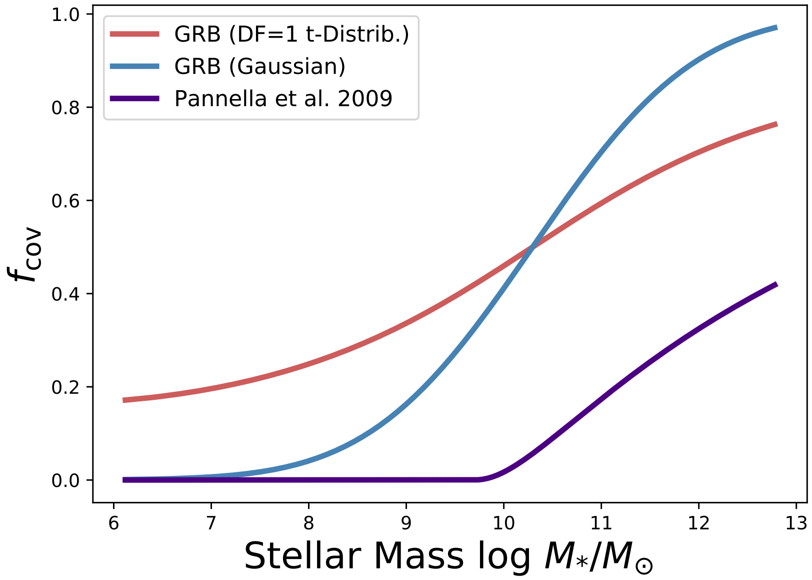

Figure 2.4 Relationships between covering fraction and host galaxy stellar mass. Using the mean $N_{\rm H}$ at a given stellar mass, we calculated covering fractions as detailed in Section 2.2.2.2. These relationships are used to produce model populations of obscured and unobscured quasars based on obscuration by galaxy scale gas.

fraction obscured star formation in galaxies presented in Whitaker et al. (2017). The simple assumption here is that the material obscuring star formation in these galaxies will similarly obscure quasar activity. Pannella et al. (2009) presented a relationship between ultraviolet (UV) attenuation and stellar mass. We utilized this relationship to derive LOS column densities as a function of stellar mass since it is unclear how the fraction of obscured star formation in a galaxy relates to the physical dust distribution. Whitaker et al. (2017) showed that the obscured star formation fractions derived from the Pannella et al. (2009) relationship were consistent with what they calculated from IR and UV star formation rates.

We convert the Pannella et al. (2009) UV attenuation-stellar mass relationship to a column density-stellar mass relationship by assuming $R(V) = 3.1$ (Milky Way) extinction curve (e.g., Fitzpatrick 1999; Draine 2003). At 1500 Å, this corresponds to $A_{1500}/N_{\rm H} = 1.6 \times 10^{-21}\frac{\rm cm^2 mag}{\rm H}$. We note that the UV attenuation-stellar mass relationship in Pannella et al. (2009) is fitted over a much smaller stellar mass range than included in our simulated sample. However, once we enact a luminosity threshold, only $\sim$12% of our sources fall outside the Pannella et al. (2009) stellar mass range, and of those sources $\sim$88% fall within 0.3 dex of the fitted mass range, so we are confident in the extrapolation of this relationship. We then compute a $f_{\rm cov} - M_*$ relationship using the same methodology as done with the models derived from the attenuation of GRB X-ray afterglows.

2.3 Results

Our models need to be able to recover the following observational constraints: (1) the host $M_{\rm halo}$ for our simulated obscured and unobscured quasars, as well as (2) the fraction of obscured quasars. The measured average host $M_{\rm halo}$ of obscured and unobscured quasars are $\log M_{\rm halo}/M_\odot = 12.94^{+0.10}_{-0.11}$ and $\log M_{\rm halo}/M_\odot = 12.49^{+0.08}_{-0.08}$, respectively (e.g., DiPompeo et al. 2017a). The range of observed obscured fractions for luminous quasars is roughly between 30% (Treister et al. 2008) and 65% (Polletta et al. 2008), with significant uncertainty on the heavily obscured (Compton-thick) population (e.g., DiPompeo et al. 2016b; Yan et al. 2019). We note that we adopt such a broad observed obscured fraction to reflect the uncertainty due to the difficulty of detecting heavily-obscured AGN. This is a conservative estimate that provides a broad parameter space in which our models could be potentially viable.

2.3.1 Radiation-regulated Unification Model

As seen above in Figure 2.2, we modeled radiation-regulated unification as a series of error functions within the $f_{\text{cov}} - \lambda_{\text{Edd}}$ parameter space covered by the error bounds of the relationship shown in Figure 4a of Ricci et al. (2017). We also included two parameterizations that were well above and below the error bounds to account for the uncertainty in the Compton-thick fraction of quasars. We calculated f_{obsc} for each of these models and found that f_{obsc} is roughly equal to the value of f_{cov} at high-λ_{Edd}. This is because the luminosity cut pushes the mean of the underlying Eddington ratio distribution to be $\log\langle\lambda_{\text{Edd}}\rangle \approx 0$. Since there is little dynamic range in f_{cov} at high-λ_{Edd}, f_{obsc} becomes the assigned high-λ_{Edd} f_{cov} value. The implication of this on our simulated populations is that only the three parameterizations with high-λ_{Edd} $f_{\text{cov}} \geq 0.3$ satisfy f_{obsc} constraints. In what follows, we focus on the model fit (shown in black in Figure 2.2) that is the mean of the Ricci et al. (2017) error bounds. We use this relationship since it produced a population of quasars whose f_{obsc} falls on the edge of the observed obscured fraction range, as well as that it best represents the results presented in Ricci et al. (2017).

For this $f_{\text{cov}} - \log \lambda_{\text{Edd}}$ relationship, we examined the λ_{Edd} and host M_{halo} distributions for the generated obscured and unobscured populations of quasars. Figure 2.5 presents the full λ_{Edd} distribution for our simulated quasars as well as the distribution after a luminosity cut of $10^{45.8}$ erg s^{-1} has been applied (e.g., DiPompeo et al. 2017b). Initially, there is an intrinsic difference between the shapes of the obscured and unobscured λ_{Edd} distributions. As expected, the unobscured population has a higher mean λ_{Edd} than its obscured counterpart

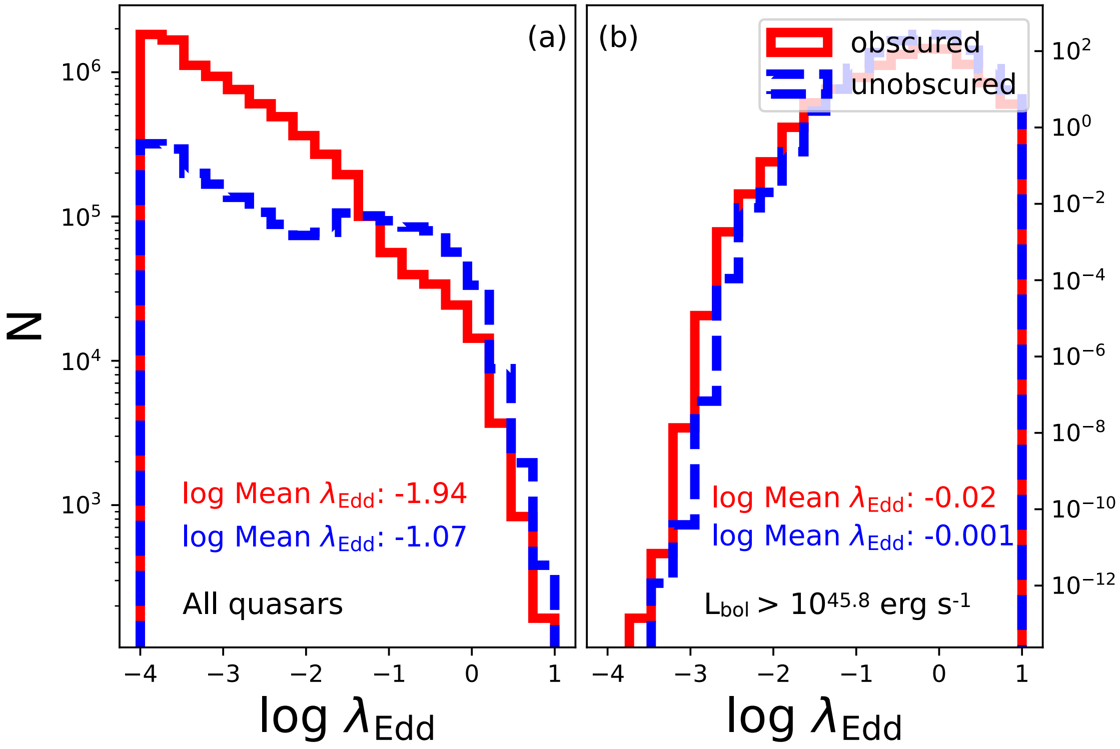

Figure 2.5 *Panel (a)*: The full weighted distributions of $\lambda_{\rm Edd}$ for our simulated quasars generated using the mean of the Ricci et al. (2017) error bounds on $f_{\rm cov} - \log \lambda_{\rm Edd}$ (black curve in Figure 2.2). Obscured quasars are shown in red bins, and unobscured quasars in blue. There is an intrinsic difference in the $\lambda_{\rm Edd}$ distributions between the obscured and unobscured populations of quasars due to the fact that the chosen $f_{\rm cov} - \log \lambda_{\rm Edd}$ relationship preferentially obscures low-$\lambda_{\rm Edd}$ quasars. *Panel (b)*: The distribution of $\lambda_{\rm Edd}$ after a luminosity cut of $10^{45.8}$erg s^{-1}, corresponding to *WISE*-selected quasars. (e.g., DiPompeo et al. 2017b). The luminosity cut causes our model to exclude the low-$\lambda_{\rm Edd}$ end of our initial distributions, thus pushing our populations to become increasingly similar.

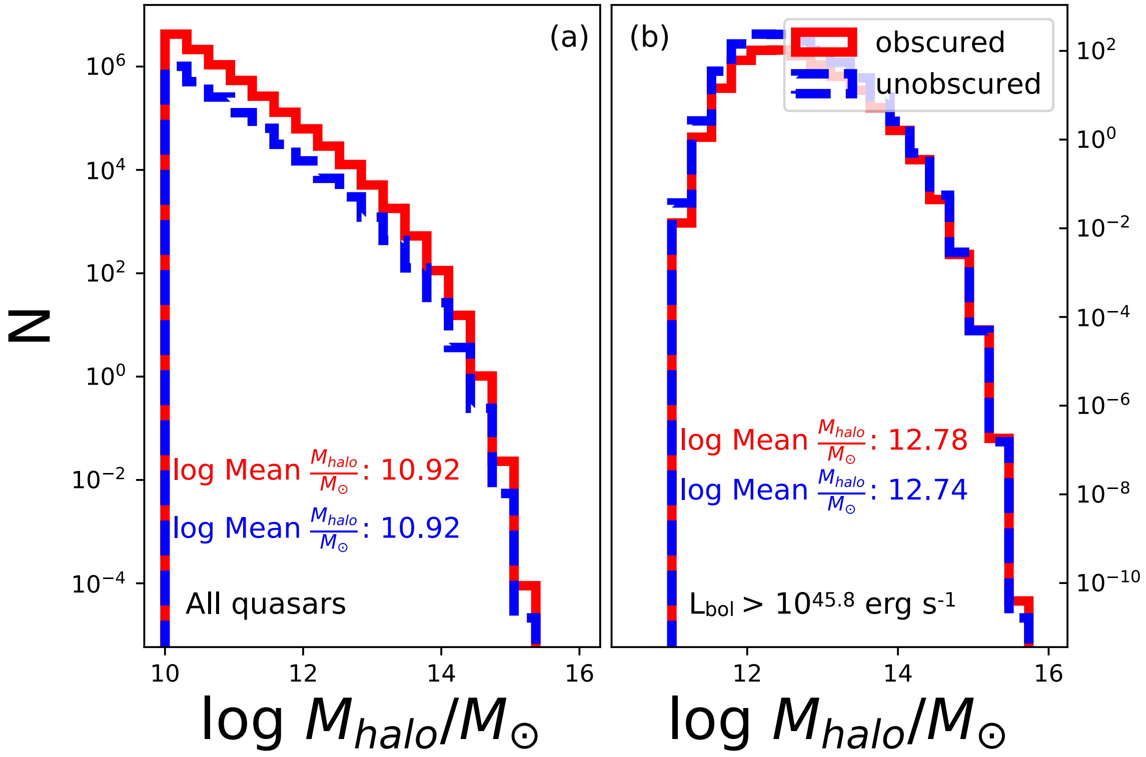

Figure 2.6 *Panel (a)*: The full weighted distributions of host M_{halo} for our simulated quasars generated using the mean of the Ricci et al. (2017) error bounds on $f_{\text{cov}} - \log \lambda_{\text{Edd}}$ (black curve in Figure 2.2). Obscured quasars are shown in red bins, and unobscured quasars in blue. *Panel (b)*: The distributions of host M_{halo} for our sample quasars after a luminosity cut of $10^{45.8}$erg s^{-1}, corresponding to *WISE*-selected quasars. (e.g., DiPompeo et al. 2017b). The obscured and unobscured populations have the same mean M_{halo} before the luminosity cut, and only a negligible post-cut difference that falls outside of our observational constraint on mean M_{halo}.

due to the fact that the shape of the $f_{\mathrm{cov}} - \log \lambda_{\mathrm{Edd}}$ distribution dictates that low-λ_{Edd} quasars have a higher probability of being obscured. However, applying a lower luminosity limit causes us to lose the low-λ_{Edd} end where the two populations are the most distinct from one another. This effectively makes the mean λ_{Edd} identical for the populations of obscured and unobscured quasars.

Figure 2.6 shows the corresponding host M_{halo} distributions. In this model, obscuration is independent of host M_{halo}, so our distributions for the full populations of simulated obscured and unobscured quasars are identical. The initial f_{obsc} for the full sample is 78%, dropping to 29% for the luminosity cut; thus removing a significant number of our obscured quasars that reside in low-mass dark matter halos. The removal of obscured quasars in low mass halos results in a small difference between the average host M_{halo} for the obscured and unobscured populations, but it is still well outside of our observational constraints.

We next carry out this analysis for all of the parameterizations of our radiation-regulated unification model, as seen in Figure 2.2. Just as we calculated the fraction of obscured quasars for each $f_{\mathrm{cov}} - \log \lambda_{\mathrm{Edd}}$ relationship, we also calculated mean host M_{halo} for the generated populations of obscured and unobscured quasars. These are presented in Figure 2.7. The red and blue shaded regions show the uncertainty for the measured mean M_{halo} for mid-IR selected obscured and unobscured quasars, respectively (DiPompeo et al. 2017a). We find that as we increase the covering fraction at high-λ_{Edd}, the mean M_{halo} for obscured and unobscured quasars become increasingly similar. Increasing the covering factor for high-λ_{Edd} sources at a given luminosity threshold allows for more low-mass, high-λ_{Edd} quasars to be classified as obscured. For a luminosity cut of $10^{45.8}$ erg s^{-1}, there is nowhere in this parameter space that satisfies both the mass difference and obscured fraction observational constraints.

Following DiPompeo et al. (2017b), we probed the effect the luminosity cut had on our simulated quasar populations. For the population of quasars generated from the minimum

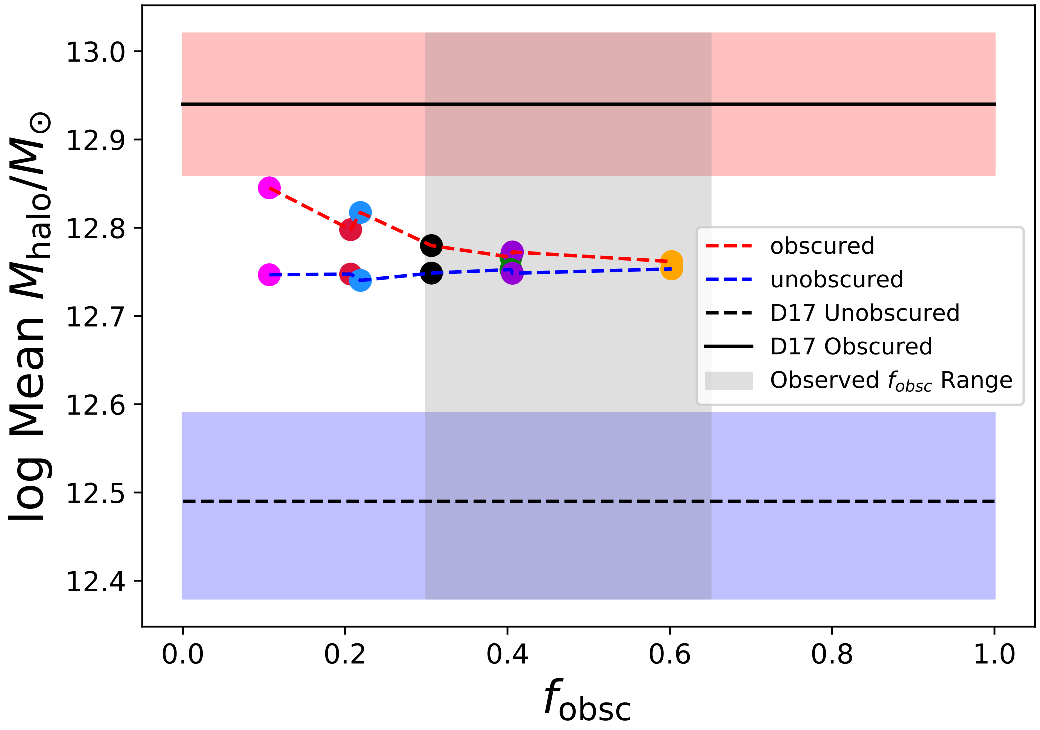

Figure 2.7 The calculated mean halo masses for simulated quasar populations generated using different error function fits to the $f_{\rm cov} - \log \lambda_{\rm Edd}$ relationship as seen in Figure 2.2. The solid, black line shows the measured mean halo mass of a population of observed obscured quasars (e.g., DiPompeo et al. 2017a), where the red, shaded region shows the error on that measurement. This is also the case for the black, dashed line, and the blue, shaded region, but for the unobscured population studied in DiPompeo et al. (2017a). Each point corresponds to the populations generated using the model of the same color in Figure 2.2. The points connected by the red (blue), dashed line are the average obscured (unobscured) host halo masses. The radiation-regulated unification model is unable to recover both the disparity in $M_{\rm halo}$ between obscured and unobscured quasars and an obscured fraction that falls within the range of observations.

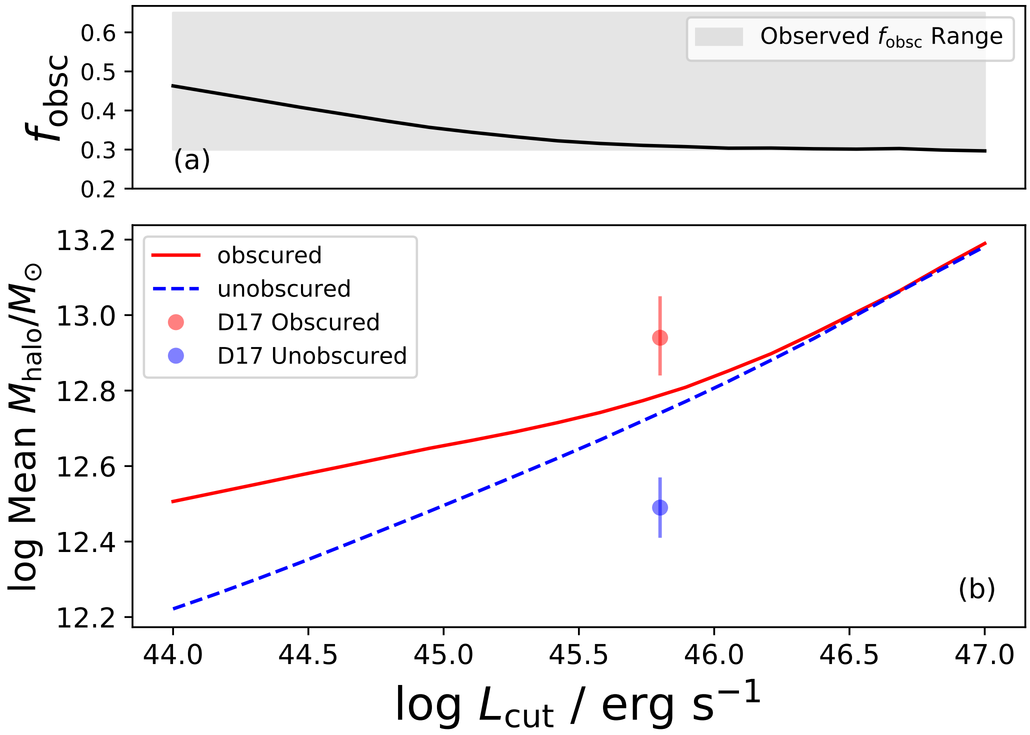

Figure 2.8 *Panel (a)*: The obscured fraction of our sample population modeled from the yellow curve in Figure 2.2 as a function of the luminosity threshold for the radiation-regulated unification model. At every luminosity limit, the obscured fraction resides within the range of observed obscured fractions. *Panel (b)*: The relationship between the weighted mean $M_{\rm halo}$ of the distribution as a function of the luminosity threshold. The obscured sample is depicted by the solid, red line, and the unobscured is depicted by the dashed, blue line. It is apparent that the choice in luminosity limit affects the disparity between the mean $M_{\rm halo}$ for obscured and unobscured quasars, but it does not reproduce observations.

$f_{\text{cov}} = 0.3$ model, we find that as the luminosity cut increases, the mean M_{halo} for the obscured and unobscured populations converge. Increasing the minimum detectable luminosity effectively pushes our sample to be comprised of quasars that are either accreting at higher λ_{Edd} or residing in higher mass dark matter halos. As also shown in Figures 2.5 and 2.6, increasing the lower luminosity limit excludes the low-Eddington end of our quasar populations where their λ_{Edd} distributions are most distinct from one another. Our model is able to produce a ~ 0.3 dex difference in M_{halo} for obscured and unobscured quasars at low luminosity cuts (around 10^{44} erg s^{-1}), which is still even smaller than the observed difference shown in DiPompeo et al. (2017a). This is shown in Figure 2.8. Overall, the difference between simulated M_{halo} for our obscured and unobscured populations fall significantly below observations.

As mentioned earlier at the end of Section 2.2.2.1, we also considered the effect of obscuration due to a slim accretion disk at high-λ_{Edd}. We did this by implementing a linear increase of f_{cov} starting at $\log \lambda_{\text{Edd}} = 0$ such that a quasar with $\log \lambda_{\text{Edd}} = 1$ has a covering fraction of 1. We found that implementing a slim accretion disk to the model with minimum $f_{\text{cov}} = 0.3$ mildly decreased the average M_{halo} for our obscured population of quasars, making it identical to the average unobscured quasar dark matter halo mass. The average M_{halo} for the simulated obscured and unobscured quasars are both $\log M_{\text{halo}}/M_{\odot} = 12.75$. This, in addition to the fact slim accretion disks are also more often found in luminous, $z \sim 2$ AGN rather than in the $z \sim 1$ quasar populations we are modeling (e.g., Netzer & Trakhtenbrot 2014), shows us that this model is not viable for recreating mid-IR quasar clustering measurements.

2.3.2 Galaxy-scale Gas Obscuration

Here, we conduct a similar analysis as for the radiation-regulated unification model, instead assuming the obscurer is galaxy-scale gas, to determine if this model could satisfy observational constraints.

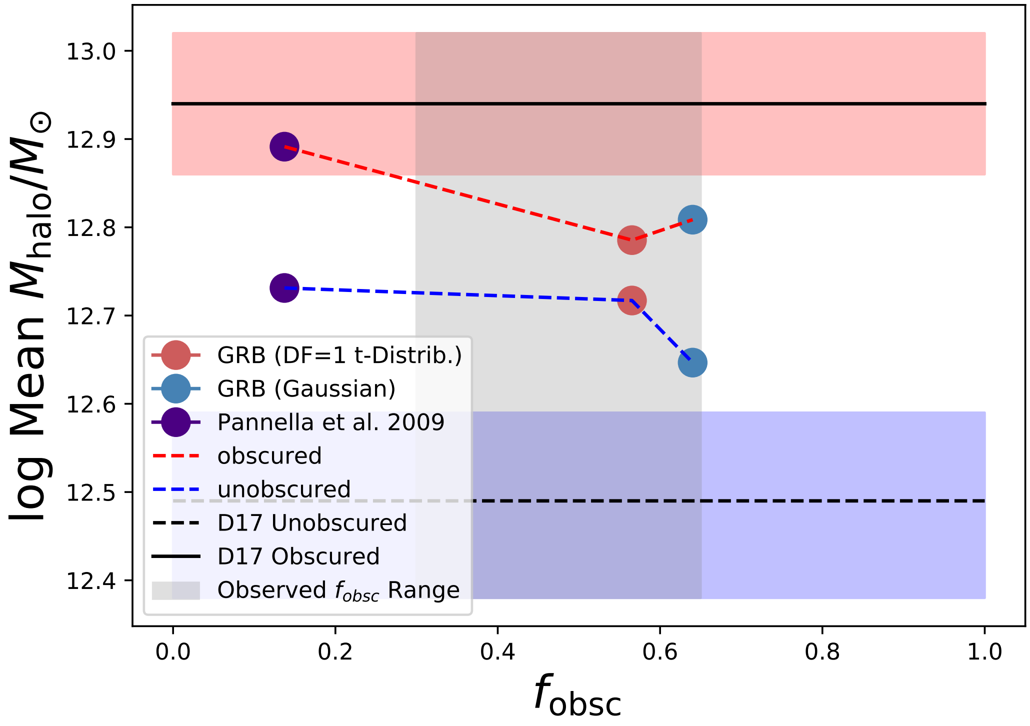

Figure 2.9 The calculated mean $M_{\rm halo}$ for simulated quasar populations generated using $f_{\rm cov} - \log M_*$
relationships as seen in Figure 2.4. The red (blue), dashed line connects the average host halo mass for the obscured (unobscured) population generated from the $f_{\rm cov} - \log M_*$ of the same color from Figure 2.4. The solid, black line shows the measured mean $M_{\rm halo}$ of a population of observed obscured quasars (e.g., DiPompeo et al. 2017a), where the red, shaded regions show the errors on that measurement. This is also the case for the black, dashed line, and the blue, shaded region, but for the unobscured population studied in DiPompeo et al. (2017a). Although these models are able to drive small differences in average $M_{\rm halo}$ for obscured and unobscured quasars, they do not satisfy observational constraints.

As before, we calculated obscured fractions and mean M_{halo} values for the populations of quasars that were generated using the various $f_{\text{cov}} - \log M_*$ relationships shown in Figure 2.4. The calculated obscured fraction for each $f_{\text{cov}} - \log M_*$ relationship is shown as the x-axis of Figure 2.9. It is apparent that two of the $f_{\text{cov}} - \log M_*$ relationships produced populations of quasars that were more highly obscured than what has been observed since the points for these models fall outside of the grey box that depicts the range of observed obscured fractions. For a quasar to be luminous enough to be detectable using mid-IR color selection, it would have to be rapidly accreting or host a massive black hole. Since we are considering the galaxy stellar mass-dependent model here as well as scaling relationships between $M_{\text{BH}} - M_*$, the quasars that would be detectable in this model will typically reside in galaxies with large stellar masses. Since the $f_{\text{cov}} - \log M_*$ relationships in Figure 2.4 state that more massive galaxies have a higher probability of obscuring the central quasar, this results in the populations of quasars generated with the Gaussian Buchner et al. (2017) inspired-model to have a higher obscured fraction than observed. The mean M_{halo} values are shown as the y-axis in Figure 2.9. Much like what occurred in the results of the radiation-regulated unification model, we find that the weighted mean parent M_{halo} for all of the $f_{\text{cov}} - \log M_*$ relationships fall outside of the range of clustering measurements which is shown by the red (blue) shaded region for observed obscured (unobscured) sources.

Figure 2.10 shows our GRB-derived Gaussian galaxy-scale gas obscuration model's dependence on luminosity cut. We chose this model because it produced a f_{obsc} that fell on the edge of observational constraints as well as having a modest difference between M_{halo} of its obscured and unobscured quasar populations. The intrinsic M_{halo} distributions created by the galaxy-scale gas models are most different from one another at low-M_{halo}. Once again, a higher luminosity cut results in sampling a region in the original M_{halo} distribution where the obscured and unobscured distributions are almost indistinguishable. It is clear that modeling a quasar's obscuration as a function of its host galaxy's stellar mass is not sufficient

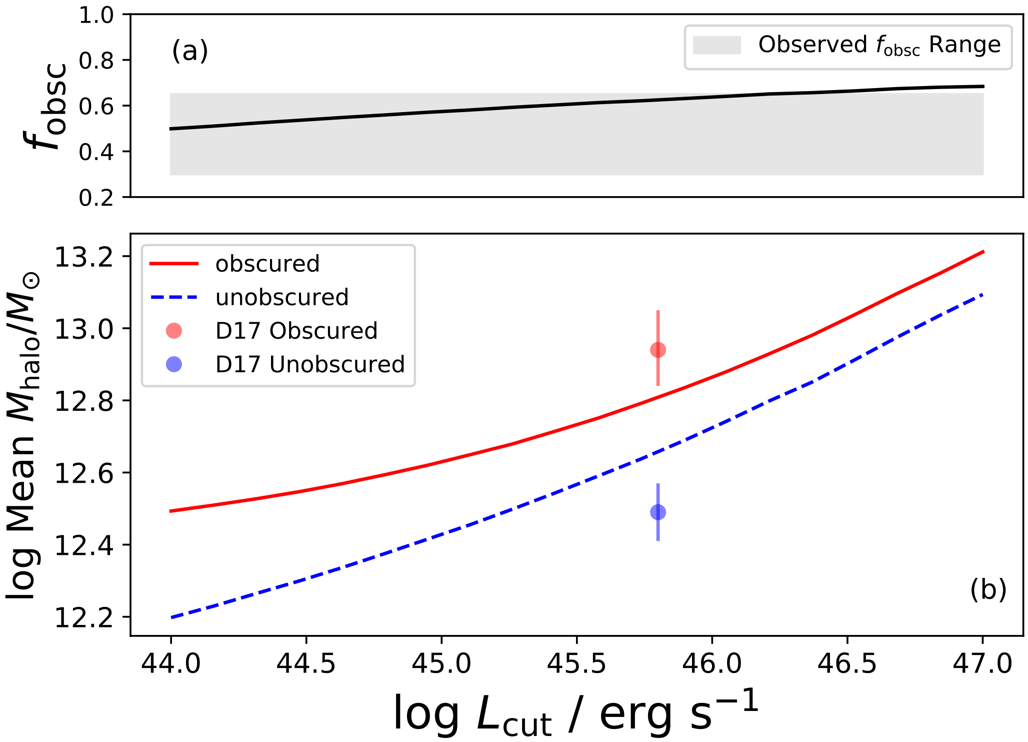

Figure 2.10 *Panel (a)*: The obscured fraction for the populations of quasars generated at each varying luminosity threshold for the observed GRB-derived Gaussian galaxy-scale dust model of obscuration (as shown in blue in Figure 2.4 and thereafter). *Panel (b)*: The relationship between the mean $M_{\rm halo}$ of our obscured (red, solid curve) and unobscured (blue, dashed curve) populations and luminosity threshold. For this obscuration model, the choice in luminosity limit minimally affects the disparity between the mean $M_{\rm halo}$ for obscured and unobscured quasars, but it does not reproduce observations.

to properly recover clustering measurements of parent $M_{\rm halo}$ as well as the observed quasar obscured fraction.

2.3.3 Combining Nuclear and Galaxy-scale Obscuration

Both of the models discussed above assume that obscuration is coming from material *either* within the region closest to the quasar or within the interstellar regions of the host galaxy. We next consider that there could be many possible lines-of-sight in which the obscuring material is independently contributed by both, the nuclear-scale torus and the galaxy-scale gas and dust. Here, we adopt a $\log N_{\rm H} - \log \lambda_{\rm Edd}$ relationship from Ricci et al. (2017) to assign our quasars nuclear column densities. We then sum the nuclear and the Buchner et al. (2017)-assigned galaxy-scale column densities to obtain a mean LOS column density for each of the sources in our simulated sample. Utilizing the same methodology described above in Section 2.2.2.2, these mean LOS column densities are treated as the mean of a Gaussian PDF that is integrated on the interval $10^{22} < N_{\rm H}/{\rm cm}^{-2} < \infty$ to obtain a LOS covering fraction for each quasar. We again randomly assign our quasars into obscured and unobscured populations based on their calculated covering fractions. We find that after applying the luminosity cut, the mean $M_{\rm halo}$ for the obscured and unobscured populations are $\log M_{\rm halo}/M_{\odot} = 12.79$ and $\log M_{\rm halo}/M_{\odot} = 12.65$, respectively, and that $f_{\rm obsc} = 0.75$. This model overpredicts the number of obscured quasars in this population, and it is unable to reproduce the magnitude of the mass discrepancy between the host halos of obscured and unobscured quasars. It is possible that torus and galaxy-scale obscuration (as modeled here) can contribute to this observed host mass difference to some degree, but cannot reproduce the observational results. This suggests that evolutionary models in which obscuration is an earlier stage in the lifetime of the quasar may be necessary to recover observed properties of mid-IR selected quasars.

2.3.4 The Effects of Uncertainty

Here, we address the various sources of uncertainty in our models as well as their effects on our results.

2.3.4.1 Uncertainty in Scaling Relationships

There is a degree of uncertainty inherent in the relationships that allowed us to convert our simulated $M_{\rm halo}$ into galaxy stellar masses, and then into black hole masses (e.g., Moster et al. 2010; Häring & Rix 2004). These uncertainties get propagated through each conversion, and they are exacerbated by the fact that these uncertainties are higher for the relationships at $z = 1$ than in the local universe (e.g., Häring & Rix 2004; Guo et al. 2010; Moster et al. 2010; Behroozi et al. 2010; Lamastra et al. 2010). There is also uncertainty in the observed stellar mass and black hole mass functions out at higher redshifts (Kelly & Merloni 2012; Kormendy & Ho 2013). To account for possible effects of uncertainty in the black hole masses at $z = 1$, we probed the effect of shifting our black hole masses by ± 0.5 dex for our radiation-regulated unification and galaxy-scale gas obscuration models, in accordance with the maximum error propagated through scaling relationships, as estimated in Kelly & Merloni (2012). This shift in black hole mass for our simulated quasars effectively changes the number of quasars that can be detectable after a luminosity cut is enacted, thus changing the shape of the mass distributions of our obscured and unobscured quasars.

The results for this analysis are presented in Table 2.2. Shifting the black hole masses of our sample by ± 0.5 dex did not have a strong impact on the obscured fractions for any of our models. However, since shifting our black hole masses effectively changed our luminosity cut, there was a noticeable difference in the calculated obscured and unobscured mean $M_{\rm halo}$. On average, shifting our black hole masses by -0.5 dex pushed all of the obscured and unobscured quasars to reside in more massive halos since we essentially excluded any quasars that were initially on the cusp of the luminosity cutoff. For all of the models, the

Table 2.2 The effect of shifting black hole masses of our modeled quasars

Model	$\log M_{\rm BH}/M_\odot$ Shift (dex)	Obscured Mean ($\log M_{\rm halo}/M_\odot$)	Unobscured Mean ($\log M_{\rm halo}/M_\odot$)	$f_{\rm obsc}$
Radiation-regulated	-0.5	12.94	12.92	0.27
	0.0	12.80	12.75	0.28
	+0.5	12.70	12.59	0.30
Galaxy-scale (Pannella)	-0.5	13.03	12.90	0.16
	0.0	12.91	12.75	0.14
	+0.5	12.80	12.59	0.12
Galaxy-scale (GRB Gauss.)	-0.5	12.97	12.83	0.67
	0.0	12.82	12.65	0.63
	+0.5	12.65	12.57	0.61
Galaxy-scale (GRB *t*-dist)	-0.5	12.96	12.90	0.58
	0.0	12.79	12.72	0.56
	+0.5	12.77	12.71	0.57
Nuclear + Galaxy	-0.5	12.94	12.83	0.77
	0.0	12.79	12.65	0.75
	+0.5	12.66	12.48	0.73

shift in black hole mass of -0.5 dex produced populations of quasars whose host dark matter halos are more massive than observed, as well as obscured and unobscured populations that reside in dark matter halos of similar masses. When we shifted our black hole masses by +0.5 dex, we allowed more of our quasars to survive the luminosity cut applied. This shift had the effect of lowering the mean $M_{\rm halo}$ for all of the obscured and unobscured populations of quasars that our models generated. Even though the mass difference between each of the obscured and unobscured populations is greater than that of the original, unshifted populations, all of the mean dark matter halos for the obscured quasars fall below that of clustering measurements.

Overall, we find that even with this systematic shift in black hole masses, our models are unable to satisfy all of the observational constraints.

2.3.4.2 Uncertainty in Covering Fraction Parameterizations

As shown above in Figure 2.2, there are formal uncertainties on the $f_{\text{cov}} - \log \lambda_{\text{Edd}}$ relationship presented in Ricci et al. (2017). In our primary analysis, we mostly considered the effect of the highly uncertain Compton-thick fraction on our models. This is because the *WISE* luminosity limit eliminates the low-λ_{Edd} quasars from our sample (as seen in Figure 2.5), so only differences in f_{cov} at high-λ_{Edd} should affect our simulated sample. However, for completeness we also explored the entire parameter space occupied by the error bounds on the original Ricci et al. (2017) relationship. We tested models that had low-λ_{Edd} covering fractions towards the high end and the low end of the formal error bounds as well as at the same at the high-λ_{Edd} end of the relationship. We found that none of our models that spanned the range of the Ricci et al. (2017) error bounds were able to drive significant differences between the mean halo masses of the obscured and unobscured quasar populations. The obscured fraction of quasars for most of these populations also fell below the observed obscured fraction range.

We similarly addressed the possible uncertainty in the $f_{\text{cov}} - \log M_*$ relationships by varying the parameterizations to cover the parameter space between the Student's t-distribution-derived and Gaussian PDF-derived covering fraction curves, similar to what is shown in Figure 2.2 for the radiation-regulated unification model. We did this to account for the fact that the shape of the underlying N_{H} PDF is uncertain. We again find that there is nowhere in this parameter space that can simultaneously satify observational constraints on the dark matter halo masses for the obscured and unobscured quasars and the obscured fraction.

2.3.5 Implications for Evolution

In this work, we have explored various simple models that attempt to recover the clustering measurements of mid-IR selected quasars by characterizing quasar obscuration as a function of either λ_{Edd} or host galaxy stellar mass. We found that these models could either satisfy dark matter halo mass measurements or the observed obscured fraction, but not both. This result strongly implies that evolution needs to be incorporated in quasar obscuration models to be able to understand the observed halo mass difference between obscured and unobscured populations of quasars.

One commonly invoked picture of quasar evolution is that quasar activity is triggered by a dramatic event such as a merger or disk instability. The quasar then remains active in an obscured state until it rids itself of obscuring material via radiative and mechanical feedback to become unobscured (e.g., Sanders et al. 1988; Di Matteo et al. 2005; Hopkins et al. 2008; Alexander & Hickox 2012; DiPompeo et al. 2017b; Hickox & Alexander 2018). Qualitatively, treating the effective obscuring covering fraction as a function of time in a quasar's evolution provides a simple explanation for the fact that obscured and unobscured quasars have different observed properties such as host dark matter halo mass. DiPompeo et al. (2017b) quantitatively showed that this evolutionary sequence is able to recreate clustering measurements. The key piece to evolutionary models is understanding the timescales at which the host galaxy and the quasar/black hole evolve. The model presented in DiPompeo et al. (2017b) assumed coevolution between the host galaxy and the black hole, but the black hole grew in spurts and its growth lagged behind that of the galaxy. The implication of this is that obscured quasars host black holes that are undermassive relative to what would be expected based on their host galaxy masses. This effect coupled with a luminosity threshold is enough to drive a difference in the average host dark matter halo mass between populations of obscured and unobscured quasars. Although it has been shown that the dusty-torus does exist and that it can obscure a quasar along certain lines of sight, any torus-obscuration model needs to consider a time-dependence on the $M_* - M_{\rm BH}$ relationship to be able to properly recreate observations.

Separate from host galaxy or black hole properties, Powell et al. (2018) discussed the potential role of assembly bias and environment on the dark matter halo mass discrepancy between obscured and unobscured quasars. For a population of $z \sim 0.1$, X-ray selected AGN, the model presented in DiPompeo et al. (2017b) predicted a much smaller host halo mass difference than measured. Powell et al. (2018) argued that this implies that assembly bias, in which unobscured AGN reside in more recently formed halos, could be driving a physical difference in AGN clustering. This is distinct from observed clustering differences arising as a selection effect due to the limiting luminosities of surveys. This interpretation also considers a time-dependence on obscuration, albeit on a different time scale than that in DiPompeo et al. (2017b). Both assembly bias and event-driven evolution scenarios are viable to explain the observed clustering difference in mid-IR selected quasars on their own or in conjunction with a torus/galaxy-scale obscuration model.

2.4 Summary and Conclusions

Observational studies of quasars have shown that obscured quasars preferentially reside in higher mass dark matter halos; a result that contradicts the simplest models of unification by orientation (e.g., Hickox et al. 2011; Donoso et al. 2014; DiPompeo et al. 2014, 2016a, 2017a). Recent results presented for Compton-thin AGN in Ricci et al. (2017) showed a strong relationship between the covering factor of an AGN's torus and its λ_{Edd}. Using this empirical relationship along with known M_{halo} and λ_{Edd} distributions, we constructed a simple model that sought to recreate the M_{halo} difference for obscured and unobscured quasars as seen in mid-IR quasar clustering measurements. We find that our model of radiation-regulated unification is not able to recreate clustering measurements while also producing samples of quasars that have an obscured fraction that falls within observations.

Using relationships between host galaxy gas content and stellar mass as presented in Buchner et al. (2017) and Pannella et al. (2009), it was also possible to model quasar obscuration as a function of its host galaxy's stellar mass. We find that although some of these models were able to produce host M_{halo} that fell within the range of clustering measurements, they are not viable since the obscured fractions for these populations were outside the observed range (e.g., Treister et al. 2008; Polletta et al. 2008; DiPompeo et al. 2016b; Yan et al. 2019). We also considered the effect of allowing our simulated quasars to be obscured by the parsec-scale dusty torus and by its host galaxy's interstellar gas. This model is able to produce a population of quasars that have an obscured fraction that falls within the observed range, but the dark matter halo mass difference between the obscured and unobscured populations is too small compared to what is calculated from mid-IR clustering measurements.

Some evolutionary paradigms of obscuration have been able to broadly recover observed dark matter halo masses of mid-IR selected quasar populations (e.g. Di Matteo et al. 2005; Hopkins et al. 2008; DiPompeo et al. 2017b; Blecha et al. 2018). They assume co-evolution between the larger-scale galaxy properties and the small-scale environment of the AGN via various physical processes such as mergers or feedback. It is worth noting that even though evolutionary models have been able to reproduce dark matter halo mass measurements, they have also struggled to recover obscured fractions that fall within the range of observations (e.g., DiPompeo et al. 2017b). Here, we considered non-evolutionary physical models that describe how the properties of the galaxy or quasar could affect obscuring material on large and small scales. We implemented known empirical relationships between M_{halo}, galaxy mass, and SMBH mass, as well as relationships between a quasar's covering fraction and its λ_{Edd} and between its host galaxy's stellar mass and N_{H} (Moster et al. 2010; Häring & Rix 2004; Pannella et al. 2009; Tinker et al. 2010; Jones et al. 2016; Ricci et al. 2017; Buchner et al. 2017; Whitaker et al. 2017). We sought to determine if these relationships coupled with a luminosity threshold representative of the observational limitations of *WISE* could recover the host M_{halo} calculated via clustering measurements as well as an obscured fraction that fell within the range of observations. We found that these non-evolutionary approaches to modeling quasar evolution are not enough to be able to properly simulate observed populations of mid-IR selected quasars. We could not simultaneously recover mean M_{halo} for our obscured and unobscured quasars and an obscured fraction that falls within the range of observations. The dusty torus and galaxy-scale dust and gas both likely play a role in quasar obscuration, but evolutionary models that invoke processes for AGN triggering and feedback such as event-driven radiative blowout still need to be considered to be able to model populations of observed mid-IR selected quasars.

Chapter 3

The Space Density of Intermediate Redshift, Extremely Compact, Massive Starburst Galaxies

Kelly E. Whalen (Dartmouth College), Ryan C. Hickox (Dartmouth College), Alison L. Coil (University of California, San Diego), Aleksander M. Diamond-Stanic (Bates College), James E. Geach (University of Hertfordshire), John Moustakas (Siena College), David S. N. Rupke (Rhodes College), Gregory H. Rudnick (University of Kansas), Paul H. Sell (University of Florida), Christy A. Tremonti (University of Wisconsin-Madison, Madison), Julie D. Davis (University of Wisconsin-Madison, Madison), Serena Perrotta (Unievrsity of California, San Diego), Grayson C. Petter (Dartmouth College)

This work first appeared in The Astrophysical Journal 2022, volume 164, page 222.

3.1 Introduction

Galaxy formation models within a Λ-Cold Dark Matter (ΛCDM) framework that do not include feedback typically over-predict the present day baryon fraction as well as the number of number density of galaxies on the high and low mass ends of the local stellar mass function (SMF) (e.g., Croton 2006; Kereš et al. 2009; Moster et al. 2010; Moustakas et al. 2013). This implies that star formation over cosmic timescales is inefficient, which requires that galaxy formation models inject energy into cooling clouds of gas. This is typically done by invoking feedback from massive stars and active galactic nuclei (AGNs) to heat and eject gas, thus reducing star formation efficiency (e.g., Springel et al. 2005b; Di Matteo et al. 2005; Somerville & Davé 2015). Feedback as a driver of the cosmic star formation inefficiency is supported by evidence of large-scale gas outflows and/or relativistic jets in star forming and active galaxies (e.g. Veilleux et al. 2005; McNamara & Nulsen 2007; Fabian 2012; Somerville & Davé 2015).

In massive galaxies, feedback-driven outflows are often attributed to AGN activity since dark matter halo mass, galaxy stellar mass, bulge mass, and black hole mass all scale with one another (e.g., Ferrarese & Merritt 2000; Guo et al. 2010; Kormendy & Ho 2013). However, cosmological galaxy formation simulations show that the exclusion of stellar feedback in models leads to the formation of galaxies that are ~ 10 times more massive than observed at a given redshift, showing that stellar-driven feedback plays an integral role in regulating star formation in massive galaxies (e.g., Springel et al. 2005b; Hopkins et al. 2012). On small (giant molecular cloud) scales, feedback can slow the local star formation rate by decreasing the gas surface density in a region, but this alone is not sufficient to produce simulated galaxies whose masses match those observed. Large-scale galactic wind-driven outflows where $\dot{M}_{*,outflow} \sim$ SFR are necessary to be able to model galaxies with masses that are consistent with observations (e.g., Veilleux et al. 2005).

Constraining the importance of feedback-driven quenching is crucial to understanding how massive galaxies form, especially at high redshift. Massive, quiescent galaxies at $z > 1.5$ are typically more compact than their local counterparts by roughly a factor of 5 (e.g. Zirm et al. 2007; van Dokkum et al. 2008; van der Wel et al. 2014). The likely progenitors of these massive, compact quiescent galaxies are similarly compact star forming galaxies that were formed in gas-rich mergers of disk galaxies and were then rapidly quenched via some dissipative feedback (e.g., Barro et al. 2013; Stefanon et al. 2013; van Dokkum et al. 2015b). However, heavy dust obscuration coupled with high redshift makes constraining the role of AGN vs. stellar-driven feedback difficult with the typical UV signatures of outflows (e.g., van Dokkum et al. 2015b).

We have been studying a population of $z \sim 0.5$ massive, compact galaxies which show signs of recent, extreme bursts of star formation and gas depletion, similar to what we would expect as the progenitors to high-z massive, quiescent galaxies (Tremonti et al. 2007; Diamond-Stanic et al. 2012, 2021; Geach et al. 2013; Sell et al. 2014; Geach et al. 2014; Rupke et al. 2019; Petter et al. 2020). Our sample of galaxies consists of sources initially targeted as SDSS quasars, but subsequently classified as young post-starburst galaxies due to their blue stellar continua, weak nebular emission lines, and bright infrared photometry (Tremonti et al. 2007). Hubble Space Telescope (*HST*) imaging showed that these galaxies have extremely compact morphologies ($R_e \sim 100$ pc) with tidal features indicative of having recently undergone a major merger event (see Figure 4.1) (Diamond-Stanic et al. 2012; Sell et al. 2014). We also note that rings and diffraction spikes from the *HST* PSF are visible in the images of our sources, showing that their angular sizes are on the order of that of the PSF which further highlights their compactness (Sell et al. 2014; Diamond-Stanic et al. 2021; Davis et al. in prep). The sources in our sample can have SFR surface densities up to ~ 1000 M$_\odot$ yr^{-1}kpc^{-1} (Diamond-Stanic et al. 2012; Sell et al. 2014), and lie below the $0.5 < z < 1$ size-mass relations for star forming and quiescent galaxies (see Figure 3.2; Mowla et al. 2019; Diamond-Stanic et al. 2021). Spectroscopic observations show that these galaxies host outflows with velocities > 1000 km s^{-1} that can extend to tens of kpc (Tremonti et al. 2007; Rupke et al. 2019; Davis et al. in prep). There is also little evidence that these massive outflows are primarily driven by AGN activity based on X-ray, IR, radio, and spectral line diagnostics, meaning that extreme star formation can be responsible for gas depletion in these galaxies (Diamond-Stanic et al. 2012; Sell et al. 2014; Petter et al. 2020).

These galaxies are important because they allow us to directly observe the effects of extreme star formation on gas kinematics in starburst and post-merger galaxies. In merger-driven galaxy evolution scenarios, a major merger event can trigger a strong burst of obscured star formation. Dissipative feedback via AGN or starburst activity can then expel large amounts of gas and dust from the galaxy, allowing it to passively evolve into a gas-poor massive elliptical galaxy (e.g. Sanders et al. 1988; Lonsdale et al. 2006). The objects we are studying can possibly be representative of galaxies that are actively undergoing quenching, and might be an important phase for the building up of a massive, quiescent elliptical population. However, this is difficult to determine without knowing the space density of extreme compact starburst galaxies like the ones we have been studying. We are broadly defining our compact starbursts as massive, centrally concentrated galaxies that have recently experienced a burst of star formation. The space density of extreme massive, compact starbursts is strongly dependent on the timescales upon which starburst events can be observed using our selection criteria.

The aim of this paper is to estimate the average amount of time sources in a simulated galaxy population would be selected as extreme compact starburst galaxies under our selection criteria, in addition to their space density. We also place our galaxies into context with their high redshift compact star forming analogs, compact quiescent galaxies, post starburst galaxies, ultraluminous infrared galaxies (ULIRGs), the merger rate density, and massive, quiescent galaxies within the same redshift interval (e.g. Sanders et al. 1988; Lonsdale et al. 2006; Lotz et al. 2011; Barro et al. 2013; van der Wel et al. 2014; Wild et al. 2016).

The outline of the paper is as follows: in Section 3.2 we discuss the selection of the parent sample of galaxies. In Section 3.3 we discuss empirical model construction and constraining model free parameters via an MCMC routine. In Section 3.4 we discuss our implementation of the SDSS quasar selection function. In Section 3.5 we calculate the average observability timescale and space density for our population of compact starbursts. In Section 3.6 we place our galaxies into cosmological context with other phases of merger-driven galaxy evolution. We adopt a cosmology of $H_0 = 70.2$ kms^{-1}Mpc^{-1}, $\Omega_M = \Omega_{CDM} + \Omega_b = 0.229 + 0.046 = 0.275$, and $\Omega_\Lambda = 0.725$ (Komatsu et al. 2011)

3.2 The observed sample

The selection criteria used for our sample will be detailed in Tremonti et al. in prep, but we will give a brief summary in this section.

Our sample was originally selected with the objective to understand the role galaxy-scale winds play in star formation quenching for massive, intermediate redshift galaxies. The parent sample of galaxies we use in this work is drawn from the Eighth Data Release of SDSS (York et al. 2000; Aihara et al. 2011). We set out to select sources that were targeted as quasars (flagged either as QSO_HIZ, QSO_CAP, QSO_SKIRT, QSO_MAG_OUTLIER), since the SDSS QSO sample extends to fainter magnitudes than the main galaxy sample (Strauss et al. 2002). Selecting sources that have been targeted as quasars allows our sample to consist of objects that are massive and compact. The magnitude limits ensure that our sources are massive, highly star forming, and not strongly dust attenuated and the SDSS quasar selection algorithm requires that our sources are either unresolved or that they are resolved but satisfy more stringent color-magnitude cuts. This is described in more detail in Section 3.4.1.

We required that our sources were spectrally classified as galaxies with apparent $16 < i < 20$. We selected sources within $0.4 < z < 0.9$ to ensure that the MgII $\lambda\lambda 2796, 2804$ line would be shifted into the optical so we could use that as a probe of galactic winds. We also exclude sources that were classified as distant red galaxies (LEGACY_TARGET1 != DRG). Sources with redshift warnings and bad quality plates were also thrown away. This initial cut left us with a sample of 1198 galaxies.

We fit the SDSS spectra with a combination or simple stellar population models, similar to Tremonti et al. (2004), and a type I quasar template. From the spectral fitting, we calculated the fraction of light attributed to the quasar model (f_{qso}). We also measured nebular emission and stellar absorption line indices (following Kauffmann et al. 2003b) for the sources in our parent sample as well as the strength of the 4000 Å break (D$_n(4000)$) (Balogh et al. 1999). Our initial aim was target post starburst galaxies (PSBs) by selecting galaxies with evidence of having gone through a starburst event within the last 1 Gyr ((Hδ_A + H$\gamma_A)/2$ OR $D_n(4000) < 1.2$.), but with little ongoing star formation within the last 10 Myr ([OII] 3727 Å equivalent width (EW) > -20 Å). These cuts reduce our sample to 645 sources.

Lastly, our sample was limited to consisting of brighter galaxies with tighter cuts on [OII] EW and including a cut on the measured quasar fraction to further ensure that strong AGN were not included. The new cuts imposed were [OII] 3727 ÅEW > -15 Å, and $f_{qso} < 0.25$. We also require that apparent g and i magnitudes were brighter than $g < 20$ or $i < 19.1$. Although we select for weak nebular emission to eliminate starbursts, many of our sources were detected in *WISE* (Wright et al. 2010), and SED fitting through the mid-infrared shows they can have SFRs$= 20 - 500$ M$_\odot$ yr^{-1} (Diamond-Stanic et al. 2012; Perrotta et al. 2021; Davis et al. in prep). These cuts leave us with a sample of 121 galaxies. We take advantage of the *WISE* detections for our sources and make an IR color cut of $W1 - W2 < 0.8$ to further limit AGN contamination (Stern et al. 2012; Hickox et al. 2017). The *WISE* AGN cut leaves us with a population of 115 galaxies in what we are considering to be our parent sample. We include this selection criteria in our modeling of compact starburst galaxies to estimate the amount of time our galaxies would be targeted and selected by this set of criteria. A full list of targets is given in Table 3.1 along with their redshifts, stellar masses, and SDSS photometry.

In addition to the SDSS and *WISE* data for our parent sample, we also have high-S/N ($\sim 15-30$ per pixel) spectra from the Blue Channel Spectograph on the 6.5-m MMT (Angel et al. 1979), the Magellan Echellette (MagE; Marshall et al. 2008) spectrograph on the Magellan Clay telescope, and the Low Resolution Imaging Spectrometer (LRIS; Oke et al. 1995) on the Keck I telescope for 37 of the sources in our parent sample. These observations and their data reduction are detailed in Davis et al. (in prep), but broadly these observations were done using 1" slits resulting in spectra with resolution $R \sim 600-4100$. We refer to these 37 galaxies as the MgII sample.

3.3 Model construction

The aim of this work is to constrain the importance of massive, compact starburst events in galaxy quenching at $z \sim 0.5$ by estimating the space density of these objects. Here, we do this by constructing an empirical model based on the galaxies we have in our sample and then evolving a large simulated population of compact starbursts to estimate the timescales upon which they would be targeted by our selection criteria. This process can be broken down into two steps:

1. Construct a set of template distributions of stellar population parameters and SFHs by fitting SDSS $ugriz$ model mags and *W1, W2* photometry for the 115 galaxies in our sample with a Markov Chain Monte Carlo (MCMC; Metropolis et al. 1953; Foreman-Mackey et al. 2013) fitter.

2. Use the posterior distribution of SFH parameters from step 1 to predict luminous properties of a set of mock galaxies whose SFHs are consistent with our observed sample. The luminous properties are computed using the FLEXIBLE STELLAR POPULATION SYNTHESIS models (FSPS; Conroy et al. 2009).

Since our small sample of galaxies consists of sources that are unresolved in SDSS imaging, we have to make a number of assumptions about their underlying stellar populations. First, we assume that the light from our compact starburst galaxies can largely be broken down into two components: a young, simple stellar population (SSP) that formed in a single, nuclear burst, and an older component that has a star formation history representative of a massive, star forming galaxy at $z \sim 0.5$. We note that there is likely clumpy star formation occurring outside of the nuclear regions of our galaxies, but due to their extremely compact *HST* morphologies it is fair to assume that the contribution of these star forming regions to the total emitted light is minimal compared to the large nuclear burst. We also assume that our galaxies will only experience one burst of nuclear star formation and will then passively evolve. Although *HST* observations (Sell et al. 2014) showed that many of our sources have more than one core that could trigger a starburst event, we note that these sources are still unresolved in SDSS so the burst would not be localized to a particular core. This assumption is also consistent with the single burst of star formation triggered by a merger event seen in simulations (e.g. Springel et al. 2005a). Next, we naively assume that since the nuclear burst component dominates the spectral energy distribution (SED) of the total system, that the differences observed between the galaxies in our sample can solely be attributed to differences in the properties of the nuclear starburst. This assumption is consistent with the galaxies in the MgII sample having very blue spectra and young ages as derived from spectral modeling (e.g., Davis et al. in prep).

These assumptions allow us to construct a model that utilizes FSPS to simulate the stellar populations for the nuclear starburst component as well as the older, non-burst underlying stellar population. In our modeling framework, we introduce four free parameters that are fit via an MCMC routine for each of the galaxies in our sample: the age of the burst (t_{age}), the fraction of total galaxy stellar mass formed in the nuclear burst (f_{burst}), the optical depth for the dust around young stars formed in the nuclear burst ($\tau_{dust,1}$), and the total stellar mass of the system (M_*). We separately calculate the $ugriz$, *W1*, *W2*, [OII] (3727 Å) fluxes for the nuclear burst and non-burst components and their f_{burst} weighted sum to determine the SED and [OII] EW for the total simulated galaxy.

In this section, we describe the assumptions made in the FSPS modeling of both the extended non-burst and nuclear starburst components as well as the MCMC fitting we use to constrain values for the free parameters in our model.

For both, the non-burst and nuclear burst components, we make the following assumptions. We assume a Chabrier (2003) initial mass function (IMF_TYPE = 1) and $\log Z/Z_{\odot} = -0.3$ metallicity (LOGZSOL = -0.3) using the $M_* - Z$ relation presented in Gillman et al. (2021) calibrated for solar $12 + \log(\mathrm{O/H}) = 8.66$ and $Z_{\odot} = 0.0121$. We set ADD_NEB_EMISSION = TRUE to allow for nebular emission from CLOUDY models (Byler et al. 2017). We assume Charlot & Fall (2000) extinction (DUST_TYPE = 0) with DUST_TESC = 7 ($\log(t_{age}/\mathrm{yr})$) (e.g Blitz & Shu 1980; Charlot & Fall 2000; Conroy et al. 2009), where DUST_TESC is the age in Charlot & Fall (2000) extinction model at which stars are attenuated by $\tau_{dust,1}$ and $\tau_{dust,2}$. We also set AGB_DUST = TRUE since IR SEDs of star forming galaxies are poorly fit without incorporating dust shells around AGB stars (Villaume et al. 2015).

3.3.1 Modeling the extended, non-burst component

The photometric and morphological properties of the extended stellar population are most important in the later stages of the compact starburst's evolution since the contribution of the nuclear burst wanes over time. Here, we describe the assumptions we make in the FSPS modeling of the extended, non-burst component. We initialize FSPS such that TAGE is the

Hubble time (in Gyr) at the redshift of a given galaxy, DUST1 = 1, and DUST2 = 0.5. We chose these dust optical depths to ensure that the ug photometry for the modeled extended stellar component would be fainter than that of the reddest observed sources in our sample, while being consistent with the recommended values given in Charlot & Fall (2000). We explored the effects of changing TAGE and the dust parameters for the extended components in the galaxies shown in Figure 4.1 to ensure that our modeling is largely robust to extended component assumptions and found that the results of our MCMC fitting do not change with changing non-burst initial conditions.

A crucial piece to modeling the stellar population of the extended, non-burst component is assuming a particular star formation history (SFH). *HST* images show hints of a smooth, extended underlying stellar population (Diamond-Stanic et al. 2021). The presence of tidal features in our *HST* observations suggests that the galaxies in our sample have recently undergone merger events, and their high star formation surface densities indicate that that these mergers were likely gas rich (e.g., Diamond-Stanic et al. 2012; Sell et al. 2014). Based on this, we assume that the extended, non-burst stellar populations have a star formation history typical of actively star forming disk galaxies.

However, the SFHs of star forming disk galaxies are uncertain. There are many possible SFHs that would be able to build up the tightly-correlated star formation main sequence at late cosmic times (e.g. Oemler et al. 2017). For simplicity, since young stars dominate the light output from a stellar population we approximate the SFH as being flat over cosmic time to ensure that the progenitor galaxies in the system were experiencing some degree of star formation prior to merging. We do this by setting the FSPS SFH parameter as a delayed-burst SFH (sfh = 4 in FSPS) but with the constant star formation fraction set to 1.

We also note that we explored other SFHs that peaked at earlier cosmic times, such as the dark matter halo mass dependent models constructed in Behroozi et al. (2019), but our MCMC chains for these models were not able to reach convergence. The inability for our chains to converge is consistent with the fact that we do not believe that Behroozi et al. (2019)-like SFHs would be physically representative of galaxies like those in our sample. For massive ($M_* \sim 10^{11}$ M$_\odot$) galaxies like the ones in our sample, this would suggest that our sources would have peaked in star formation at $z \sim 2$ and then passively evolved until $z \sim 0.5$. This would imply that the progenitors of our compact starbursts would be almost entirely be quiescent, which is unlikely do to their high gas fractions. Therefore, we do not include models like this in our analysis.

3.3.2 Modeling the nuclear burst

Recent observational evidence has shown that intermediate redshift, extreme compact starburst galaxies are likely to exhibit flat age gradients, meaning that their optical light is dominated by star formation that began and ended in one uniform event (e.g., Setton et al. 2020). Since we expect all of the stars formed in the nuclear burst to have formed at approximately the same time, we model the starburst as a simple stellar population (SSP) in FSPS (sfh = 0). This choice is consistent with very short burst durations we derive from non-parametric SFH modeling of a subset of our sample with high S/N spectra (Geach et al. 2018; Tremonti et al. in prep; Davis et al. in prep). This work (detailed in Davis et al. (in prep)) is done by fitting the rest frame UV-mid IR broadband photometry and high-resolution spectra simultaneously using Prospector (Leja et al. 2019; Johnson et al. 2021). We also assume that the dust in the vicinity of the nuclear starburst extincts some of the light from the newly formed stars. We leave the age of the central burst ($\log t_{age}$) and the optical depth (τ_{burst}) as free parameters that will later be constrained with MCMC fits to the photometric data of the sources in our observed sample. We set DUST2 = $\tau_{burst}/2$ (e.g., Wild et al. 2011). We similarly calculate SDSS $ugriz$ and *WISE* W1 & W2 magnitudes for the nuclear bursts as we did for the extended, non-burst stellar population.

3.3.3 Calculating PSF magnitudes

Once we have the model photometry for the extended, non-burst stellar populations and their nuclear bursts, we can combine them to get the photometry for the entire system. We start by converting the modeled apparent AB magnitudes for the extended, non-burst stellar population and the burst component to flux densities. The output magnitudes of FSPS are normalized to 1 $M_\odot$ at every epoch, so we calculate the fluxes for our galaxies and nuclei by multiplying their 1 $M_\odot$ flux densities by their respective masses. We define the mass of the nuclear burst as $M_{nuc} = f_{burst} \times M_*$ and $M_{host} = (1 - f_{burst}) \times M_*$. We also leave f_{burst} and M_* as free parameters in our MCMC fitting in addition to τ_{dust} and $\log t_{age}$ as described earlier.

For sources observed in SDSS, the QSO targeting pipeline takes a source's $ugriz$ PSF magnitudes as input rather than its de Vaucouleurs or exponential disk model magnitudes (Richards et al. 2002). The output magnitudes from FSPS are representative of model magnitudes, so we must first convert these to PSF magnitudes before we run the SDSS QSO targeting algorithm on our modeled sample. We do this by first assigning surface brightness profiles to both components of the galaxy. For the extended, non-burst component, we assume a $n = 1$ Sérsic profile where the effective radius (R_{eff}) is taken from the redshift-dependent star forming galaxy size-mass relation presented in Mowla et al. (2019). Due to the nuclear starburst's compact nature, we assume a $n = 4$ Sérsic profile where R_{eff} is ~ 300 pc, as motivated by observations (e.g., Geach et al. 2013; Sell et al. 2014). Diamond-Stanic et al. (2021) showed that $R_{eff} < 1$ kpc for the *HST*-observed galaxies. We do not vary R_{eff} for the nuclear components for our modeled galaxies since ~ 100 pc scale starbursts would always be unresolved in SDSS and are effectively observed as point sources.

We convert R_{eff} for each component from kpc to arcsec using their cosmological angular size distances and normalize the surface brightness profiles ($I(r)$) for each component such that

$$2\pi \int_0^\infty I_{comp}(r) r dr = f_{\nu,comp}.$$

We then convolve these component surface brightness profiles with the SDSS PSF in each photometric band. The full width half maxes (FWHMs) for the $ugriz$ bands are 1.53, 1.44, 1.32, 1.26, 1.29 arcsec, respectively. The convolved burst and disk components are then added together to create a modeled total galaxy surface brightness profile. We then fit this profile with a 2D-Gaussian model of the SDSS PSF and integrate the Gaussian model fit to obtain PSF fluxes in each respective band. The PSF fluxes are then converted to apparent AB magnitudes so they could later (§4.1) be passed through the SDSS QSO selection pipeline.

3.3.4 Constraining model free parameters with MCMC

We have constructed a 4-parameter model for the photometry and [OII] (3727 Å) EW of intermediate-z compact starbursts by utilizing FSPS. FSPS directly outputs model mags and spectra of stellar populations. We calculate [OII] (3727 Å) EW from the FSPS output spectrum using SPECUTILS (Earl et al. 2022). As stated above, our compact starburst model is the sum of separately modeling the host galaxy and nuclear burst contributions to the overall photometric and spectral properties. In this model, we leave the age of the nuclear starburst (log t_{age}/Myr), the burst fraction (f_{burst}), optical depth of dust extincting young stellar light (τ_{dust}), and the galaxy stellar mass (log $M_*/M_\odot$) as free parameters. Here we detail how we constrain possible parameter values using MCMC fitting to the $ugriz$ and W1/W2 photometry for our observed galaxies.

3.3.4.1 Parameter fitting

As discussed in Section 3.2, our collaboration has been studying a sample of 115 intermediate-z compact starburst galaxies. Archival SDSS $ugriz$ and *WISE* W1 and W2 photometry are available for the full parent sample. For each of these, we constrain the

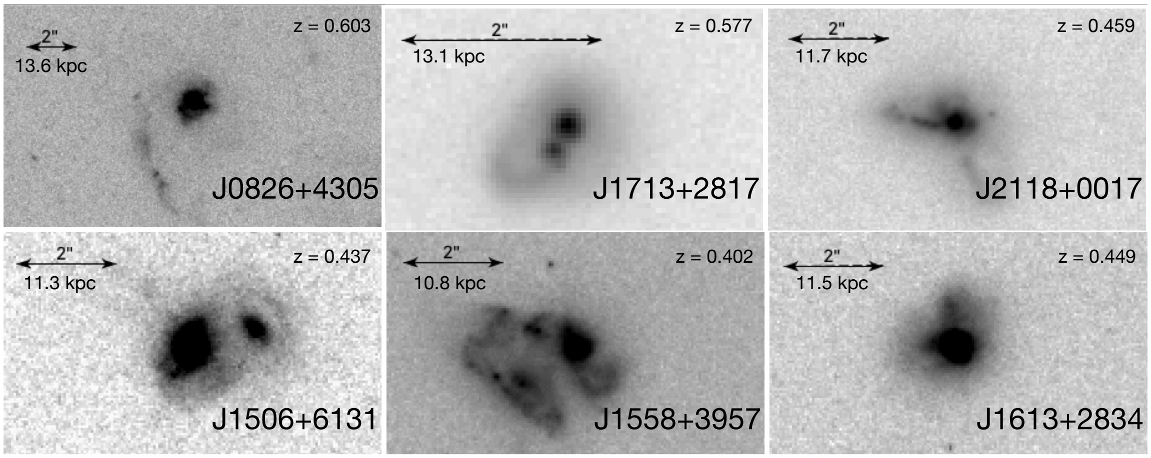

Figure 3.1 *HST* WFC3 cutouts of 6 representative galaxies in our sample that overlap with those presented in Sell et al. (2014). We note that we omit J0944+0930 and J1104+5946 from Sell et al. (2014) as they do not satisfy all of our selection criteria. All of these galaxies show clear signs of tidal disruptions, consistent with their extreme nuclear starbursts being triggered by major merger events.

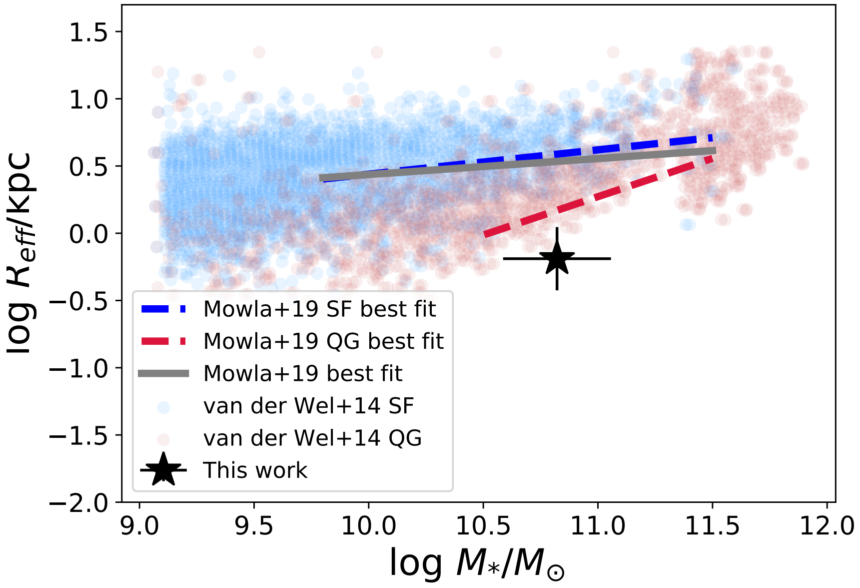

Figure 3.2 Location of our galaxies (black star) within the $0.5 < z < 1$ size-mass plane as presented in Mowla et al. (2019). Blue and red points are van der Wel et al. (2014) star forming and quiescent galaxies, respectively. The red, blue, and grey lines are the best fit size-mass relations for the quiescent, star forming, and total CANDELS/3DHST galaxies in Mowla et al. (2019). Our data point represents the average R_{eff} and M_* for a subset of the MgII galaxies presented in Davis et al. (in prep). Our sources are significanly more compact than other galaxies at similar z and M_*.

probability densities for $\log\ t_{age}$, f_{burst}, τ_{dust}, and $\log M_*$ using the ensemble adaptation of the Metropolis-Hastings MCMC algorithm from the package, EMCEE (Metropolis et al. 1953; Foreman-Mackey et al. 2013). Each step of our MCMC calculates the model SDSS $ugriz$, *WISE* W1, and W2 photometry, and compares them to those for each observed galaxy. For each galaxy, we run the MCMC such that the autocorrelation time for each walker is ~ 50 times less than the run time. For most of our galaxies this is $\sim 60,000$ steps. We use the EMCEE ensemble stretch move with scale parameter $a = 2$. We randomly initialize each walker in the intervals

$$0.5 < \log\ t_{age}/\text{Myr} < 2$$

$$0.05 < f_{burst} < 0.4$$

$$0.3 < \tau_{dust} < 1$$

$$10 < \log M_*/M_\odot < 11$$

and allow them to explore the parameter space

$$0.5 < \log\ t_{age}/\text{Myr} < 3$$

$$0.05 < f_{burst} < 0.65$$

$$0 < \tau_{dust} < 5$$

$$10 < \log M_*/M_\odot < 12$$

such that it finds the parameter values that are most likely to minimize the difference between the model and observed photometry.

For each galaxy in our sample, we output the mean parameter values and their covariance from MCMC-calculated posterior distributions. We use these mean values and their covari-

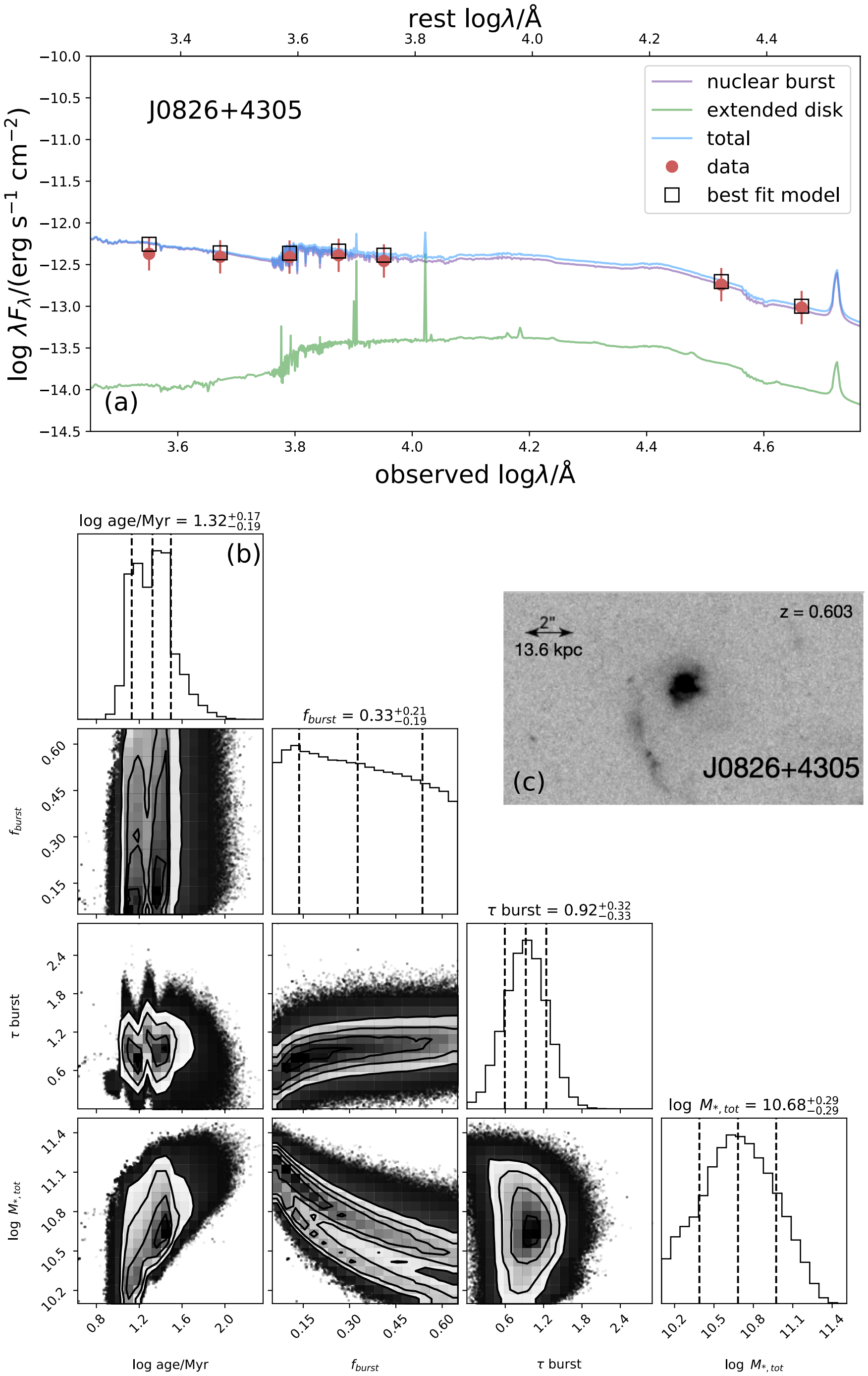

Figure 3.3 *Panel (a)*: Best fit SED for galaxy J0826+4305. The red points and error bars are the observed photometry and ± 0.25 magnitude uncertainty region, respectively. The open black squares are the modeled photometry. The blue, violet, and green curves are the modeled SED for the total galaxy system, nuclear burst, and host galaxy, respectively. *Panel (b)*: Triangle plot of parameter posterior distributions for galaxy J0826+4305. We calculate the mean and covariances of these posterior distributions to model them as 4D-Gaussian distributions. We then randomly draw sets of parameter values from the Gaussian-modeled posterior to construct a mock population of compact starbursts. *Panel (c)*: Galaxy cutout as seen in Figure 4.1.

ances to model these posteriors as 4-dimensional Gaussian distributions whose means and standard deviations are identical that of the MCMC output. We do this to reduce noise later in our analysis since we use these distributions to randomly draw sets of parameter values to model mock galaxies based on the ones in our observed sample. The best fit SED and parameter probability distributions for a constantly star forming host based on the galaxy J0826+4305 can be seen in panels (a) and (b) Figure 3.3, respectively.We also include these for J1713+2817, J2118+0017, J1506+6131, J1558+3957, and J1613+2834 in Figures 3.9, 3.10, 3.11, 3.12, and 3.13, respectively. For consistency with other studies of our objects, we note general agreement between our best fit stellar masses and those presented in Sell et al. (2014) for the galaxies that were included in both of our samples. This is shown in Table 3.2.

For each of the 115 galaxies in our sample we randomly draw $\log\ t_{age}$, f_{burst}, τ_{dust}, and $\log M_*$ values from their respective Gaussian-modeled posterior distributions taking into account the covariances between each of the parameters, to model a population of galaxies with properties similar to the observed source. We can then evolve these modeled galaxies to estimate a distribution of selectable lifetimes for each of the galaxies in our sample.

3.4 Modeling the targeting algorithm & selection function

The ultimate goal for our model is to be able to estimate the space density of $z \sim 0.5$, massive, compact starburst galaxies. To do this, we need to understand the timescales upon which these galaxies would be selected under a set of targeting criteria. Here, we detail how we model the various components of the selection function we use to identify sources in our sample.

3.4.1 The SDSS QSO targeting algorithm

All of the sources in our observed sample were initially targeted for SDSS spectroscopy as QSOs based their bright magnitudes and blue colors. In order to ensure that our modeled galaxies would satisfy these criteria, we need to incorporate this selection into our modeled targeting function.

The SDSS QSO targeting algorithm identifies sources based on their location in three-dimensional color space. This is the $(u-g)$-$(g-r)$-$(r-i)$ $(ugri)$ color cube for $z < 3$ sources and $(g-r)$-$(r-i)$-$(i-z)$ $(griz)$ cube for galaxies at higher redshifts. The QSO catalog constructed from SDSS DR8 sources was selected using the Richards et al. (2002) targeting algorithm [1]. The SDSS quasar selection function aims to identify sources that lie far from the region of color space where stars are most likely to be found as well as for sources to satisfy general color/magnitude cuts. All magnitudes referenced in the targeting algorithm are PSF magnitudes. Since we are working with modeled data that is free from observational uncertainty, we do not include the steps in the algorithm that flag sources for having data with fatal errors.

Since quasars and local stars both exhibit bright apparent magnitudes and are unresolved point sources, the algorithm needs to be able to differentiate between them in color-color-color space. The algorithm makes use of the method described in Newberg & Yanny (1997) that defines a "stellar locus" in color-color-color space where stars are most likely to exist. The stellar locus is constructed by analyzing the distribution of SDSS identified stars in color space. To maintain generality, we will refer to the main coordinate system describing the color-color-color cube as $\langle \hat{x}, \hat{y}, \hat{z} \rangle$, where $\hat{x}$ is in the direction of the bluest color axis and $\hat{z}$ in the direction of the reddest. The locus construction algorithm begins by setting the endpoints of the stellar distribution in color space and then iteratively calculating midpoints. This process allows a local coordinate system $(\langle \hat{i}_i, \hat{j}_i, \hat{k}_i \rangle)$ to be defined at each locus point.

---

[1] Python adaptation of Richards et al. (2002) QSO selection algorithm can be found at www.github.com/ke27whal/sdss_qso_selection.

At each locus point (p_i), $\hat{k}_i$ is defined as a unit vector in the direction $\overrightarrow{p_{i+2} - p_i}$. As detailed in Newberg & Yanny (1997), unit vectors $\hat{i}_i$, $\hat{j}_i$, and $\hat{k}_i$ are given as

$$\hat{k}_i \equiv k_x \hat{x} + k_y \hat{y} + k_z \hat{z},$$

$$\hat{j}_i \equiv (\hat{k}_i \times \hat{z})/|\hat{k}_i \times \hat{z}| = (k_y \hat{x} - k_x \hat{y})/\sqrt{k_x^2 + k_y^2},$$

$$\hat{i}_i \equiv \hat{j}_i \times \hat{k}_i = [-k_x k_z \hat{x} - k_y k_z \hat{y} + (k_x^2 + k_y^2)\hat{z}]/\sqrt{k_x^2 + k_y^2}.$$

The cross section of the stellar locus is measured by fitting an ellipse perpendicular to $\hat{k}_i$ at each point. The semi-major and semi-minor axes of the ellipses are in the direction of unit vectors $\hat{l}_i$ and $\hat{m}_i$, respectively, and are defined as

$$\hat{l}_i \equiv \hat{i}_i \cos\theta_i + \hat{j}_i \sin\theta_i,$$

$$\hat{m}_i \equiv -\hat{i}_i \sin\theta_i + \hat{j}_i \cos\theta_i$$

where θ_i is the angle between the major axis of the ellipse and unit vector $\hat{i}$. We adopted the locus point positions, θ_i, $\hat{k}_i$, $|\vec{l}_i|$, and $|\vec{m}_i|$ values from Richards et al. (2002), and proceeded to construct right cylinders that define the 4σ stellar locus probability region in color-color-color space. We also incorporate the mid-z inclusion region as the white dwarf/A star exclusion regions detailed in Richards et al. (2002).

Sources targeted as quasars must also satisfy color and magnitude cuts in addition to not belonging to the stellar locus. For low-z sources in the $ugri$ color cube, all objects must have apparent i-band magnitude $15 < i < 19.1$ (Richards et al. 2002). Both extended and point source objects are allowed to be selected as quasars, but they need to satisfy different sets of criteria. Point source objects only need to fulfill the magnitude and stellar locus cuts to be targeted. Extended sources are kept if they are likely to contain an active nucleus. This is most likely when $(u - g) < 0.9$, as redder AGN would be at high-z and would not be extended (Richards et al. 2002; Adelman-McCarthy et al. 2006). This $(u - g)$ cut does not remove blue, extended star forming galaxies, so a second cut of $l_i > 0$ and $m_i > 0$ is applied where l_i and m_i are positions within the $\langle \hat{k}, \hat{l}, \hat{m} \rangle$ coordinate space defined earlier. In the high-z $griz$ color cube, all outliers from the stellar locus with $15 < i < 20.4$ are targeted as quasars. However, to avoid contamination from low-z quasars, sources are removed from the high-z sample when all of the following criteria are met;

$$(g - r) < 1.0,$$

$$(u - g) \geq 0.8,$$

$$i \geq 19.1 \ \text{ OR } \ (u - g) < 2.5.$$

We allow the sources in our sample to be targeted as either low-z or high-z quasars since our observed sample contains a mixture of both target types.

3.4.2 Spectroscopic/photometric selection

In addition to being blue, unresolved sources, the galaxies in our sample also exhibit weak nebular emission characteristic of post starburst galaxies. As mentioned earlier, we implement an emission line equivalent width (EW) cut on [OII] (3727 Å) such that [OII] EW> -15 Å, consistent with that used for our parent sample (Sell et al. 2014; Davis et al. in prep; Tremonti et al. in prep). We also model the $g < 20$ flux limit and $W1 - W2 < 0.8$ *WISE* color cut that we impose on our sample.

3.5 Estimating the space density

In this section, we discuss the various parameters that contribute to the calculated compact starburst space density (n_{CS}) as well as the possible sources of uncertainty. We estimate the space density in the redshift range $0.4 < z < 0.9$ as

$$n_{CS} \sim \frac{N_{targeted}}{f_{complete}} \cdot \frac{t_{cosmic}}{V_{0.4<z<0.9}} \cdot \frac{A_{sky}}{A_{SDSS}} \cdot \left\langle \frac{1}{t_{obs}} \right\rangle . \tag{3.1}$$

Here, $N_{targeted}$ is defined as the number of galaxies in our observed sample of massive, compact starburst galaxies, $f_{complete}$ is the completeness of the SDSS QSO catalog ($f_{complete} \sim 0.9$; Vanden Berk et al. 2005), $V_{0.4<z<0.9}$ is the volume in Mpc^{-3} contained within the redshift range $0.4 < z < 0.9$, A_{SDSS}/A_{sky} is the fractional area of the SDSS footprint relative to the area of the entire sky, t_{cosmic} is the amount of cosmic time in Myr contained in the redshift range $0.4 < z < 0.9$, and $\langle 1/t_{obs} \rangle$ is the average of the inverse selectability timescale in Myr. The only model-dependent factor in this calculation is the amount of time our sources would be selected under a particular set of targeting criteria, so we will spend the first part of this section focusing on calculating this value.

It is also worth highlighting that the timescale we are calculating for our sources is the amount of time these objects would be targeted under our set of selection criteria. This is a separate quantity from the amount of physical time galaxies might be undergoing an extremely compact starburst phase. The physical timescale is also dependent on how we define these sources. A unifying feature of the observed sources in our sample is that they are late-stage major mergers that host extremely young stellar populations. It is possible that some of them have quenched/are very recent PSBs and that others are still forming stars. Broadly, we define our sources as galaxies that have recently experienced an extreme nuclear burst of star formation. Calculating the physical timescale for these sources would require much more detailed modeling which is beyond the scope of this work. Our goal here is to estimate the space density of objects that would be targeted by our selection criteria at some point in their evolution.

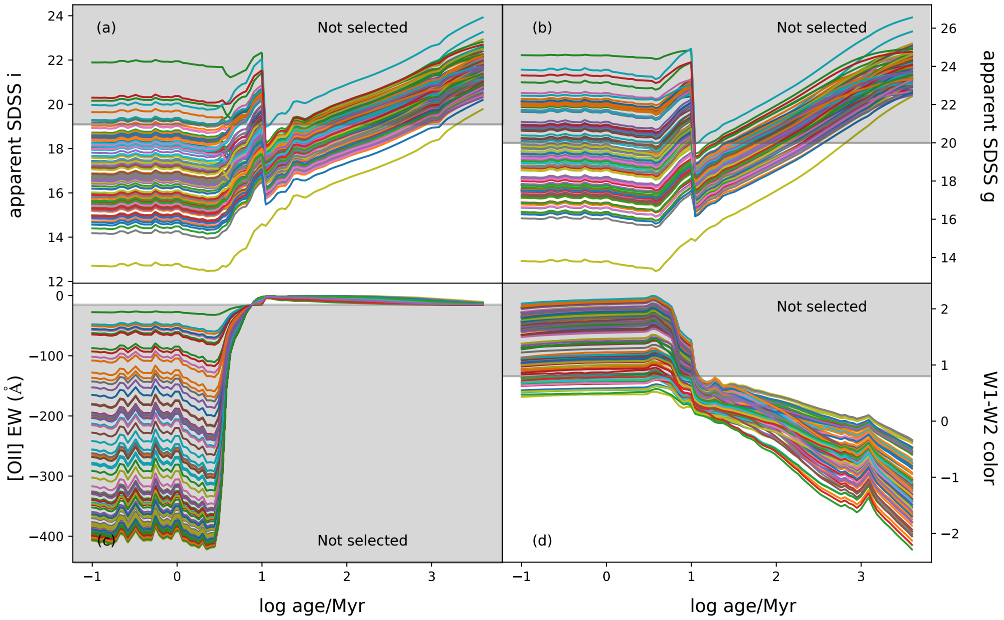

Figure 3.4 Shown here are the modeled evolutionary tracks of the apparent i-band and g-band *SDSS* magnitudes (*panels (a) & (b)*), [OII] equivalent width (*panel (c)*), and *WISE* $W1-W2$ color (*panel (d)*) for a sub-sample of modeled galaxies. The x-axis is age relative to the burst peak. The grey-shaded rectangles represent the regions of parameter space that would not be selected by the criteria placed on that given parameter. This is a schematic representation— the full details of our source selection can be found in Section 3.2.

3.5.1 Calculating observed lifetimes

For each of the 115 galaxies in our sample, we used SDSS $ugriz$ model mags and *WISE* W1/W2 measured photometry to construct SEDs which were then fit by our MCMC routine to obtain the posterior distributions for $\log t_{age}$/Myr, f_{burst}, τ_{dust}, and $\log\ M_{*,tot}/M_{\odot}$. These posterior distributions were then modeled as 4-dimensional Gaussian distributions and we output their covariance matrices. For each of the 115 observed galaxies in our sample, we draw 200 sets of parameters from the respective posterior distributions while taking into account covariances between parameters. This gives us 115×200 mock galaxies which we then evolve. We evolve our modeled galaxies within the time interval $-1 < \log\ t_{age}/\mathrm{Myr} < 2.5$ in 1000 uniformly spaced steps. We calculate [OII] EWs from the output FSPS spectrum using SPECUTILS (Earl et al. 2022), as well as the photometry at each step to determine if the sources would be targeted by our selection criteria at each time step. This allows us to construct selected lifetime distributions for each of the 115 observed galaxies in our sample. The evolutionary tracks for a subset of randomly selected galaxies' i and g-band magnitudes, [OII] EWs, and $W1 - W2$ colors, as well as the selection limits on each respective parameter can be seen in Figure 3.4. We note that Figure 3.4 does not include the SDSS QSO targeting selection since that is a much more complicated set of criteria and would be impossible to visually display. However, we do apply it in our target selection.

In the following section, we detail how we determine the space density of our sources by randomly sampling with replacement the selected lifetime distribution calculated by evolving mock galaxies. In short, we bootstrap by generating 100,000 randomly sampled (with replacement) populations of 115 mock galaxies. For each iteration, we randomly draw an array of 115 indices which correlates to the various observed galaxies in our sample. We use the randomly drawn indices to pull selected lifetimes from the corresponding selected lifetime distributions. We then average these lifetimes to determine a selectability timescale

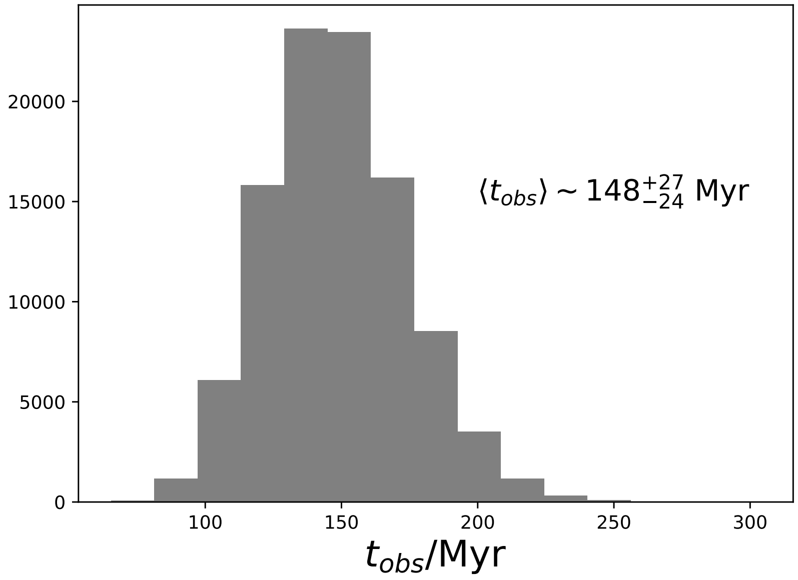

Figure 3.5 Distribution of average selected lifetimes from the mock sample. We find that extreme nuclear starbursts like the ones observed in our galaxies would be selected for $\sim 148^{+27}_{-24}$ Myr, consistent with the burst ages calculated in Davis et al. (in prep).

for that given mock population of galaxies. The average selected lifetime distribution for the 100,000 samples of 115 mock galaxies is shown in Figure 3.5. We find that on average, compact starburst galaxies like the ones we observe would be selected under our set of targeting criteria for 148^{+27}_{-24} Myr. This timescale is broadly consistent with the average post-starburst peak age of 70 ± 106 Myr calculated in Davis et al. (in prep).

In our modeling, we find that our mock galaxies would be targeted soon after the nuclear burst occurs, meaning that we can directly compare our selectability timescale and the post-starburst peak SF ages in Davis et al. (in prep). The light-weighted stellar ages of the MgII sample ranging from $\sim$ 13-300 Myr) galaxies are consistent with the calculated selectability timescale in this work. This is a good consistency check to ensure that our modeling shows that galaxies in our observed sample would be selectable at their best-fit stellar ages.

We next use the selectability timescales of our modeled compact starburst galaxies to estimate their space density.

3.5.2 Calculating space density

As stated above, we estimate the space density in the redshift range $0.4 < z < 0.9$ (Equation 3.1) by randomly sampling from our selected lifetime distributions. To ensure that we sample a sufficiently large population of mock galaxies, we iterate this part of the calculation 100,000 times.

For each of the 100,000 iterations, we randomly sample with replacement 115 galaxies from our mock sample. For each of the galaxies in that sample, we randomly draw a $\log t_{obs}/\mathrm{Myr}$ value from the observable lifetime distribution that corresponds to that particular galaxy. In each iteration, we use these $\log t_{obs}/\mathrm{Myr}$ values to compute,

$$\left\langle \frac{1}{t_{obs}} \right\rangle = \frac{1}{N_{sim}} \sum_{i}^{N_{sim}} \left(\frac{1}{t_{obs,i}} \right), \tag{3.2}$$

where $N_{sim} = 115$. We then use this to calculate the space density for the random population generated each iteration using the expression above. The resulting space density distribution (calculated using Equation 3.1) can be seen in Figure 3.6. We estimate the space density of these massive, compact starbursts to be $(1.1^{+0.5}_{-0.3}) \times 10^{-6}$ Mpc^{-3} in the redshift range $0.4 < z < 0.9$.

3.6 Cosmological context

One of the most interesting questions surrounding our sample of galaxies is whether or not this type of compact starburst phase is characteristic in the evolution of many, if not most, massive galaxies. A widely supported view of galaxy formation and evolution is that mergers are responsible for building up increasingly massive galaxies and for triggering

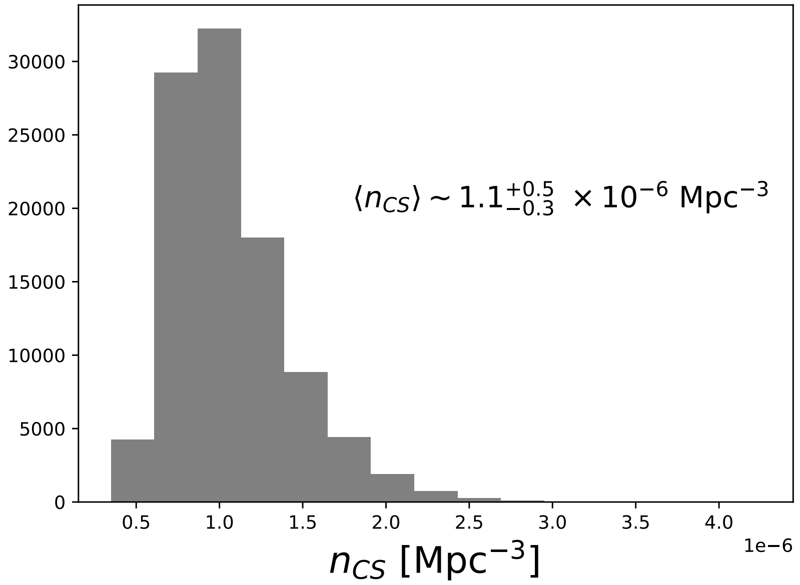

Figure 3.6 Space density distribution calculated from our mock population of galaxies. We estimate that the space density for our population of $0.4 < z < 0.9$ compact starburst galaxies is $(1.1^{+0.5}_{-0.3}) \times 10^{-6}$ Mpc^{-3}.

starbursts and AGN activity (e.g., Toomre 1977; Sanders et al. 1988; Kauffmann et al. 1993; Mihos & Hernquist 1996; Hopkins et al. 2006, 2008; Lotz et al. 2011; Somerville & Davé 2015). Sanders et al. (1988) presented a basic framework in which the collision of two gas-rich disk galaxies would funnel gas towards the center of the system via tidal streams or shocks, thus creating a dusty, gas-rich environment to foster rapid star formation (e.g. Lonsdale et al. 2006). This dusty starburst stage would be selected as a ULIRG. As gas is fueling rapid star formation, it is continuously being funneled into the nucleus and also being accreted onto the black hole, thus also triggering AGN activity (e.g. Hopkins et al. 2006, 2008). Within this framework, gas from the galaxy can be expelled by a blowout phase driven by violent, dissipative feedback.

The galaxies in our observed sample have many features that could tie them into this evolutionary framework. We know that the galaxies for which we have *HST* observations have disturbed morphological features such as tidal tails or two nuclei, which is indicative

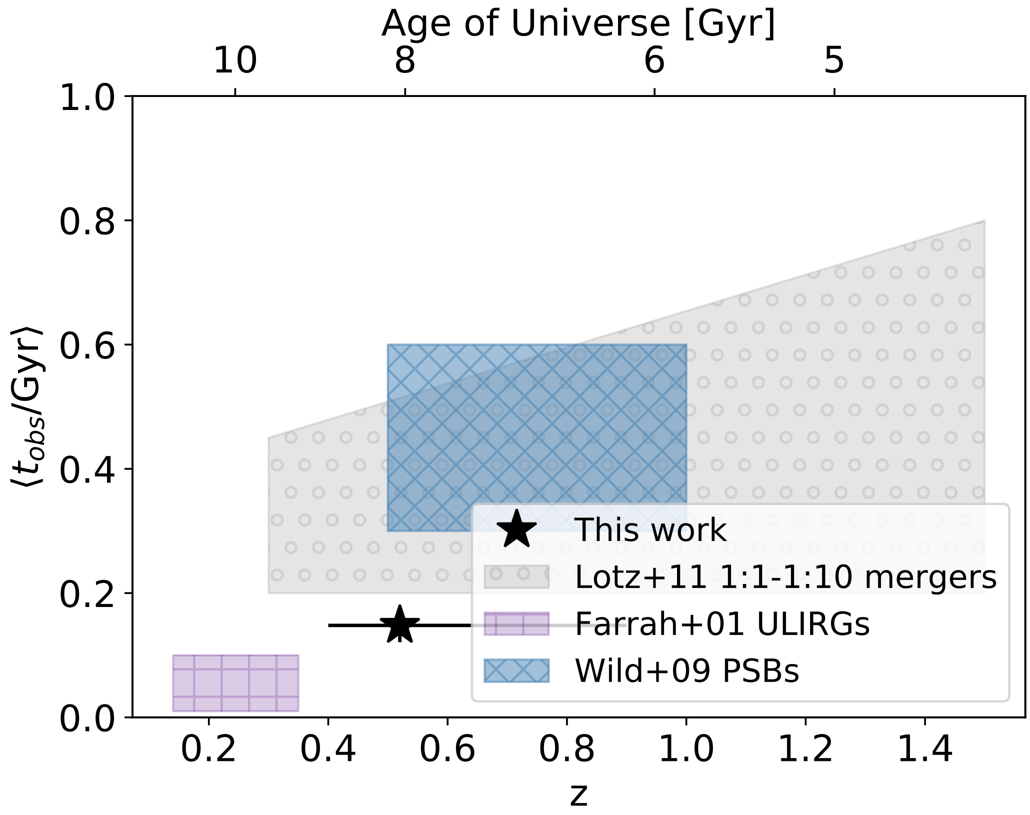

Figure 3.7 Comparison of the average timescales (in Gyr) upon which various phases of massive galaxy evolution would be observable. The black star represents the average selectability timescale for the modeled compact starburst galaxies in our sample, and its error bar along the redshift axis represents the size of the redshift range of our sources and the error bar along the t_{obs} axis is the statistical uncertainty calculated via bootstrapping as described in Section 3.5.2 The grey, purple, and blue shaded regions represent the range of observable timescales for galaxy mergers (Lotz et al. 2011), ULIRGs (Farrah et al. 2003), and post starburst galaxies (PSBs; Wild et al. 2016), respectively. We note that the timescales presented for galaxy mergers and PSBs correspond to the amount of time a source would be targeted under a set of selection criteria (similar to the value calculated for our sources), while the timescale for ULIRGs reflects the amount of physical time a source would experience star formation characteristic of the ULIRG phase. We elaborate on how we obtain the timescale estimates for the shaded regions in the text. It is clear that compact starburst galaxies like the ones in our sample occur on relatively short lived timescales that are comparable to that of ULIRG star formation.

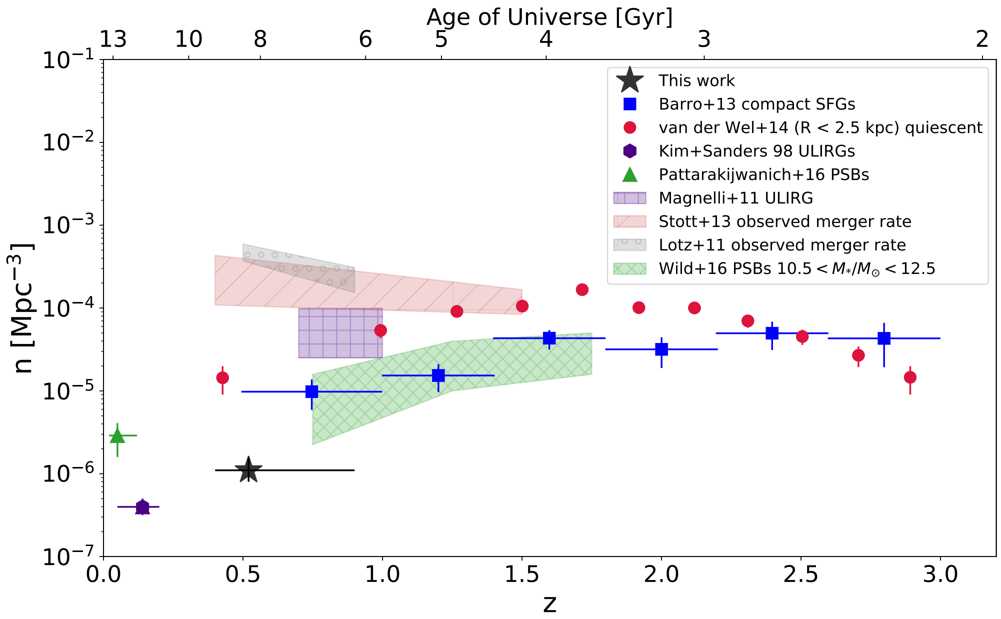

Figure 3.8 Comparison of the space densities of various phases of massive galaxy evolution. The black star represents the modeled space density for compact starburst galaxies like those in our observed sample. Its error bar along the redshift axis represents the size of the redshift range of our sources and the error bar along the space-density axis is the statistical uncertainty calculated via bootstrapping as described in Section 3.5.2. We note that there are additional systematic errors, including uncertainty with model assumptions, which make this statistical error a lower limit. The blue squares represent the space density evolution of massive, compact star forming galaxies from the CANDELS survey (Barro et al. 2013), the red points represent massive ($\log M_*/M_\odot \sim 11$), compact quiescent galaxies (van der Wel et al. 2014), the green triangle represents low-z PSBs (Pattarakijwanich et al. 2016), and the purple hexagon represents low-z ULIRGs (Kim & Sanders 1998). The grey, red, purple, and green shaded regions depict the Lotz et al. (2011) observed merger rate density, the Stott et al. (2013) observed merger rate density (calculated using merger observability timescales), ULIRG space density (Magnelli et al. 2011), and intermediate-z PSB space density (Wild et al. 2016) ranges, respectively. The Barro et al. (2013) points, Lotz et al. (2011) region, and Stott et al. (2013) region have been adjusted to account that our sources have masses $\log M_*/M_\odot > 10.5$, while most of the other populations shown include galaxies $\log M_*/M_\odot > 10$. While only a relatively small fraction of intermediate-z major mergers will result in an extreme compact starburst similar to those in our sample, it is likely that sources like ours are the more extreme, lower-z analogs to compact star forming galaxies more common in the early Universe and are closely related to intermediate-z PSBs.

of them having undergone a recent merger (e.g Sell et al. 2014). In addition to having disturbed morphologies, our galaxies host high velocity ionized and molecular gas outflows which can extend out to kpc scales (e.g. Tremonti et al. 2007; Diamond-Stanic et al. 2012; Geach et al. 2013, 2014; Sell et al. 2014; Geach et al. 2018) or even over 100 kpc scales (Rupke et al. 2019).

In order to understand the evolutionary significance of extreme, compact star formation events like those observed in our galaxies, we need to contextualize their space density relative to that of various phases within massive galaxy, merger-driven evolution. Our results are summarized in Figures 3.7 and 3.8, and we discuss in greater detail within this section.

3.6.1 Evolution of massive compact galaxies

The sample of galaxies we have been studying is comparable to a high-z population of similarly compact, massive forming galaxies. Massive, quiescent galaxies in the Universe at $z > 1.5$ are typically more compact than their local counterparts by roughly a factor of 5 (e.g. Zirm et al. 2007; van Dokkum et al. 2008; van der Wel et al. 2014). The progenitors of these galaxies were likely compact star forming galaxies that were formed in gas-rich mergers of disk galaxies and were then rapidly quenched via some dissipative feedback, a formation scenario that is reminiscent of what we expect for ULIRGs and quiescent galaxies in the lower-z Universe (e.g., Barro et al. 2013; Stefanon et al. 2013; van Dokkum et al. 2015b).

Barro et al. (2013) observed populations of compact quiescent and star forming galaxies in the redshift range $\sim 1 < z < 3$ to understand the evolutionary pathways that lead to the assembly of massive, compact quiescent galaxies we see predominantly in the early Universe. We include their compact star forming galaxy space density evolution as the blue squares in Figure 3.8 for comparison with the intermediate-z massive, compact starburst galaxies we are studying (black star). We adjust the points from Barro et al. (2013) using redshift appropriate stellar mass functions (Moustakas et al. 2013; Adams et al. 2021) to account for the fact that their sample consists of sources with a wider stellar mass distribution than our sample. The adjusted space density is given as

$$n_{\text{adjusted}} = n_{\text{literature}} \times \frac{\int_{\text{lim, us}}^{\infty} \phi_{\text{SMF}} \, \mathrm{d} \log M_*}{\int_{\text{lim, lit}}^{\infty} \phi_{\text{SMF}} \, \mathrm{d} \log M_*}, \tag{3.3}$$

where $n_{\text{literature}}$ is the literature space density calculated for a larger mass range than our sample, and ϕ_{SMF} is the stellar mass function. We use the Moustakas et al. (2013) and Adams et al. (2021) SMFs for $z \leq 1.5$ and $z > 1.5$, respectively. The Barro et al. (2013) compact star forming galaxies have constant space densities at high redshift, but begin to decline at $z <\sim 1.5$. This decline is consistent with the decline in galaxy merger, star formation, and cold gas densities with decreasing redshift (e.g., Tacconi et al. 2010; Daddi et al. 2010; Tacconi et al. 2013; Madau & Dickinson 2014; Riechers et al. 2019).

We show in Figure 3.8 that the space density of our sources lies only slightly below the space density evolution trend shown with the Barro et al. (2013) compact star forming galaxies. We note that our galaxies are more extreme than the Barro et al. (2013) sources as they are both more compact and more rapidly star forming. This likely biases our compact starburst space density to be slightly lower than that for the Barro et al. (2013) galaxies. It is possible that our sources represent the low redshift analogs for an extreme subset of compact starburst galaxies that are more prevalent in the early Universe.

Understanding how stellar feedback rapidly quenches star formation at intermediate redshift is necessary to be able to build models for galaxy formation and evolution in the early Universe when compact star formation events were significantly more common. For compact star-forming galaxies in the early Universe, it is difficult to observe the effects of feedback due to their high redshift and the fact they are commonly obscured by dust, making it nearly impossible to observe UV spectral signatures of outflows (e.g., van Dokkum et al.

2015b). The broad consistency between the space density of our extreme, compact starburst galaxies and the Barro et al. (2013) sample allows us to better understand how compact star formation might be a phase that massive galaxies go through across a wide range of cosmic time.

Barro et al. (2013) also presented a schematic representation of how galaxies evolve onto the local size-mass relation. Within this framework, compact star forming galaxies will experience rapid quenching via AGN or star formation feedback, resulting in a massive, compact quiescent galaxy population. Over cosmic time, these sources will undergo minor and major mergers resulting in a buildup of mass and size (e.g. Naab et al. 2009). If our sources are the low-redshift analogs of early Universe compact star forming galaxies beginning their quenching phase, we would expect that they would also end up as compact, quiescent galaxies. We show the space density evolution from van der Wel et al. (2014) for high-z, massive ($M_* \sim 10^{11}\ M_\odot$), compact ($R/(M_*/M^{11})^{0.75} < 2.5$ kpc) galaxies as red points in Figure 3.8. The space density of compact quiescent galaxies peaks just as that of compact star forming galaxies begins to decline. It then wanes with decreasing redshift due to size buildup via galaxy mergers. Within the lowest redshift bin, the van der Wel et al. (2014) sources have a space density of ~ 10 larger than that of our compact, starburst galaxies. It is also worth noting that the compact quiescent galaxies would be considered to be "compact" for ~ 2 Gyr before minor mergers significantly contribute to size buildup (e.g., Naab et al. 2009; Newman et al. 2012)— a timescale that is significantly longer than the ~ 100 Myr timescale for which our sample would be targeted as extremely compact starbursts (e.g. Barro et al. 2013). In addition to this, the effective radii for the van der Wel et al. (2014) sources is significantly larger than that of our nuclear starbursts. This could be due to the compact quiescent radii being more linked to the stellar mass profiles, while ours might be biased to small values because of mass-to-light ratio (M/L) effects. However, Diamond-Stanic et al. (2021) showed that even accounting for M/L effects that the stellar mass effective radius for our systems is on the order of 0.1-0.5 kpc, which indicates that our population could be even smaller and potentially more extreme than the compact quiescent galaxies in the van der Wel et al. (2014) sample. All of this together suggests that a significant fraction of massive, compact quiescent sources at intermediate redshift could have recently gone through a starburst similar to what we observe for the galaxies in our sample.

3.6.2 Comparison to post starburst galaxies

In order to get a full picture of the role intermediate-z, extremely compact starbursts galaxies play in the buildup of a massive, quiescent population, we also need to understand the evolutionary stages that follow their bursts. By design of our selection criteria, the compact starburst galaxies in our sample are similar to PSBs in that they have B and A-star dominated spectral features and weak nebular emission. Understanding the population of PSBs in a similar redshift interval as our sources would provide context for quenching timescales as well as what the progenitors of PSBs might look like.

Wild et al. (2016) studied a population of massive, PSBs within $0.5 < z < 2$, and determined that PSBs are a relatively short-lived, transitory phase in galaxy evolution, likely lasting $\sim 0.1 - 1$ Gyr (see also Wild et al. 2009). This timescale range was determined by modeling PSBs in both toy-model and hydrodynamic simulations, and evolving them to determine the amount of time they would be targeted as PSBs— a similar method to what we do here for our compact starburst galaxies. The PSBs selectability timescale is given as the blue region in Figure 3.7. Our compact starburst galaxies with selectability timescales of ~ 100 Myr would be selected for $10 - 100\%$ of the time PSBs would be selected by their respective selection criteria.

It would be expected that extremely compact starburst galaxies and PSBs would have similar space densities within a given redshift range if they were two evolutionary stages that were directly related to each other. In other words, if compact starburst galaxies are the immediate progenitors to PSBs, they should be found in similar abundances. This is what is seen in Figure 3.8. The Wild et al. (2016) PSBs within the mass range $10.5 < \log M_*/M_\odot < 12.5$ show a decrease in space density with decreasing redshift. The lowest redshift bin for the Wild et al. (2016) PSBs overlaps with the upper limits of the redshift range probed for our compact starburst galaxies. The mass bin for Wild et al. (2016) is consistent with that of our sources so we did not have to correct for integrating the SMF within different mass intervals. Our sources overlap within the margin of error with the estimated PSB space density at the lowest redshift included in the Wild et al. (2016) sample.

The redshift evolution of the Wild et al. (2016) PSB space density is also consistent with declining star formation and cold-gas densities over cosmic time— properties that would also impact the frequency of extremely compact bursts of star formation (e.g Madau & Dickinson 2014; Riechers et al. 2019). Since the cosmic SFR density sharply declines at low-z, we also want to compare our compact starburst space density to that of low-z PSBs to determine if our calculated space density is consistent with the decline in PSB space density on the interval $0 < z < 1$. We calculate the $z \sim 0.05$ PSB space density by integrating the lowest-z luminosity function presented in Pattarakijwanich et al. (2016). This luminosity function is given per [5000 Å] magnitude, a fiducial top hat filter used to calculate average f_λ across $4950 < \lambda/\text{Å} < 5100$ for the rest frame spectra of the PSBs in their sample. In order to calculate a comparable space density from this, we needed to construct a [5000 Å] mass-luminosity relation to determine our bounds of integration. We did this by calculating [5000 Å] magnitudes from SDSS spectra for the low-z PSBs studied in French et al. (2018) using the methodology described in Pattarakijwanich et al. (2016) and using MPA-JHU stellar masses (Brinchmann et al. 2004; Tremonti et al. 2004). We then integrated the Pattarakijwanich et al. (2016) luminosity function within $10.5 < \log M_*/\text{M}_\odot < 11.5$, which corresponds to $-23.3 < [5000\text{Å}] < -21.3$, to obtain a low-$z$ PSB space density of $\sim (2.9^{+1.2}_{-1.3}) \times 10^{-6}$ Mpc^{-3}. This is given as the green triangle in Figure 3.8. This is of the same order of magnitude of that for our $z \sim 0.5$ compact starburst galaxies, which supports that a fraction of the most extreme PSBs might have undergone an extremely compact starburst phase like that observed in our galaxies.

3.6.3 Comparison to ULIRGs

Within the framework of merger-driven galaxy evolution, it is likely that extremely compact starburst events are most relevant in the remnants of major, gas-rich mergers. We also know that major, gas-rich mergers can trigger strong bursts of dusty star formation which would be observed as a ULIRG with $L_{FIR} > 10^{12}\ L_{\odot}$. It is possible that sources like the massive, extremely compact starburst galaxies in our sample could represent the transition between the dust-obscured ULIRG and the beginning of a galaxy-scale blowout. Here, we compare the selectability timescale and space density of our compact starbursts to that of ULIRGs in order to contextualize their importance in merger-driven galaxy evolution.

The timescales upon which a galaxy will experience ULIRG-like star formation are poorly constrained. On the low end, SN-driven winds could cut the lifetime of a single starburst in a ULIRG to 1-10 Myr (e.g., Thornley et al. 2000). However, studies of ULIRGs with a wide variety of morphologies have allowed the ULIRG lifetime to be estimated to be in the 0.1-1 Gyr range (e.g. Farrah et al. 2001; Murphy et al. 2001; Farrah et al. 2003). It is possible that this wide range of estimated ULIRG lifetimes is due to the fact that it is likely that a ULIRG undergoes multiple large bursts of star formation, allowing it to be selected as such on discontinuous time intervals (e.g., Bekki 2001; Farrah et al. 2001). Farrah et al. (2003) analyzed a population of 41 local ULIRGs and found that most of their sources would have lifetimes $10 \lesssim$ Myr $\lesssim 40$. From all of the values quoted above, we assume that the lifetime of a ULIRG is $\sim 1 - 100$ Myr, and show this range as the purple shaded region in Figure 3.7. However, it is important to make the distinction that these timescales are more strongly related to the physical timescales of dusty star formation than to observable lifetimes caused by respective selection criteria as discussed in other sections. The post-peak SF ages for the MgII galaxies in our sample calculated in Davis et al. (in prep) are better comparisons to the ULIRG lifetimes due to the fact that they are tied more to the physical properties of the galaxies. As stated earlier, Davis et al. (in prep) calculated the average post-peak SF age of ~ 70 Myr, which is largely consistent our estimate that they would be able to be targeted for $\sim 148^{+27}_{-24}$ Myr. These timescales are of a similar order of magnitude to that of ULIRGs, which is largely unsurprising because both types of systems are characterized by their energetic starbursts, albeit ours are a bit more extreme.

We next compare our estimated compact starburst space density to that of ULIRGs in a similar redshift interval. Koprowski et al. (2017) computed the evolution of the far-IR luminosity function for galaxies out to $z \sim 5$. We estimate the observed space density of ULIRGs by adopting the $0.5 < z < 1.5$ far-IR luminosity function presented here. Integrating the luminosity function for $L_{\rm IR} > 10^{12}\ L_\odot$ gives $n_{\rm ULIRG} \sim 6 \times 10^{-5}$ Mpc^{-3}. This is shown as the purple shaded region in Figure 3.8, where the range of values is due to the uncertainty in the Schechter function fit as described in Koprowski et al. (2017). We note that we do not correct for differences in the mass distributions between the ULIRG sample and our sources because ULIRG sample was luminosity selected. Similarly, Magnelli et al. (2009) calculated the evolving far-IR luminosity function and space density for ULIRGs for several redshift bins within the interval $0.4 < z < 1.3$. For the $0.4 < z < 0.7$ and $0.7 < z < 1$ bins, $n_{\rm ULIRG} \sim 3 \times 10^{-5}$ Mpc^{-3} and $n_{\rm ULIRG} \sim 2 \times 10^{-5}$ Mpc^{-3}, respectively.

Comparing these values to our estimated compact starburst space density ($(1.1^{+0.5}_{-0.3}) \times 10^{-6}$ Mpc^{-3}) suggests that it is possible that $\sim 3 - 8\%$ of intermediate-z ULIRGs can experience a phase similar to that observed in our sample of extremely compact starburst galaxies. The physical timescales of ULIRGs and our compact starbursts are driven by the same processes, and they are on the same order of magnitude, while there is a factor $\sim 12 - 40$ difference in their space densities. It is possible the sources in our sample represent a small fraction of the most extreme population of ULIRGs that have the highest SFRs and/or are the most compact.

We also compare the space density of our intermediate-z massive, compact starburst galaxies to that of low-z ULIRGs, similar what we hae done in the previous subsection for PSBs since we expect a sharp decline in the ULIRG space density alongside that of the cosmic SFR density (e.g., Madau & Dickinson 2014). Kim & Sanders (1998) presented a luminosity function for $0.05 < z < 0.2$ ULIRGs, and integrating the luminosity for $\log\ L_{\rm IR}/{\rm L}_{\odot} > 12$ gives a space density of $\sim (4 \pm 1) \times 10^{-7}$ Mpc^{-3}. This is given as the purple hexagon in Figure 3.8. Given that the space density of our intermediate-z, compact starburst galaxies is calculated in a redshift range between that of the low and intermediate-z ULIRGs, this very steep decline in ULIRG space density also suggests that a small fraction of ULIRGs could undergo a phase like that observed in our galaxies as they evolve.

3.6.4 Comparison to $z \sim 0.5$ merger rate per co-moving unit volume

Since extremely compact starburst galaxies are likely formed by the merging of gas-rich disk galaxies, it is important to characterize how many major mergers could produce events like those observed in our sample of galaxies. This requires having knowledge of the major merger rate over a given redshift range. In the past few decades, much work has been done to constrain the galaxy-galaxy merger rate throughout cosmic time. However, there are large systematic uncertainties in this measurement that have prevented the reaching of a consensus between theory and observations and even between different observational techniques. Here, we summarize the most recent results in calculating the $z \sim 0.5$ galaxy merger rate per co-moving unit volume and use them to contextualize our compact starburst space density. To be more concise, we will refer to the merger rate per co-moving unit volume as the merger rate density for the rest of this paper.

A crucial piece of calculating the galaxy merger rate density is understanding the timescales upon which a system would be identified as a major merger. This is also the aspect of the calculation that contributes the most uncertainty to the major merger rate density. The two main methods to identify merging galaxies are to select systems with disturbed morphologies (e.g., Abraham et al. 1994, 2003; Conselice 2009; Lotz et al. 2008) or to search for systems comprised of close pairs (e.g, Le Fèvre et al. 2000; Bluck et al. 2009). Each of these methods probe different stages of the merger and are susceptible to different biases. Close pair selection identifies sources before the merger begins but morphological selection can detect systems before, during, and after the merger occurs, allowing morphologically selected galaxy mergers to be identifiable on different timescales than their close pair counterparts.

In Figure 3.7, we compare the selectability timescale calculated for our modeled compact starburst galaxies (black star) to that of all galaxy mergers presented in Lotz et al. (2008) (grey shaded region). The Lotz et al. (2011) region reflects the range of timescales calculated for simulated systems with mass ratios $1 : 10 < \mu < 1 : 1$ that were selected morphologically (for a detailed review; Abraham et al. 1994, 2003; Lotz et al. 2011). We find that extreme compact starburst events are selectable for a fraction of the amount of time that a morphologically selected galaxy merger would be under its own respective criteria.

Having constraints on galaxy merger timescales allows for the merger rate density to be calculated. We show our calculated compact starburst space density (black star) in conjunction with merger rate densities (grey and red shaded regions) as well as the space densities of other phases of merger-driven evolution in Figure 3.8. The grey shaded region represents the range of the predicted observable merger rate densities calculated in Lotz et al. (2011), and the red shaded region represents the observed range of merger rate densities presented in Stott et al. (2013) which used Lotz et al. (2011) predicted observable timescales. Both the Lotz et al. (2011) and Stott et al. (2013) merger rate densities were calculated for samples containing galaxies with $\log M_*/M_\odot > 10$, while the compact starburst galaxies in our sample are typically $\log M_*/M_\odot > 10.5$. We therefore adjusted the Lotz et al. (2011) and Stott et al. (2013) merger rate densities to ensure that we are working within the same mass interval of the galaxy stellar mass function (SMF) within the appropriate redshift range, as described above. We also converted these merger rate densities to merger space densities by assuming a typical merger timescale of 0.5 Gyr (Lotz et al. 2011).

We find that our estimated massive compact starburst space density is ~ 200 times smaller than the merger rate density within a similar redshift interval, suggesting that only a small fraction of galaxy mergers would trigger an extreme burst of compact star formation similar to our observed sample. However, we reiterate that the Lotz et al. (2011) and Stott et al. (2013) merger rates consider both major and minor mergers. It is likely that these compact starburst events are triggered only by gas-rich major (mass ratio 1:1 - 4:1) mergers which only make up a fraction of the total number of mergers occurring across a given redshift range (e.g., Lin et al. 2010). This suggests that although only a small fraction of all galaxy mergers might result in extremely compact starbursts, that these could be a likely result of a larger fraction of gas-rich major mergers.

3.6.5 Comparison to $z \sim 0.5$ massive, quiescent galaxies

Another way of understanding the role of compact starburst galaxies in the buildup of quiescent galaxy populations is to compare their space density to that of massive, quiescent galaxies within the same redshift range. Moustakas et al. (2013) presented a detailed study of galaxies targeted in PRism Multi-object Survey (PRIMUS) and provided contsraints on the evolution of the stellar mass function from $0 < z < 1$. The galaxies in PRIMUS were sorted into star forming and quiescent populations, and the evolution of their space density was calculated across different stellar mass and redshift bins. For quiescent PRIMUS galaxies in the mass range $10.5 < \log M/M_{\odot} < 11$, their space density increases by $\sim 2 \times 10^{-4}$ Mpc^{-3} from $z \sim 0.8$ to $z \sim 0.35$. The net decline in space density for star forming galaxies in this redshift interval is $\sim 9 \times 10^{-5}$ Mpc^{-3}. These changes in space density are comparable to the merger rate in this redshift range and are a factor of ~ 1000 larger than our measured space density of $n \sim (1.1^{+0.5}_{-0.3}) \times 10^{-6}$ Mpc^{-3} for our sample of massive, compact starburst galaxies. This is broadly consistent with short-lived compact starbursts existing for ~ 100 Myr, evolving into massive, quiescent galaxies which would exist on ∼Gyr timescales. It is likely that this is a relatively rare phase of galaxy evolution within the general population of massive, quiescent galaxies. However, it is possible that the fraction of those that have also previously undergone extreme ULIRG or PSB phases also could have experienced extremely, compact starbursts like those in our sample.

3.7 Summary & Conclusions

In order to build up a population of quiescent galaxies, otherwise gas-rich and star forming galaxies need to undergo some type of quenching process to either disrupt or expel the gas in the system. Violent, dissipative feedback in which either AGN activity or rapid star formation injects energy into the ISM is an important process that impedes the formation of stars in a galaxy. Observationally, feedback manifests as large-scale gas outflows being driven from a galaxy.

Within the context of merger-driven galaxy evolution, we expect gas-rich mergers of massive star forming galaxies to trigger dusty starburst events that would then be followed by a blowout event in which nuclear gas and dust is expelled from the system, therefore exposing the nuclear regions of the galaxy. In this work, we have studied a population of 115 $z \sim 0.5$ massive galaxies that are experiencing extreme, compact starburst events and outflows. Resolved *HST* WFC3 observations of a subset of these show that they are merger remnants, suggesting that these types of events could be an phase within a simple merger-driven evolutionary pathway.

Our goal for this work was to determine how long galaxies like the ones we observe would be selected under a certain set of selection criteria, to estimate their space density, and to place them into cosmological context with other evolutionary phases massive galaxies could experience. We do this by empirically modeling the stellar populations of $z \sim 0.5$ massive, compact starburst galaxies. Our model is dependent on four parameters: nuclear burst age, burst mass fraction, optical depth of dust enshrouding newly formed stars, and total galaxy stellar mass. These posterior distributions for these parameter values are constrained for each of the 115 galaxies in our sample by fitting the SDSS $ugriz$ and *WISE* W1/W2 photometry for the 151 galaxies in our sample using an MCMC technique. We randomly draw sets of parameters from the Gaussian models for the MCMC-calculated posterior distributions to assemble a mock population of compact starburst galaxies. We evolve the modeled sources to determine the timescales under which the galaxies we model would be selected by our targeting criteria. We find that this timescale is 148^{+27}_{-24} Myr and that the corresponding intrinsic space density is $n_{\mathrm{CS}} \sim (1.1^{+0.5}_{-0.3}) \times 10^{-6}$ Mpc^{-3}.

Our results, as summarized in Figure 3.8, suggest that our observed population of extreme compact starburst galaxies could fit into an evolutionary scheme described in Barro et al. (2013). At higher redshifts massive, compact star forming galaxies are more common, and they are believed to be the progenitors of massive, compact quiescent galaxies. Based on comparisons with the Barro et al. (2013) sample of massive, compact galaxies it is likely that our sources follow a similar life cycle in which a gas-rich major merger triggers a burst of star formation. This starburst then drives massive, high velocity gas outflows, thus rapidly quenching the galaxy. This galaxy would be observable for ~ 100 Myr timescales as a PSB (e.g., Wild et al. 2016), and would then evolve into a massive, compact, quiescent galaxy. Throughout cosmic time, the massive, quiescent galaxy will undergo minor mergers, allowing it to grow in both mass and size to become a typical quiescent galaxy consistent with the mass-size relation of the massive quiescent galaxy population at z=0, which is notably devoid of compact quiescent galaxies (e.g., Taylor et al. 2010). Although it is more common for galaxies to experience this timeline earlier in the Universe, our galaxies appear to be consistent with these trends within their respective redshift interval. The space density of our massive, compact starbursts suggests that they can contribute to the buildup of a fraction of PSBs and massive, extreme compact quiescent galaxies within their epoch, which in turn could contribute to the overall population of massive, quiescent galaxies in the future.

3.8 Auxillary MCMC Output

Table 3.1: Properties for the galaxies included in our sample.

SDSS ID (1)	z (2)	$\langle \log M_*/M_\odot \rangle$ (3)	$\sigma_{\log M_*/M_\odot}$ (4)	SDSS u (AB) (5)	SDSS g (AB) (6)	SDSS r (AB) (7)	SDSS i (AB) (8)	SDSS z (AB) (9)	*WISE* W1 (Vega) (10)	*WISE* W2 (Vega) (11)
J1015+0004	0.417	11.0	0.07	22.03	20.71	19.25	18.95	18.77	15.83	15.38
J1109-0040	0.593	11.4	0.47	22.07	20.88	19.46	18.8	18.61	15.26	15.22
J1210+0030	0.441	11.1	0.08	21.88	20.87	19.37	19.02	18.79	15.87	15.3
J1341-0009	0.446	11.0	0.19	22.34	20.96	19.38	19.05	18.79	15.74	15.74
J1434-0052	0.461	11.3	0.51	23.45	21.04	19.29	18.66	18.31	14.86	14.64
J1440+0039	0.564	11.2	0.10	20.93	20.4	19.27	18.86	18.74	15.59	15.59
J1125-0145	0.519	10.9	0.27	19.6	19.33	18.69	18.48	18.39	14.84	14.65
J0745+3754	0.406	10.7	0.22	20.27	19.86	19.14	18.79	18.46	14.78	14.13
J0251-0657	0.406	11.1	0.27	22.91	21.14	19.39	18.88	18.57	15.38	15.19
J0905+5759	0.711	10.8	0.28	19.91	19.58	19.4	19.1	19.14	15.56	15.46
J1219+0336	0.451	11.0	0.21	20.15	19.52	18.79	18.53	18.33	14.99	14.56
J1232+0226	0.418	11.1	0.22	21.55	20.36	18.81	18.53	18.4	15.41	15.25
J1440+0107	0.456	10.9	0.23	20.63	20.26	19.38	18.97	18.76	15	14.53
J1441+0116	0.537	11.0	0.22	20.35	19.76	19.34	18.97	18.68	15.33	15.1
J0901+0314	0.459	10.6	0.23	19.55	19.29	18.82	18.7	18.57	15.22	15.01
J1107+0417	0.467	10.6	0.22	19.96	19.52	19.07	18.89	18.7	15.58	14.93
J1453+6022	0.406	10.9	0.15	20.49	20.04	19.02	18.78	18.55	15.61	15.33
J1506+6131	0.437	10.3	0.17	19.69	19.58	19.12	19.04	19.16	15.72	15.52
J1610+5104	0.469	11.1	0.07	22.1	20.93	19.35	18.92	18.76	15.68	15.51
J1635+4709	0.699	11.6	0.13	20.65	20.28	19.51	18.75	18.56	15.21	15.11
J2116-0634	0.728	11.3	0.18	20.74	20.02	19.72	19.2	19.05	15.51	15.55
J2311-0839	0.725	11.7	0.14	21.15	20.89	19.93	18.92	18.71	15.4	15.29
J2140+1209	0.751	11.1	0.25	20.63	20.19	19.85	19.31	19.1	15.57	14.98
J2256+1504	0.727	11.4	0.22	20.76	20.1	19.59	18.91	18.74	15.12	15.19
J2319+1435	0.422	10.5	0.36	22.62	21.07	19.42	19.01	18.78	15.77	15.44
J0826+4305	0.603	10.7	0.27	19.64	19.43	19.14	18.88	18.85	15.42	15.13
J0951+5514	0.402	11.3	0.11	20.65	20.01	18.91	18.51	18.15	14.85	14.37
J1235+6140	0.599	11.3	0.48	20.91	20.31	19.19	18.61	18.51	15.4	15.13
J1253+6256	0.536	10.4	0.17	19.69	19.64	19.3	19.25	19.22	16.16	15.68
J1506+5402	0.608	10.7	0.27	19.28	19.13	18.88	18.65	18.61	15.26	14.78
J1248+0601	0.632	11.2	0.18	20.89	20.33	19.49	18.98	18.85	15.77	15.64
J1117+5123	0.49	11.3	0.11	21.06	20.42	19.24	18.91	18.68	15.33	15.38
J1020+5331	0.457	11.0	0.31	22.53	20.68	19.21	18.88	18.69	15.77	15.62
J1401-0223	0.402	11.0	0.20	20.36	19.91	19.05	18.64	18.29	15.01	14.54

J0933+4135	0.441	10.7	0.25	19.07	18.97	18.46	18.39	18.24	15.14	14.59
J0939+4251	0.411	10.9	0.17	20.05	19.58	18.73	18.52	18.24	15.18	14.89
J1142+6037	0.568	11.5	0.29	20.86	20.13	18.81	18.29	18.17	15.05	14.79
J1713+2817	0.577	11.3	0.16	20.82	20.3	19.33	18.91	18.86	15.52	15.23
J1720+3017	0.684	11.6	0.10	21.25	20.67	19.75	18.89	18.78	15.45	15.47
J2118+0017	0.459	10.8	0.25	20.17	19.78	18.96	18.74	18.53	14.96	14.25
J0922+0452	0.476	11.1	0.08	21.22	20.34	18.99	18.79	18.57	15.7	15.49
J1052+0607	0.555	10.9	0.14	20.53	20.14	19.32	19	18.86	15.69	15.82
J1353+5300	0.408	11.3	0.18	20.43	19.84	18.81	18.38	18.12	14.65	14.2
J1436+5017	0.454	11.0	0.19	20.22	19.81	18.83	18.61	18.42	15.36	14.91
J1558+3957	0.402	10.6	0.23	19.37	19.07	18.54	18.44	18.24	15.17	14.55
J1604+3939	0.564	11.7	0.29	20.85	20.01	18.8	18.21	18.06	14.58	14.48
J0828+0336	0.572	11.0	0.11	20.9	20.3	19.3	18.98	18.94	16.09	15.77
J0808+2709	0.563	11.1	0.19	20.63	20.09	19.4	18.9	18.77	15.52	14.94
J1009+4336	0.519	10.9	0.26	19.6	19.37	18.79	18.56	18.38	14.98	14.62
J1133+0956	0.483	11.0	0.19	20.45	19.93	19.05	18.8	18.75	15.2	14.95
J0900+3212	0.496	11.3	0.22	20.18	19.84	18.96	18.5	18.14	14.67	14.49
J1330+4821	0.444	11.5	0.16	20.6	19.73	18.76	18.32	17.97	14.64	14.13
J1420+5313	0.742	11.8	0.20	20.72	20.39	19.84	19.01	18.67	14.68	14.61
J1556+4234	0.401	11.4	0.11	20.42	19.76	18.52	18.19	17.88	14.8	14.38
J1456+3849	0.421	10.8	0.23	19.84	19.48	18.88	18.49	18.16	14.44	13.8
J1459+3844	0.433	10.5	0.22	19.93	19.64	19.05	18.9	18.68	15	14.56
J1037+4048	0.439	11.1	0.16	22.17	20.94	19.4	18.98	18.74	15.74	15.56
J1248+4444	0.43	10.7	0.22	19.71	19.49	18.83	18.62	18.48	15.14	14.76
J1447+3650	0.414	11.0	0.06	22.71	20.89	19.17	18.84	18.72	15.7	15.58
J1520+3334	0.516	11.3	0.12	21.91	20.78	19.39	18.98	18.88	15.41	15.18
J1611+2650	0.483	11.4	0.13	20.97	20.18	18.97	18.67	18.45	14.92	14.62
J1039+4537	0.634	11.2	0.26	20.37	20	19.42	18.98	18.86	15.02	14.87
J1035+3854	0.422	11.0	0.29	22.44	20.8	19.26	18.96	18.75	15.85	15.59
J1052+4104	0.576	10.9	0.18	20.14	19.84	19.27	18.96	18.89	15.78	15.74
J1215+4233	0.479	11.2	0.33	22.22	20.86	19.21	18.82	18.58	15.48	15.22
J1244+4140	0.459	10.8	0.18	19.91	19.54	18.79	18.64	18.45	15.71	15.15
J0921+3251	0.73	11.1	0.41	26.53	15.87	14.65	16.92	16.62	15.01	14.96
J1012+1134	0.411	11.0	0.42	24.01	21.22	19.6	19.07	18.79	15.43	14.81
J1113+1119	0.628	11.6	0.63	20.57	17.48	17.04	16.68	16.5	15.49	15.43
J1232+0723	0.401	10.7	0.22	19.86	19.41	18.73	18.6	18.42	14.96	14.7
J1239+0731	0.542	11.0	0.18	20.51	20.12	19.29	18.95	18.85	15.62	15.49
J1415+4830	0.496	11.0	0.21	19.66	19.2	18.73	18.34	18.08	14.12	13.4
J1450+4621	0.782	11.6	0.15	20.6	20.09	19.66	18.89	18.85	15.24	15.23
J1658+2354	0.498	11.4	0.17	19.74	19.22	18.33	18.07	17.94	14.54	14.36
J0908+1039	0.502	11.0	0.23	19.77	19.45	18.74	18.47	18.27	14.89	14.6

J1119+1526	0.491	11.1	0.07	22.09	20.95	19.43	19.04	18.87	15.82	15.66
J0830+5552	0.526	11.0	0.25	20.19	19.85	19.16	18.81	18.56	14.82	14.49
J1435+0846	0.404	11.3	0.15	20.28	19.73	18.61	18.32	18.05	14.99	14.56
J0742+4844	0.431	11.0	0.14	20.79	20.19	19.03	18.83	18.59	15.6	15.19
J0752+1806	0.619	10.5	0.13	20.44	19.91	19.5	19.03	20.65	14.66	14.32
J0836+2526	0.531	10.8	0.23	20.75	20.29	19.28	18.94	18.8	16.12	15.82
J1016+3026	0.402	10.8	0.30	23	20.8	19.18	18.83	18.64	15.72	16.02
J1133+3958	0.487	11.1	0.21	19.7	19.29	18.52	18.29	18.15	14.74	14.46
J1229+3545	0.614	11.4	0.41	20.57	20	19	18.46	18.33	15.18	15.1
J1301+3615	0.573	11.3	0.19	20.51	20.01	19.13	18.68	18.59	15.05	14.91
J0901+2338	0.438	10.8	0.23	20.06	19.45	18.96	18.58	18.39	14.39	13.7
J0911+2619	0.471	11.0	0.24	20.18	19.71	18.95	18.58	18.36	14.5	13.92
J1403+2440	0.455	11.0	0.15	22.2	20.79	19.24	18.93	18.76	15.77	15.69
J1505+2312	0.417	11.0	0.07	22.6	20.89	19.33	18.98	18.71	15.78	15.39
J1548+1834	0.688	11.2	0.22	20.53	20.08	19.55	18.93	18.89	15.37	15.31
J1634+1729	0.491	10.9	0.23	20.71	20.1	19.35	19.04	18.78	15.22	14.54
J1635+1749	0.469	11.0	0.24	20.71	20.17	19.21	18.93	18.75	15.08	14.67
J1226+2753	0.427	10.3	0.14	19.14	19.14	18.83	18.81	18.78	15.87	15.46
J0936+2237	0.571	11.3	0.49	22.66	21.12	19.48	18.86	18.63	15.41	15.34
J1012+2258	0.504	11.5	0.20	20.74	20.13	18.81	18.43	18.21	14.89	14.69
J1000+2816	0.469	11.2	0.14	20.74	20.25	19.17	18.76	18.56	15.22	15.22
J0941+1827	0.569	11.5	0.14	21.02	20.26	19.1	18.61	18.36	15.2	14.97
J1005+1836	0.402	10.8	0.33	24.96	21.13	19.48	19.02	18.79	15.7	15.56
J0912+1523	0.747	11.7	0.29	20.91	20.37	19.59	18.64	18.4	15.23	15.06
J0900+1130	0.407	11.2	0.21	20.64	19.97	19.04	18.62	18.18	14.66	14.04
J1203+1807	0.595	11.4	0.38	22.37	21.25	19.73	18.96	18.82	15.41	15.38
J1205+1818	0.526	10.6	0.27	19.01	18.88	18.54	18.41	18.45	15.19	14.84
J1256+1826	0.424	11.0	0.39	22.52	21.02	19.35	18.88	18.6	15.42	15.27
J1248+1954	0.561	11.0	0.17	20.15	19.8	19.13	18.81	18.79	15.68	15.65
J1352+1653	0.533	11.3	0.32	22.07	21.07	19.47	18.88	18.63	15.57	15.36
J1400+1524	0.564	11.3	0.15	20.72	20.35	19.35	18.86	18.76	15.38	15.24
J1412+1635	0.454	11.1	0.39	22.5	20.91	19.3	18.88	18.57	15.5	15.21
J1412+1943	0.413	10.9	0.20	21.76	20.68	19.26	19	18.75	15.79	15.57
J1500+1739	0.577	10.7	0.27	19.68	19.38	19.04	18.82	18.76	15.15	14.82
J1516+1650	0.589	11.0	0.24	19.73	19.35	18.93	18.54	18.35	14.46	13.95
J1049+6433	0.454	11.4	0.38	21.79	20.36	18.78	18.35	18.13	15	14.71
J1528+0126	0.403	10.9	0.22	20.3	19.78	19.03	18.62	18.23	14.53	14.06
J0811+4716	0.516	11.0	0.11	21.16	20.69	19.55	19.2	18.92	15.93	15.87
J0827+2954	0.682	11.5	0.11	21.48	21.05	20.12	19.42	19.14	15.69	15.48
J1613+2834	0.449	11.0	0.24	20.26	19.76	18.94	18.69	18.42	14.84	14.25

Table 3.2 Comparison between our derived stellar masses and those presented in Sell et al. (2014).

SDSS Name (1)	$\langle \log M_*/M_\odot \rangle$ (This work) (2)	$\log M_*/M_\odot$ (Sell et al. 2014) (3)
J1506+6131	$10.3^{+0.22}_{-0.15}$	10.2
J0826+4305	10.7 ± 0.29	10.8
J2118+0017	$10.8^{+0.22}_{-0.27}$	11.1
J1558+3957	10.6 ± 0.24	10.6
J1613+2834	$11.0^{+0.17}_{-0.24}$	11.2

Note. — Average $\log M_*/M_\odot$ and $\sigma_{\log M_*/M_\odot}$ were computed in the MCMC fitting routine described above.

Note. — These derived masses are broadly consistent with one another.

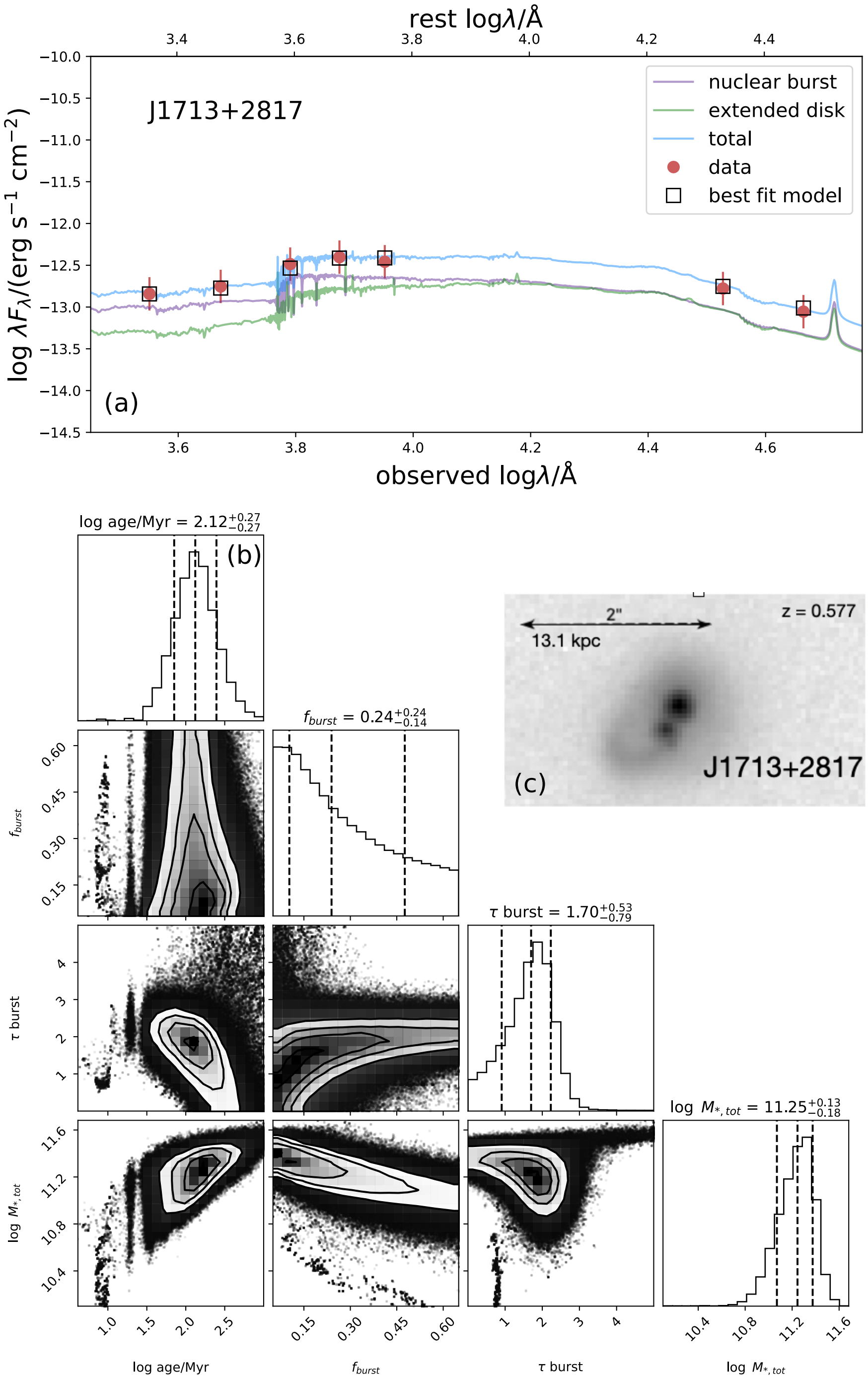

Figure 3.9 *Panel (a)*: Best fit SED for galaxy J01713+2817. The red points and error bars are the observed photometry and ± 0.25 magnitude uncertainty region, respectively. The open black squares are the modeled photometry. The blue, violet, and green curves are the modeled SED for the total galaxy system, nuclear burst, and host galaxy, respectively. *Panel (b)*: Triangle plot of parameter posterior distributions for galaxy J01713+2817. We calculate the mean and covariances of these posterior distributions to model them as 4D-Gaussian distributions. We then randomly draw sets of parameter values from the Gaussian-modeled posterior to construct a mock population of compact starbursts. *Panel (c)*: Galaxy cutout as seen in Figure 4.1.

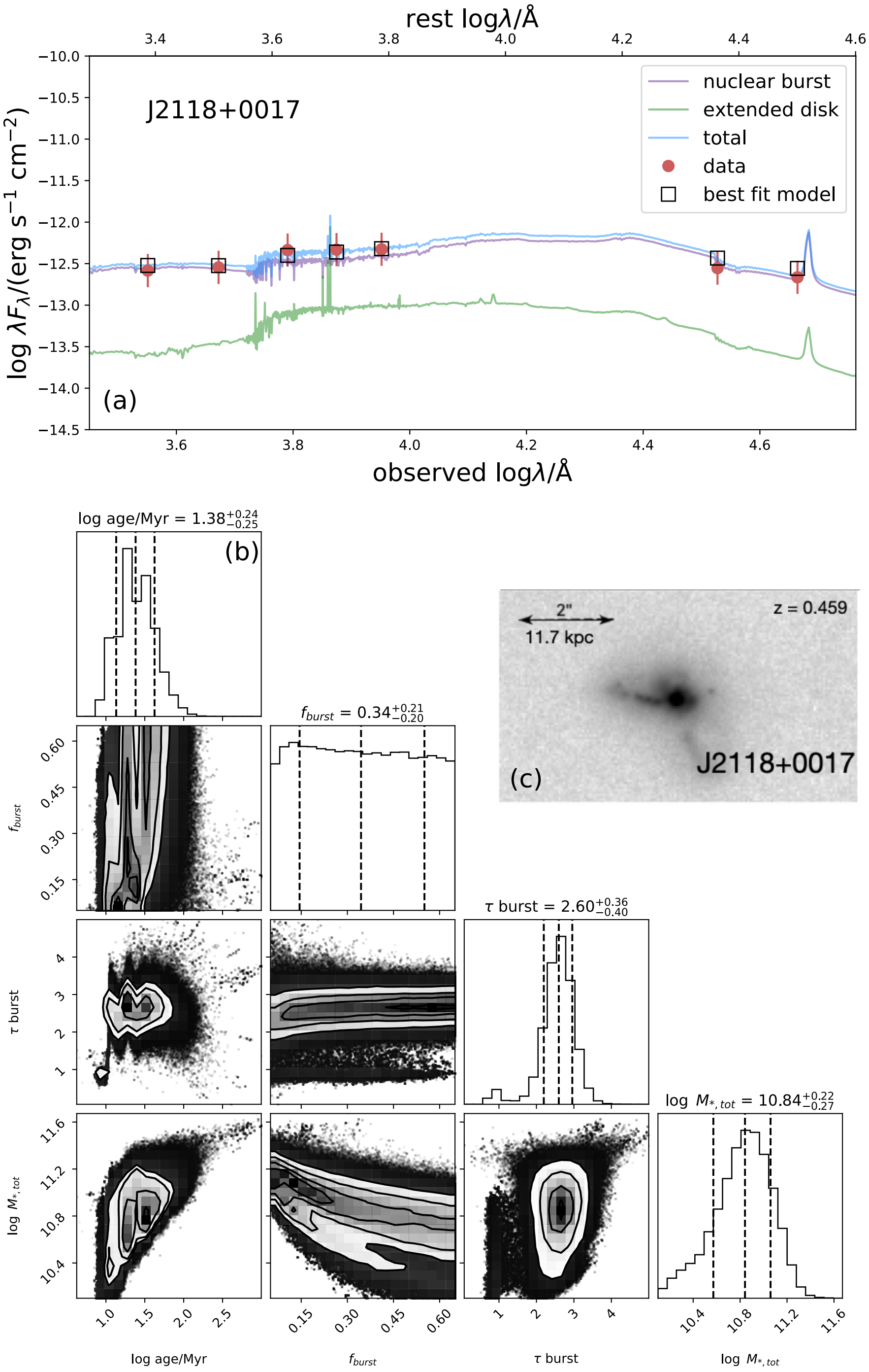

Figure 3.10 *Panel (a)*: Best fit SED for galaxy J2118+0017. The red points and error bars are the observed photometry and ± 0.25 magnitude uncertainty region, respectively. The open black squares are the modeled photometry. The blue, violet, and green curves are the modeled SED for the total galaxy system, nuclear burst, and host galaxy, respectively. *Panel (b)*: Triangle plot of parameter posterior distributions for galaxy J2118+0017. We calculate the mean and covariances of these posterior distributions to model them as 4D-Gaussian distributions. We then randomly draw sets of parameter values from the Gaussian-modeled posterior to construct a mock population of compact starbursts. *Panel (c)*: Galaxy cutout as seen in Figure 4.1.

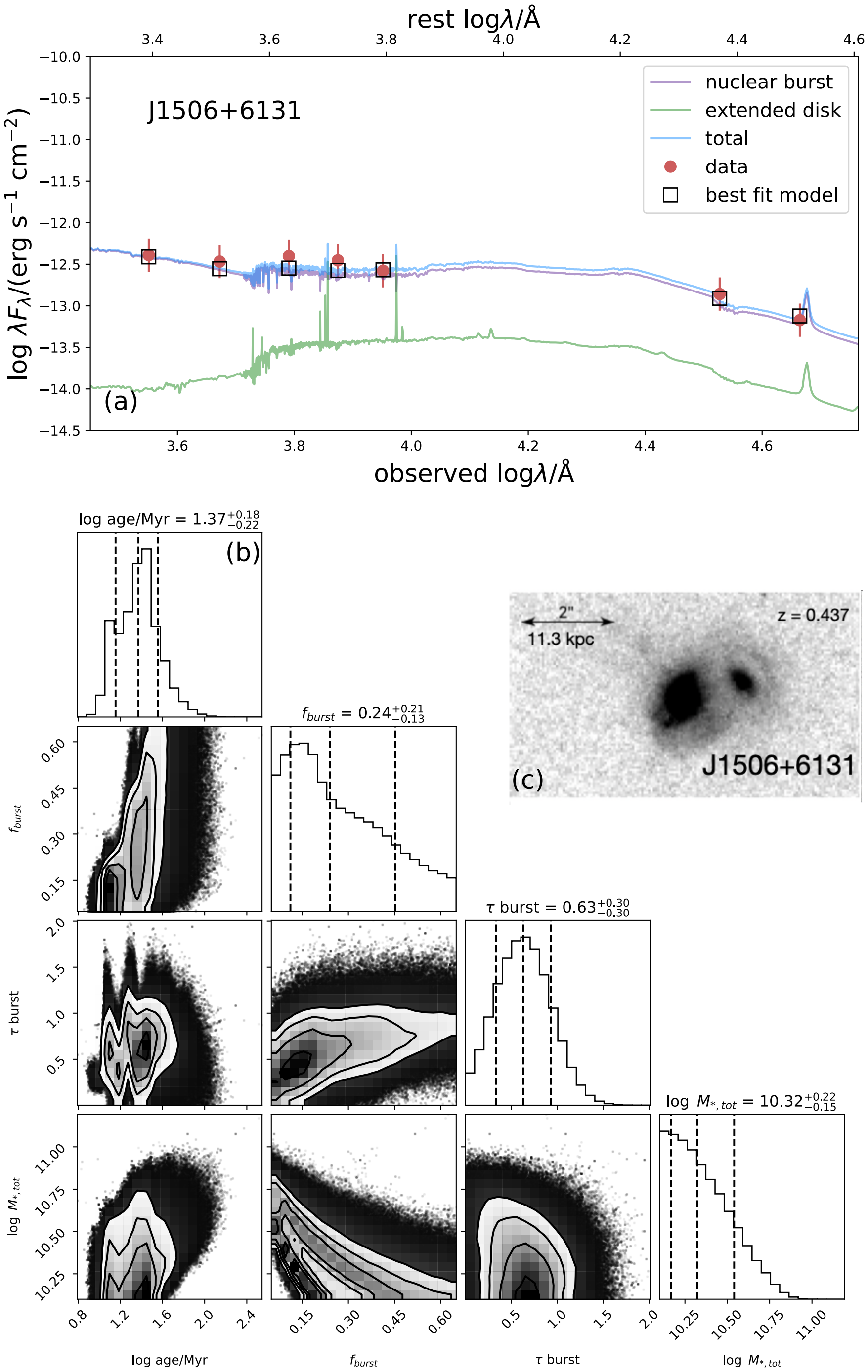

Figure 3.11 *Panel (a)*: Best fit SED for galaxy J1506+6131. The red points and error bars are the observed photometry and ± 0.25 magnitude uncertainty region, respectively. The open black squares are the modeled photometry. The blue, violet, and green curves are the modeled SED for the total galaxy system, nuclear burst, and host galaxy, respectively. *Panel (b)*: Triangle plot of parameter posterior distributions for galaxy J1506+6131. We calculate the mean and covariances of these posterior distributions to model them as 4D-Gaussian distributions. We then randomly draw sets of parameter values from the Gaussian-modeled posterior to construct a mock population of compact starbursts. *Panel (c)*: Galaxy cutout as seen in Figure 4.1.

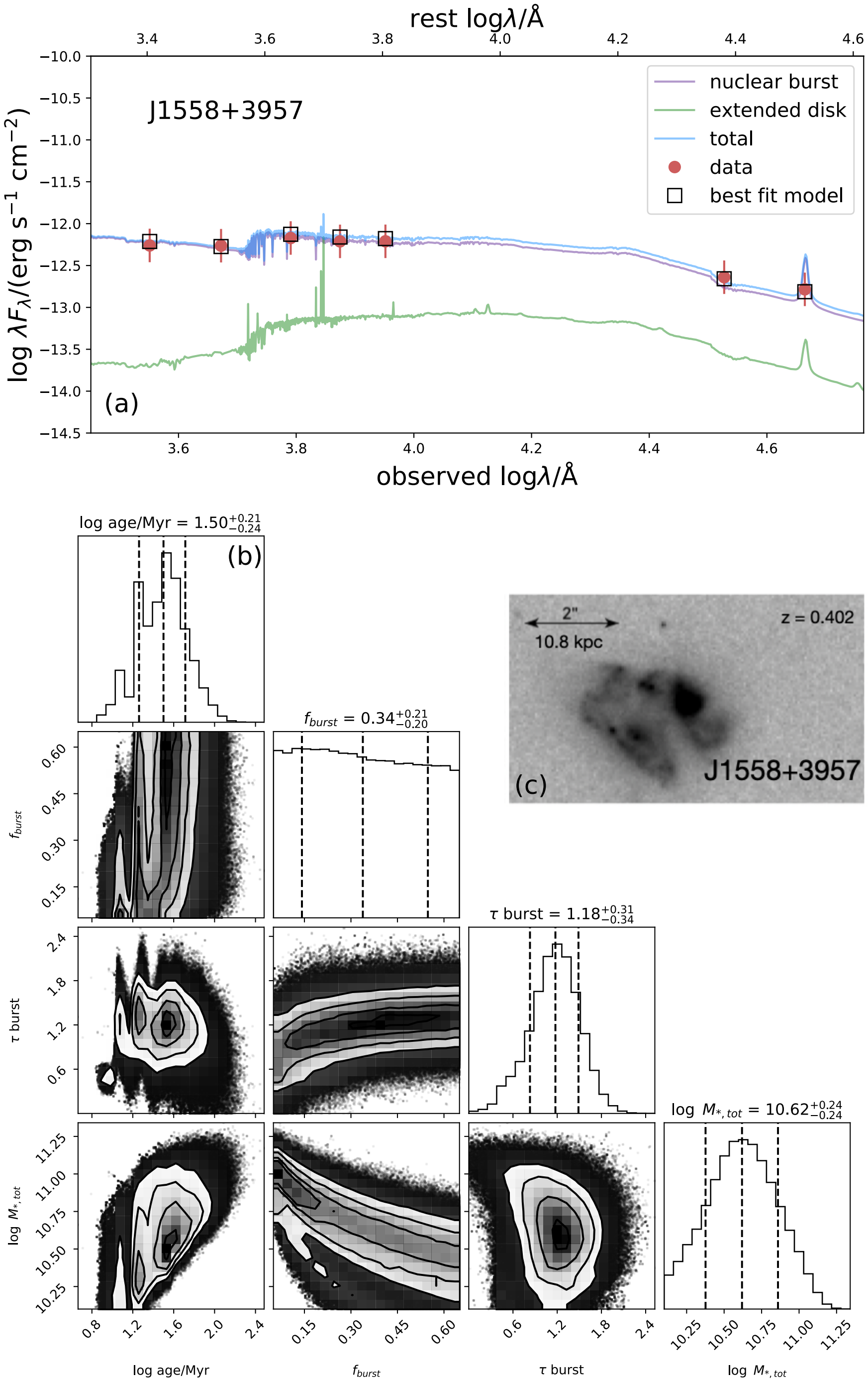

Figure 3.12 *Panel (a)*: Best fit SED for galaxy J1558+3957. The red points and error bars are the observed photometry and ± 0.25 magnitude uncertainty region, respectively. The open black squares are the modeled photometry. The blue, violet, and green curves are the modeled SED for the total galaxy system, nuclear burst, and host galaxy, respectively. *Panel (b)*: Triangle plot of parameter posterior distributions for galaxy J1558+3957. We calculate the mean and covariances of these posterior distributions to model them as 4D-Gaussian distributions. We then randomly draw sets of parameter values from the Gaussian-modeled posterior to construct a mock population of compact starbursts. *Panel (c)*: Galaxy cutout as seen in Figure 4.1.

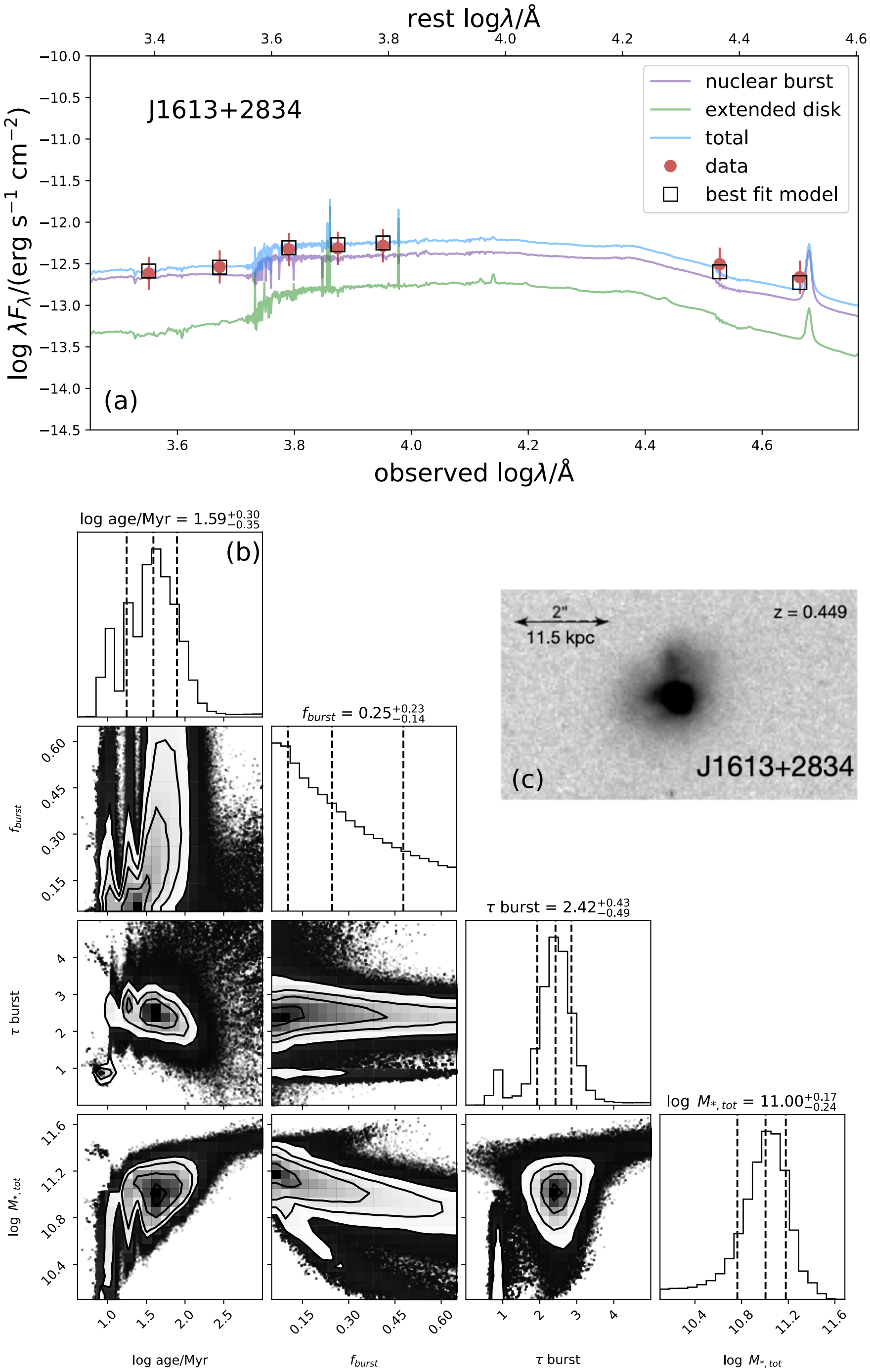

Figure 3.13 *Panel (a)*: Best fit SED for galaxy J1613+2834. The red points and error bars are the observed photometry and ±0.25 magnitude uncertainty region, respectively. The open black squares are the modeled photometry. The blue, violet, and green curves are the modeled SED for the total galaxy system, nuclear burst, and host galaxy, respectively. *Panel (b)*: Triangle plot of parameter posterior distributions for galaxy J1613+2834. We calculate the mean and covariances of these posterior distributions to model them as 4D-Gaussian distributions. We then randomly draw sets of parameter values from the Gaussian-modeled posterior to construct a mock population of compact starbursts. *Panel (c)*: Galaxy cutout as seen in Figure 4.1.

Chapter 4

Longslit Spectroscopy of Ultra-puffy Galaxy Candidates with SALT

Kelly E. Whalen (Dartmouth College), Ryan C. Hickox (Dartmouth College), Joshua Perlmutter (Brandeis University), Andy D. Goulding (Princeton University), Jenny Greene (Princeton University), Jiaxuan Li (Princeton University)

This is work that is being prepared for future publication.

4.1 Introduction

Although they are among the most numerous galaxies in the Universe, low-mass dwarf ($\lesssim 10^9\ M_\odot$) galaxies challenge our understanding of the processes that drive galaxy formation and evolution (e.g., Somerville & Davé 2015; Weinberg et al. 2015). Dwarf galaxies reside in shallow gravitational wells, are dark matter dominated, and are typically are less metal enriched than more massive galaxies at a given redshift, making them excellent targets to test the limits of baryonic and dark matter-related galaxy formation processes (e.g., Tremonti et al. 2004; Bullock & Boylan-Kolchin 2017; Sales et al. 2022).

An elusive subset of dwarf galaxies have central surface brightnesses that are fainter than that of the ambient night sky, earning them the name of low surface brightness galaxies (LSBGs; e.g., Impey & Bothun 1997). The extreme faintness of the LSBG population introduces a host of observational challenges since they are exceedingly difficult to detect in blind optical surveys, biasing our known galaxy population to being brighter than it intrinsically is (e.g. Disney 1976). The most extremely faint subgroup of LSBGs are size-mass outliers that have dwarf-like stellar masses and optical effective radii comparable to the Milky Way (e.g., van Dokkum et al. 2015a). These ultra-diffuse galaxies (UDGs) have been preferentially found in high abundances in high-density cluster environments (van Dokkum et al. 2015b; Koda et al. 2015; van der Burg et al. 2016; Ruiz-Lara et al. 2018), but they can also reside in galaxy groups (e.g., Román & Trujillo 2017; van der Burg et al. 2017), and isolated in the field (e.g., Martínez-Delgado et al. 2016; Leisman et al. 2017).

The formation mechanisms responsible for creating populations of UDGs are uncertain, but it is possible that they vary dependending on large-scale environment. For example, the overabundance of UDGs in high density environments suggest that its possible that they are failed L_* galaxies that underwent a gas removal process such as ram-pressure stripping, strangulation, starvation, or harrassment early in their lifetimes (e.g., Gunn & Gott 1972; Larson et al. 1980; Mihos 2004; van Gorkom 2004; van Dokkum et al. 2015a; Yozin &

Bekki 2015; Baushev 2018; Tremmel et al. 2020). For field UDGs, it is possible that they might have also experienced environmental stripping earlier in their formation as they passed through cosmic web filaments, and are just now being observed in isolation (e.g. Benavides et al. 2021). Λ-Cold Dark Matter (ΛCDM) galaxy formation models and weak lensing observations suggest that UDGs could also be the result of galaxies forming in dwarf-mass ($\lesssim 10^{10}\ M_{\odot}$) dark matter halos with high angular momentum (e.g., Amorisco & Loeb 2016; Sifón et al. 2018; Kong et al. 2022). Isolated UDGs are typically blue and star forming, consistent with other proposed formation scenarios where feedback from massive stars and supernovae drive outflows and deplete gas reservoirs (e.g., Di Cintio et al. 2017; Mancera Piña et al. 2020).

Much of our understanding of dwarf galaxies in general comes from MW and local group satellites (e.g., Simon 2019). Therefore, it is of interest to characterize UDGs that are satellites of MW analogs so they can be compared to more tyipcal dwarf galaxy populations (e.g., Goto et al. 2023). Satellite UDGs could be formed from any or all of the proposed mechanisms described above, but they can also be the remnants of accreted field UDGs or "normal" dwarf satellites that have been tidally heated (e.g. Jiang et al. 2019; Liao et al. 2019). One challenge with comparing MW analog satellite UDGs to other dwarf galaxy populations is that there are very few confirmed satellite UDGs in the literature (e.g., Román & Trujillo 2017; Cohen et al. 2018; Mao et al. 2021; Carlsten et al. 2022; Nashimoto et al. 2022; Karunakaran & Zaritsky 2023).

There have been recent studies of similar diffuse dwarf galaxies, referred to as ultra-puffy galaxies (UPGs), that have selected on the basis of their displacement from the size-mass relation rather than by more observationally-motivated criteria (Li et al. 2022, 2023). These studies have aimed contribute to the known sample of size-mass outlier dwarf galaxies existing as satellites of larger galaxies and to characterize their properties. Here, using longslit spectroscopy with the Southern African Large Telescope (SALT), we confirm a subset of the galaxies presented in Li et al. (2022) as UPG satellites of MW-like analogs. This is ongoing work that will be completed in the months following the submission of this thesis.

The layout of this paper is as follows. Section 4.2 describes the data presented in this work, including how the sample was selected (§4.2.1), SALT observations (§4.2.2), and data reduction (§4.2.3). In Section 4.3, we measure redshifts for UPG candidates that show obvious Hα emission. We then verify the effictiveness of the Li et al. (2022) selection criteria in Section 4.4 by comparing our measured redshifts to those of the matched analog galaxies. Lastly, in Section 4.5, we summarize our preliminary findings and detail the future work that will be done before we submit this to a journal.

4.2 Data

Outliers from the galaxy size-mass relation present astronomers with a unique opportunity to better constrain the processes that influence how a galaxy forms. However, an ongoing challenge for studying LSBGs is that their faintness makes them difficult to detect in large surveys. However, progress has been made in recent years to identify LSBG candidates in surveys designed to detect distant, faint galaxies (e.g. Greco et al. 2018). In this section, we describe the LSBG detection pipeline developed by Greco et al. (2018) as well as how size-mass outliers are identified within the total parent sample in Li et al. (2022). We also detail the observations conducted for our sample of UPGs in addition to how those data were reduced.

4.2.1 Sample Selection

The galaxies analyzed in this paper are a subset of the larger sample of UPGs presented in Li et al. (2022). This sample of UPGs was initially targeted in the second data release (DR2) of the Hyper Suprime-Cam Subaru Strategic Program (HSC-SSP; Aihara et al. 2018), an optical imaging survey utilizing the Hyper-Spurime-Camera (Miyazaki et al. 2012, 2018) on the 8.2-m Subaru telescope.

The first step in constructing a sample of UPGs is to first identify LSBGs within the survey data. The main data reduction pipeline for the HSC-SSP is optimized to identify faint, small galaxies as would be found in the distant Universe. This introduces challenges for identifying physically large, diffuse objects, as the pipeline wants to "shred" them into multiple objects. Greco et al. (2018) developed a custom pipeline for identifying LSBGs within the HSC-SSP, which has been used to identify the parent sample for these UPGs. More detailed descriptions of this pipeline are given in Greco et al. (2018); Li et al. (2022), but we also briefly summarize these steps here:

1. **Remove diffuse light around bright sources:** Bright objects such as massive elliptical galaxies have surface brightness profiles whose outskirts can mimic the diffuse light emitted by LSBGs. This is mitigated by initializing several runs with SourceExtractor (Bertin & Arnouts 1996) to detect high and low surface brightness objects separately. After several runs and after detecting low surface brightness pixels at various thresholds, masks are constructed to eliminate shredded outskirts of extended bright objects (e.g., Rix et al. 2004; Barden et al. 2012; Prescott et al. 2012)
2. **Source extraction:** The images produced from the prior step are smoothed with a large Gaussian kernel, and sources of ≥ 100 connected pixels are extracted using SourceExtractor. A size cut of $r_{1/2} > 2.5$" and empirically motivated color cuts are applied. The surviving sample still contains shredded galaxy outskirts, so a deblending step in which point like sources blended with diffuse light from background objects are removed using Scarlet (Melchior et al. 2018).
3. **Modeling:** Parametric models are fit to the remaining LSBGs to estimate physical properties such as size, photometric magnitude, and surface brightness.

4. **Visual inspection and uncertainty estimation:** All of the remaining candidate galaxies are visually inspected to remove objects that are obviously point sources blended with diffuse background light that may have been missed during the earlier deblending step. Catalog completeness is then estimated for the remaining sample by simulating mock LSBGs and recovering them using these same selection techniques (e.g. van der Burg et al. 2017; Zaritsky et al. 2021; Carlsten et al. 2022; Greene et al. 2022). This also gives survey bias and uncertainty.

The aim of Li et al. (2022) was to build a large sample of size-mass outlier satellites of Milky Way-like analogs and to measure their observed properties and abundances. They did this by matching a sample of LSBGs identified with the criteria developed in Greco et al. (2018) with galaxies in the NASA-Sloan Atlas (NSA; Blanton et al. 2005, 2011) that were classified as Milky Way analogs by stellar mass ($10.2 < M_*/M_\odot < 11.2$). The NSA catalog includes measurements of galaxy properties as derived using Sloan Digital Sky Survey (SDSS; York et al. 2000) data, as well as measured redshifts from optical spectroscopic surveys, HI surveys, and direct distance measurements. Milky Way analogs in the NSA catalog were limited to a redshift range of $0.01 < z < 0.04$, to ensure that a sufficient volume is probed to find potentially rare outliers but to exclude extremely low-z objects that are more prone to shredding.

NSA Milky Way analogs are matched to LSBGs by first computing the virial radii of these galaxies, and identifying LSBGs that fall within that as satellites. If satellites fall within the virial radii of many hosts, they are assigned to their nearest neighbors. Mass-size outliers are then selected from the full LSBG satellite sample. UPGs are selected as dwarf galaxies that fall $> 1.5\sigma$ from the Milky Way analog satellite galaxy size-mass relation (Carlsten et al. 2021). This selection gives a UPG sample of 337 galaxies associated with 239 hosts. However, it is worth noting that the matches between LSBGs and MW analogs in Li et al. (2022) are projected matches as they do not have direct distance measurements for the LSBG sample. The aim of this work is to spectroscopically confirm the distances to a subset of the UPG sample to confirm if they are actually associated with their matched Milky Way-like hosts.

4.2.2 SALT Observations

Spectroscopic observations for this subsample of UPGs were collected using the Robert Stobie Spectrograph (RSS; Smith et al. (2006) on the Southern African Large Telescope (SALT) beginning in fall 2022 and ongoing through spring 2023. We used RSS in lonsgit mode with a single, 8' long and 2" wide slit with a PG0900 grating. We set the grating angle to 15.5°and the camera angle to 31°. This gives us an observed wavelength range of $4344.8 < \lambda_{obs}/\text{Å} < 7397.2$ and spectral resolution of $R \sim 778$. Each target was observed for three exposures of ~ 750s, for a total integration time 0f 2250s. These observations are summarized in Table 4.1.

4.2.3 Spectroscopic Reduction

We reduced the spectroscopic data following the pipeline detailed in Hainline et al. (2014). The data were initially mosaiced, bias reduced, and dark subtracted using the SALT pipeline. The following reduction steps were done using PyRAF, the Python impletation of standard IRAF[1] routines (Science Software Branch at STScI 2012). We flat-fielded our science frames, and then applied a wavelength solution to our objects using a Xenon arc lamp reference spectrum. We generated bad pixel maps for each exposure to account for cosmic rays in our data. We then background subtracted and combined the three observations for each target to obtain median spectra and their uncertainties. The images were next extinction corrected using the measured airmass at the beginning of the observation. Using a 2.7" aperture centered on the continuum, we extracted the one-dimensional spectrum for

---

[1] IRAF is distributed by the National Optical Astronomy Observatory, operated by the Association of Universities for Research in Astronomy (AURA) Inc., under cooperative agreement with the National Science Foundation.

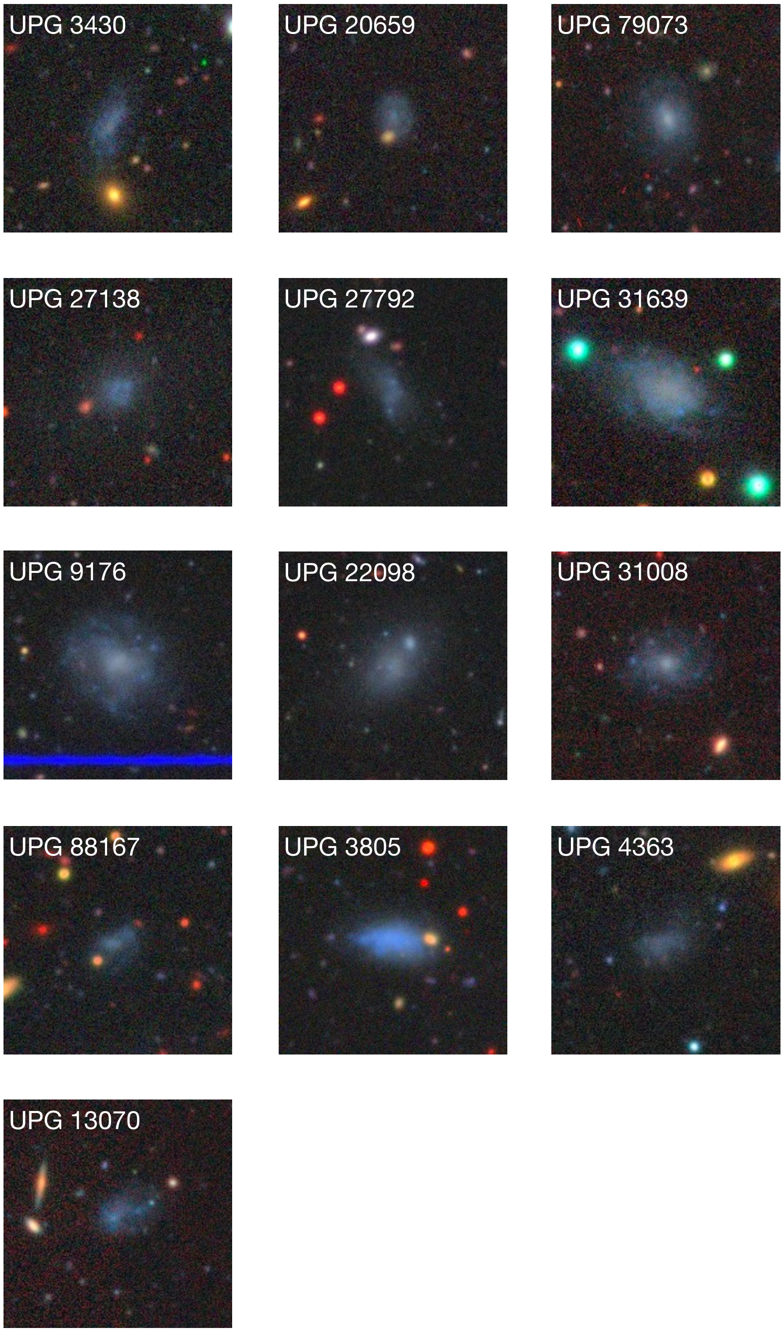

Figure 4.1 RGB Suburu HSC cutouts of the 13 UPGs presented in this work.

Table 4.1 Summary of spectroscopic observations with SALT.

Target (1)	RA (h:m:s) (2)	DEC (h:m:s) (3)	Date (UT) (4)	Exposure (sec) (5)	Airmass (6)
UPG 34340	12:25:41.18	-02:23:44.40	2023-01-28	3×750.13	1.21
UPG 20659	01:54:52.13	-02:34:41.70	2022-11-26	3×750.14	1.24
UPG 79073	00:13:23.30	+00:46:11.40	2022-11-24	3×750.14	1.28
UPG 27138	08:38:28.13	-02:02:10.00	2022-12-01	3×750.13	1.25
UPG 27792	10:13:13.13	-00:45:43.10	2023-01-21	3×750.13	1.19
UPG 31639	08:29:57.08	-01:16:26.10	2022-12-03	3×750.14	1.24
UPG 9176	10:05:31.58	+02:39:37.30	2023-01-03	3×750.13	1.23
UPG 22098	22:53:25.81	+01:24:48.90	2022-11-14	3×700.13	1.30
UPG 31008	01:13:53.97	+02:07:30.50	2022-11-23	3×750.13	1.23
UPG 88167	08:32:11.15	-01:10:18.70	2022-12-27	3×750.13	1.25
UPG 3805	10:04:27.01	+01:53:41.40	2022-12-28	3×750.13	1.28
UPG 4363	11:45:35.26	-01:51:15.60	2023-01-21	3×750.13	1.18
UPG 13070	01:23:38.15	-00:30:43.20	2022-11-25	3×750.13	1.21

each target. We lastly flux-calibrated our data using standard star spectra provided by SALT and made a correction for heliocentric velocity.

4.3 Measuring redshift

Of the 13 galaxies presented in this work, 9 had obvious Hα emission in their extracted one-dimensional spectra. The MW-like host galaxies matched with the UPGs in our sample have all been measured at low-z, so we identified the strongest feature immediately redward of rest-frame (6562.8 Å) as our observed Hα peak. We visually confirmed the presence of Hα emission by comparing our identified line to the two-dimensional spectrum to ensure that the feature was in fact Hα and not a sky line that had not been completely subtracted during the data reduction process.

For the galaxies with Hα emission, we measure line centroids by modeling the emission line as a Guassian distribution using the estimate_line_parameters function in SPECUTILS (Astropy-Specutils Development Team 2019). These spectra and the Gaussian fits to their

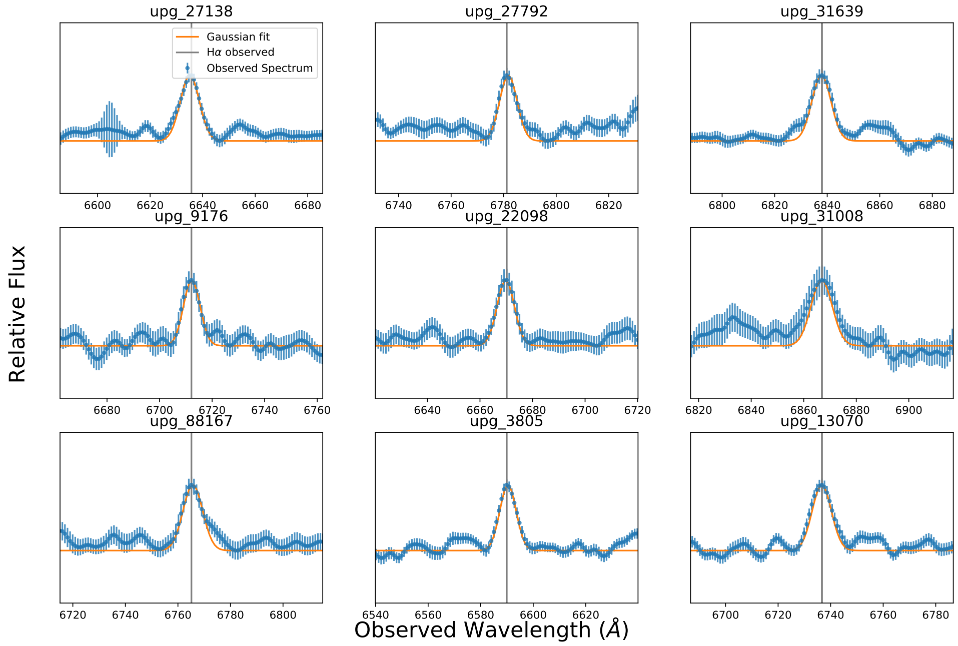

Figure 4.2 Measuring Hα line parameters for the targets with detected emission. The blue points and their error bars are the observed SALT spectra for each source, and the orange curve is the best-fit Gaussian model for the Hα emission line. The grey, vertical line denotes the location of the observed line centroid for each source.

Table 4.2 Measured redshifts and uncertainties for UPGs with detected Hα.

Target (1)	z_{meas} (2)	σ_z (3)
UPG 3805	0.004045	0.0000768
UPG 27138	0.011118	0.0000822
UPG 22098	0.016364	0.0001387
UPG 9176	0.022756	0.0001248
UPG 13070	0.026670	0.0001266
UPG 88167	0.030802	0.0001380
UPG 27792	0.033205	0.0056611
UPG 79073	0.038404	0.0073417
UPG 31639	0.042031	0.0001779
UPG 31008	0.046290	0.0017823

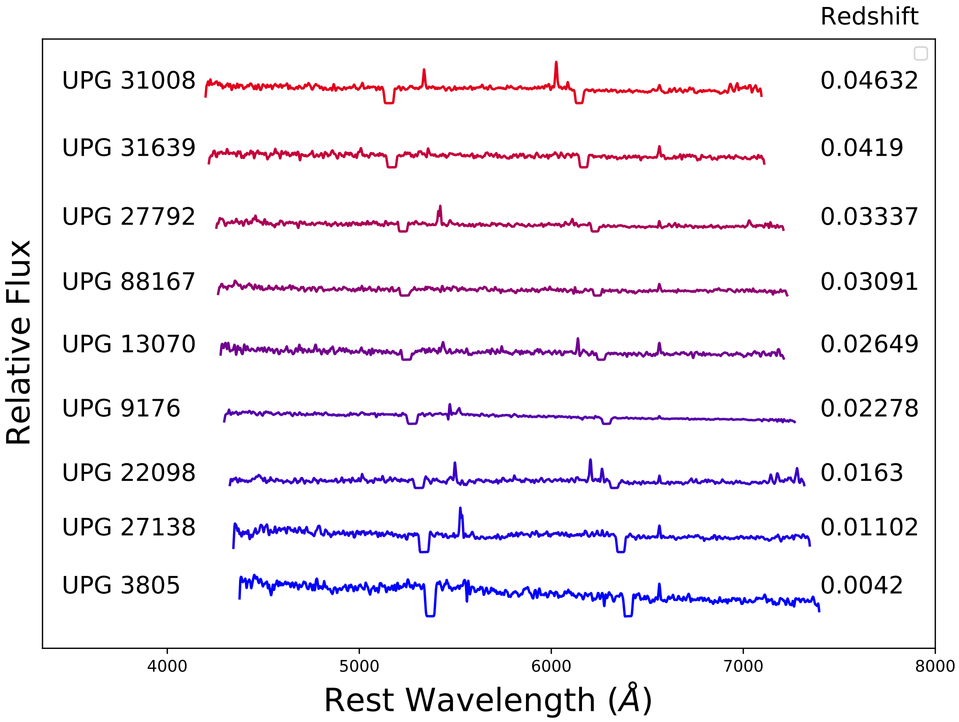

Figure 4.3 Rest frame spectra for the galaxies in our sample that had obvious Hα emission (highlighted grey region). Redshifts for the galaxies presented here range from $0.00405 < z < 0.0412$.

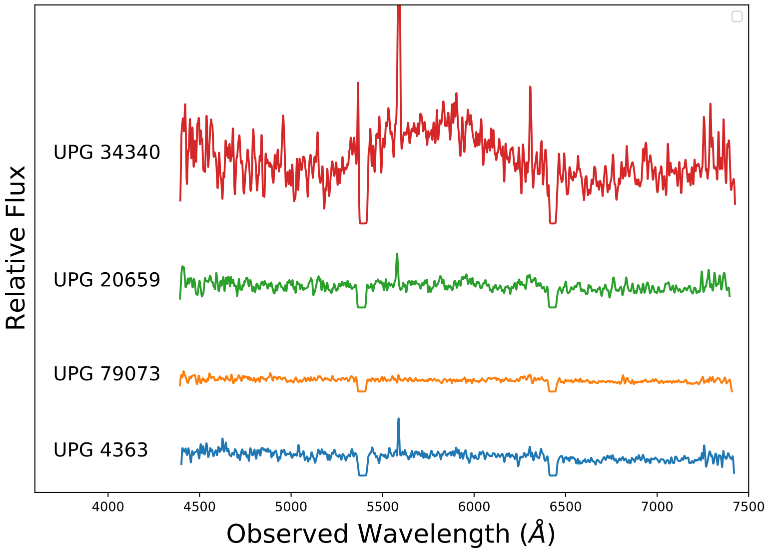

Figure 4.4 Observed frame spectra for the galaxies in our sample that lack obvious Hα emission.

Hα emission can be seen in Figure 4.2. We calculate the uncertainty on our measured redshift via bootsrapping. For each target, we randomly generate a 1000 spectra from within the uncertainty limits of the observed spectrum to construct a distribution of redshifts, the standard deviation of which is adopted as the uncertainty on the measured redshift. These values are given in Table 4.2 and the rest-frame spectra of our Hα detected UPG galaxies are shown in Figure 4.3. For completeness, we also show observed frame spectra for the galaxies in our sample that lack strong emission features in Figure 4.4.

4.4 Verifying Satellite Identification

It is common practice for distances to LSBGs to be measured by matching them to more massive host galaxies based on projected distances (e.g., van Dokkum et al. 2015a; van der Burg et al. 2016; Zaritsky et al. 2022; Nashimoto et al. 2022; Li et al. 2022). However, relatively few of these matched pairs are later spectroscopically confirmed, so these samples could contaminated by objects that are not physically associated with their matched hosts.

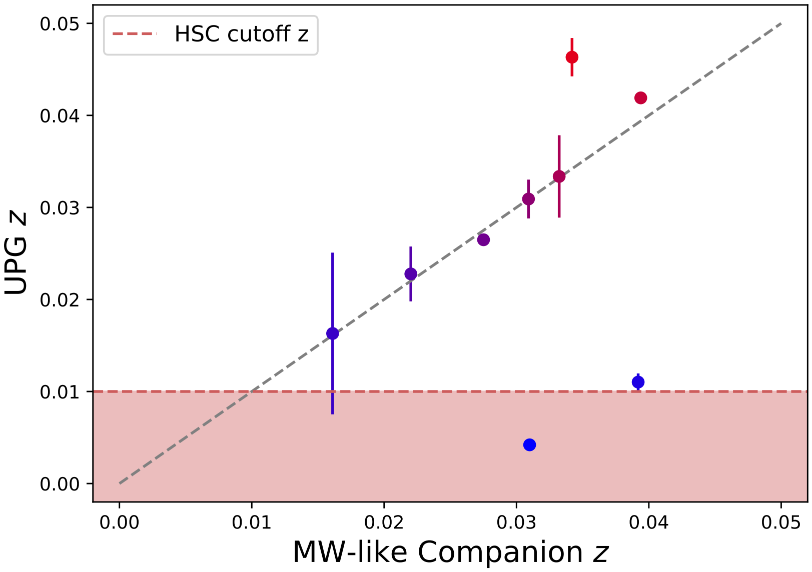

Figure 4.5 A comparison of the spectroscopically measured redshifts for the galaxies in our sample with Hα emission with those of their matched Milky Way hosts. The points are colored to match the color scheme in Figure 4.3. The errors on our redshift measurements have been estimated from bootstrapping. The grey, dashed line shows the one-to-one relation between host and UPG redshift. The red, shaded region highlights the part of parameter space that would excluded using the criteria of Greco et al. (2018). There is generally good agreement between our measured UPG redshifts and that of their host galaxies, suggesting this is an effective matching criteria.

The primary aim of this work is to spectroscopically confirm redshifts for a subset of UPGs presented in Li et al. (2022). In addition to confirming whether or not candidate LSBGs are true satellites, this will also help place constraints on the effectiveness of LSBG target selection and host matching in future surveys.

We show a comparison between the redshifts measured for the 9 galaxies with Hα emission and that of their matched Milky Way-like hosts in Figure 4.5. The grey, dashed line gives the one-to-one relationship between messured UPG redshift and that of its matched MW analog host. We also show the low redshift exlusion region (red shaded) that Li et al. (2022) used to avoid nearby objects that were more likely to be shredded. Overall, we find good agreement between the measured redshifts for our UPG sample and those of their matched hosts. Of the nine galaxies with Hα emission, only three UPGs were major outliers from the one-to-one relation. Of those outliers, two had SALT-measured spectra that approached the redshift cut used by Li et al. (2022), strongly suggesting that these matches are not associated with their hosts. The other outlier is UPG 31008, a galaxy that shows two strong emission features in close proximity to one another. The redshift presented here is for the stronger, more red feature. However, there would be better agreement with its matched host if we select the weaker feature. To reiterate, this is ongoing work and I plan to explore how varying the techniques I use to select spectral features changes our results in the coming months. Although this is a small sample of galaxies being presented, this work suggests that the MW analog-UPG candidate matching criteria used in Li et al. (2022) is effective at selecting true satellite galaxies and has relatively few projected match contaminants. This work would benefit by including more targets that have spectroscopic redshift measurements.

4.5 Summary & Future Directions

In general, dwarf galaxy populations are important astronomical objects for testing various theories on dark matter and galaxy formation. However, until recently it has been very difficult to observationally account for the faintest populations of dwarf galaxies, such as LSBGs and the even more extreme size-mass outliers within the LSBG population including UDGs and UPGs. Characterizing the properties of populations of UDGs and UPGs across different environments can help place constraints on the processes that are most responsible for regulating star formation in low-mass galaxies, allowing simulations to better reproduce observed galaxy mass and luminosity functions.

Most of what is known about dwarf galaxy populations comes from observations of Milky Way and Local Group satellite galaxies, meaning that we need to characterize size-mass outlier galaxies that are satellites around MW analogs to understand how they fit in compared to the larger known dwarf galaxy population. There has been significant work in recent years to match LSBG candidate galaxies to MW analogs, but this is normally done in projected space meaning that there is a chance that contaminant galaxies not physically associated with MW-like host could be selected.

In this work, we focus on a subset of thirteen UPG candidates that were selected as MW analog satellites in Li et al. (2022). We conduct long-slit spectroscopic observations using SALT to measure redshifts for this sample, allowing us to not only confirm these targets as UPGs, but to assess the effectiveness of the satellite-MW analog matching described in Li et al. (2022). We found that nine of the thirteen SALT-observed UPG candidates contained obvious Hα emission in their spectra. The Hα detected galaxies had redshifts in the range $0.0042 < z < 0.046$, and all but three showed good agreement with the measured redshifts of their associated MW-like host galaxies. Two of the outlier galaxies are sources that should not have been included in the sample based on redshift cuts implemented in Greco et al. (2018), and they are clearly targets that are not actually physically associated with their matched hosts. It is possible that the other outlier, UPG 31008, is not actually an outlier and that we have measured the redshift of the incorrect line as there are two prominent features close to one another and we simply seleted the higher signal-to-noise line. This is something that will be explored in the near future.

We note that this is ongoing work and that the results being presented here are preliminary. There are still rich analyses to be done with this data set to better understand this unique population of size-mass outliers. First, this is an incomplete sample. The targets presented here are just a fraction of those for which we have proposed SALT observations. These observations will be ongoing throughout spring 2023, and new targets will be reduced and analyzed as they are taken. We also plan to propose SALT observations for additional targets in upcoming calls for proposals.

Another future aim for this work is to measure a luminosity function for these MW analog satellite UPGs. Since we have measured redshifts for this sample, we can calculate Hubble-flow corrected distances (e.g. Mould et al. 2000) and luminosities. This will help give constraints on the slope of the low-lumimosity end of the local galaxy luminosity function, giving simulations more refined observables to reproduce. The last aim of this work is to put MW-analog satellite UPGs into context with UDGs in the field. We also have a set of unpublished SALT observations for a sample of nearby field UDGs selected from those presented in Greco et al. (2018). A goal here would be to similarly measure a luminosity function for these field UDGs and compare that with what we find for UPGs residing in the halos of massive MW-like hosts.

These field UDGs are also interesting in and of themselves, since they are likely not as strongly effected by environmental quenching and can be victims of less widely studied mechanisms like coupling to the angular momentum for high-spin dark matter halos or weak stellar feedback. It would also be interesting to match our field UDGs with radio survey catalogs to determine if they are inefficiently forming stars because they do not have gas, or if they are HI-bearing ultra diffuse galaxies (e.g., Leisman et al. 2017) that are being impacted by weak, nonejective stellar feedback or coupling to high-spin dark matter halos.

Chapter 5

Summary & Future Work

The work presented in this dissertation aims to address fundamental questions regarding the processes that regulate galaxy and supermassive black hole formation and evolution. I have taken several approaches in doing this which range from developing physically motivated, semi-empirical models for statistically large populations of galaxies and active black holes to reducing and analyzing observational data to contribute to known samples of rare galaxies. In this chapter, I will summarize results presented in this thesis and I will highlight outstanding questions and future work that can be done to help answer them.

5.1 Conclusions

There are many factors that can contribute to which processes are most responsible for shaping the populations of galaxies and supermassive black holes we observe in the Universe. In Chapter 1, I introduce that supermassive black holes in the centers of galaxies can feed on nearby accretion disks of material, making them extremely luminous active galactic nuclei (AGN). AGN are believed to consist of several components aside from the black hole and accretion disk, including narrow and broad-line emitting gas and a parsec scale optically and geometrically thick dusty torus. Optical observations show that not all AGN exhibit broad emission features. However polarimetric measurements are able to recover the broad lines, suggesting that there is obscuring material along the line-of-sight to an observer. The nature of this obscuring material is largely uncertain. It is possible that obscuration in AGN is a random orientation in which certain lines-of-sight are obscured by the dusty torus. An implication of this scenario is that large populations of AGN should show no bulk differences in their observed properties. It is also possible that obscuration is an evolutionary phase that an AGN will experience in its lifetime caused by galaxy-scale dust lanes created in gas-rich major mergers. This scenario is supported by clustering measurements of large populations of obscured and unobscured AGN that suggest that obscured AGN reside in more massive dark matter halos.

The work presented in Chapter 2 aims to address the nature of obscuration in a highly luminious population of AGN known as quasars. In this work, I consider scenarios in which the degree of torus obscuration is tied to other physical properties such as the quasar's accretion rate. This model is physically motivated by X-ray studies of nearby, less luminous AGN that show that an AGN's covering fraction inversely scales with accretion rate, suggesting that radiation can regulate the shape of the dusty torus on short timescales typical of black hole accretion. I implement this in physically motivated, semi-empirical models for statistical populations of $z \sim 1$ infrared-selected quasars to determine if radiation regulated unification or galacy-scale can alleviate the discrepancy between clustering measurements and unified torus obscuration model predictions. I find that the physically motivated models I construct are incapable in reproducing clustering measurements, suggesting that obscuration likely varies on timescales typical of galaxy evolution.

Another central theme of this dissertation aims to answer the question: ”How does stellar feedback shape populations of galaxies experiencing extreme star formation?” This is explored in some of the most rapidly star forming galaxies in Chapter 3 and in faintest, most diffuse galaxies in Chapter 4. An open area of research seeks to determine how massive galaxies form and quench throughout cosmic time. Large-scale cosmological galaxy formation simulations suggest that feedback is a necessary ingredient for removing gas from galaxies, thus quenching star formation. Typically, it is believed that feedback from AGN plays a larger role in quenching massive galaxies.

In this work, I study a population of $z \sim 0.5$ extremely compact, massive starburst galaxies to determine if stellar feedback can drive the types of large-scale, high-velocity, ejective outflows required for quenching massive galaxies. This population of galaxies is important; they are local analogs of the compact star forming galaxies more common at $z \sim 2$ and they host high-velocity outflows and show only limited signs of ongoing AGN activity, which make them the perfect laboratories to test the limits of extreme stellar feedback. In Chapter 3, I construct physical models for the stellar populations observed in this sample of compact starbursts. I fit their observed spectral energy distributions to constrain posterior distributions for the parameters in my model to simulate a statistical mock population of galaxies. I evolve the model galaxies and run our selection function to determine observability timescales and an intrinsic space density for this extreme population of compact starburst galaxies. I then place these galaxies in the context of merger driven galaxy evolution scenarios in which gas-rich mergers trigger extreme nuclear star formation and AGN activity before feedback quenches the galaxy. I find that the galaxies in this sample are possible local analogs for the compact star forming galaxies observed in the early Universe, and that feedback from extreme nuclear star formation might be responsible for quenching the most extremely star forming and massive ULIRGs and forming a fraction of massive post starburst galaxies at intermediate-z.

On much smaller scales, this thesis also explores how stellar feedback can potentially regulate star formation in extreme dwarf galaxy populations. Ultra-diffuse and ultra-puffy galaxies (UDG and UPG, respectively) are dwarf size-mass relation outliers. They have optical effective radii that can extend to ~1-10 kpc scales, but with stellar masses that classify them as dwarfs. Much recent work has focused on placing constraints on the processes that either “puffed up” these dwarf galaxies or rapidly quenched star formation early on in what would otherwise be Milky Way like galaxies. In Chapter 4, I present spectra taken on the Southern African Large Telescope (SALT) for a sample of UPGs that have been identified as satellites of Milky Way like galaxies. For the thirteen galaxies presented here, nine have obvious Hα emission from which redshifts can be measured. This is ongoing work, but I present preliminary results that show that UPG candidate-Milky Way analog matching procedures that use projected angular distances are overall effective at constructing populations of UPG satellite candidates.

5.2 Future Work

This is an incredibly exciting time to studying the processes that shape galaxy formation and evolution. We are in an age when new observational frontiers are being pushed in part due to *JWST*, the Vera Rubin Observatory’s Legacy Survey for Space and Time (LSST), and the Dark Energy Survey (DES). These facilities will allow us to peer early into the Universe to observe the first galaxies being formed. Technological advances have also led to improved simulations such as the recent release of the MillenniumTNG simulation (Pakmor et al. 2022), a composite simulation that combines the hydrodynamic galaxy formation models of IllustrisTNG (Vogelsberger et al. 2014) with the large-scale dark matter-only Millennium simulation to characterize galaxy formation in the context of large-scale structure formation (Springel et al. 2005b).

I am primarily interested in continuing to explore the role of feedback in shaping observed galaxy populations. This includes using new tools to characterize the compact starbursts and UDGs I have been studying, but also trying to constrain the relative roles of AGN versus stellar feedback by studying a local population of star forming Seyfert galaxies. I will briefly summarize each of these possible directions here.

5.2.1 Compact star formation in cosmological simulations

I am interested in determining what types of galaxy mergers most frequently produce galaxies like the ones in our sample, as well as if the strong stellar feedback we observe is capable of completely quenching massive galaxies. Cosmological simulations currently provide the best test space to explore the effects of galaxy formation mechanisms. I plan to use radiative-transfer models such as SKIRT (Camps & Baes 2015) to simulate photometric and spectroscopic data for galaxies in the intermediate-sized (100^3 Mpc^3) TNG100 and large-volume (300^3 Mpc^3) TNG300 simulations. This will allow me to select simulated galaxies that have observed properties that are representative of those studied in Chapter 3. I choose TNG100 because although we only expect a handful of our sources in each redshift interval, its higher resolution means that it will be able to resolve the nuclear burst and potential outflows, thus creating galaxies more representative of our sample (e.g., Patton et al. 2020; Zinger et al. 2020; Quai et al. 2021). I also want to study the evolution of gas-rich mergers, as they are the likely progenitors to our galaxies, and the large simulation volume of TNG300 would be conducive doing so on a population level. I will use our observational targeting criteria to select mock galaxies from the simulation volume to characterize their evolution to determine the importance of extreme stellar feedback in massive galaxy evolution .

I also am interested in whether past AGN activiy could have plated a role in forming the compact starburst galaxies presented in Chapter 3. Simulations have shown that galaxy mergers are effective at driving cold gas to the central regions of galaxies, thus producing both rapid nuclear star formation and active galactic nucleus (AGN) accretion. AGN and powerful, nuclear starburst often coexist in the central regions of galaxies, but it is unclear if this is because they are fueled by the same processes or if there is a more intimate physical connection between them through which they are able to influence each other's evolution through feedback (e.g., Zhuang & Ho 2020). The compact starburst galaxies in our observed sample are unique in the fact that they are undergoing extreme amounts of nuclear star formation, host powerful outflows, but have no evidence of coexisting with AGN. This raises two questions, the answers to which will provide important clues to the formation of massive galaxies: (1) Is it possible that these outflows were driven by past AGN activity and that nuclear star formation is observable for longer timescales? (2) Are compact nuclear starbursts creating the environment necessary for inducing AGN accretion?

As for the first question, AGN variability can occur on 10^4 yr timescales while nuclear star formation can last on 100 Myr timescales (e.g., Hickox et al. 2014; Diamond-Stanic et al. 2021). Physical models have also suggested that outflows in starburst galaxies without obvious AGN signatures could be consistent with feedback from heavily obscured AGN whose accretion varies on short timescales (e.g. Ishibashi & Fabian 2022). Within the limits of our current observations, our sample of compact starbursts represent stellar feedback at its most extreme. If it could be more conclusively determined that they have not had prior episodes of AGN accretion within a timescale that could produce their outflows, that would suggest that stellar feedback is a necessary process in the quenching of massive galaxies. To answer this, I would follow a similar procedure of modeling the observed spectra and photometry for simulated galaxies in the TNG100 simulation and selecting compact starburst galaxies. I will track the co-evolution of the stellar population and central SMBH, as well that of the galaxy's gas kinematics. I will use physically-motivated models of outflow kinematics from SMBH accretion properties at each time step to verify if the energetics of prior AGN activity are consistent with driving the outflows seen in observations (e.g. Ishibashi & Fabian 2022).

Nuclear starbursts could be an evolutionary phase for galaxies that precedes AGN accretion. The processes by which gas is brought to within the sphere of influence of central SMBHs are poorly understood, and it is possible that feedback from nuclear star formation could help drive gas towards the most central regions of the galaxy. To address this question I plan to use the small-volume (50^3 Mpc^3) TNG50 simulation (Nelson et al. 2019), as its resolution is comparable to that of zoom-in galaxy simulations making it ideal for studying gas kinematics in galaxies. Compact, starburst galaxies are orders of magnitude more common in the early Universe (e.g., Barro et al. 2013), so I plan to select these high-z counterparts to explore how compact star formation might foster AGN activity. I will also select a mass-matched sample of quiescent compact galaxies, and post mergers and track their evolution to measure AGN fractions at different epochs and to compare the innermost gas kinematics between these populations, giving insight as to if compact starbursts contribute significantly to AGN accretion.

5.2.2 Multiwavelength studies of HI-bearing UDGs

In Chapter 4, I introduced HI-bearing ultra-diffuse galaxies (HUDs; Leisman et al. 2017), UDGs with neutral gas reservoirs more typical for galaxies of their size rather than their stellar mass. HUDs galaxies cannot be explained by the most extreme outflow scenarios that completely expel gas from the host galaxy since they contain massive neutral hydrogen gas reservoirs.

They are also interesting because they directly challenge our understanding of the Kennicutt-Schimidt law of star formation that has empirically shown that the surface density of gas in a galaxy is related to the surface density of its star formation rate (e.g. Schmidt 1959; Kennicutt 1998). HUDs can host atomic gas reservoirs of $\sim 10^9\ M_\odot$ that are spread out over a region having a radius of several kpc. This would imply that they would be well-described by the Kennicutt-Schmidt law as their gas surface densities are well within the range fit by Kennicutt (1998). Early evidence shows that LSBGs obey the Kennicutt-Schmidt relation well McGaugh et al. (2017), but we note that these are not normalized for the surface density for the star formation or the gas, making it difficult to confidently conclude that LSBGs will obey this relation. Obtaining spatially-resolved gas masses and star formation rates could allow us to determine if HUDs whose gas masses are on the order of a gas-rich

L_* galaxy obey the local surface density relation even though their stellar populations are under-massive and diffuse.

In the case of HUDs, it is not well understood why stars are not forming out of their massive neutral hydrogen reservoirs. However, it is worth noting that HI might not be the best tracer of star formation in galaxies as stars do not directly collapse from clouds of neutral hydrogen. Rather, they form out of clouds of cold, dense molecular gas. A reason for suppressed star formation in gas rich HUDs could be that the neutral hydrogen is not able to efficiently condense into molecular clouds. Much recent work has been done to try to constrain the formation mechanisms of HUDs, and two prevailing scenarios have emerged. The first is that high dark matter halo spin parameters prevent these galaxies from being more condensed (e.g. Jones et al. 2018; Amorisco & Loeb 2016; Rong et al. 2017). With respect to the neutral hydrogen in HUDs, this means that the gas gets too dispersed to undergo gravitational collapse. The other well-supported star formation suppression mechanism is that stellar feedback disperses the matter in the galaxy, making the gas too diffuse to collapse (e.g., Di Cintio et al. 2017). Obtaining spatially-resolved submillimeter observations at a facillity like ALMA could allow us to determine if their molecular gas is turbulent due to stellar winds, thus placing constraints on stellar feedback's role in star formation suppression.

5.2.3 Spatially-Resolved Outflow Kinematics in Nearby Seyfert Galaxies to Probe Stellar Feedback

In order for feedback to quench massive galaxies, the feedback source needs to be able to drive powerful, large-scale outflows with velocities comparable to or greater than the escape velocity for the system (e.g., Veilleux et al. 2020). This means that star formation-driven outflows responsible for quenching massive galaxies need to be generated by extremely powerful and often compact starbursts; this is supported by evidence that outflow velocity scales with star formation rate (SFR) and morphological compactness (e.g., Heckman et al. 2015; Petter et al. 2020). Cosmological galaxy formation simulations also show that large-scale outflows with are necessary to reproduce galaxies with masses that are consistent with local observations (e.g., Veilleux et al. 2005, 2020). One challenge with measuring the kinematics of large-scale stellar feedback-driven outflows is that galaxies that are most likely to have rapid and compact enough star formation to launch super-galactic winds are most commonly found at $z > 1.5$ (e.g., Barro et al. 2013; van Dokkum et al. 2015b). This large distance makes it difficult to spatially resolve any kpc-scale outflows in these systems.

Chapter 3 demonstrates that systematically targeting galaxies with spatially-resolved, powerful, large-scale, outflows that are primarily launched by stellar feedback is difficult. Although powerful ejective feedback is necessary to quench massive galaxies, it could be possible to use smaller-scale feedback as a proxy to understand how ISM kinematics are affected by local star formation. It has been shown that the Kennicutt-Schmidt relation, a global star formation law where star formation rate density scales with gas density, can hold for spatially resolved star forming regions in the disks of local galaxies (e.g., Shi et al. 2018). This suggests that the same underlying physics that governs how stars and the ISM interact with each other on global scales could also apply in local star forming regions. This could provide a new avenue of measuring ISM kinematics in the vicinity of local star forming regions to constrain the relative importance of stellar feedback in disrupting gas and regulating star formation on global scales.

It could be possible to to identify clumps of star formation in local star forming Seyferts using spatially resolved infrared and UV observations and calculate their local SFRs, and to then measure spatially-resolved gas kinematics in these regions using integral field unit (IFU) observations to constrain how star formation affects its local gas environment. Based on recent evidence that global star formation laws apply on local scales, any findings here could be extrapolated to apply to how stellar feedback affects quenching on galaxy scales.

The benefit of using nearby star forming Seyfert galaxies is that these targets are spatially resolved in IR images, and that star forming regions farther out in the disk can be analyzed separately from the nuclear regions. This will allow me to measure the ISM kinematics near purely star forming regions, as well as providing a comparison sample to determine how the ISM properties differ between star forming clumps in the disk and the nuclear regions most affected by the central AGN.

Once a subsample of targets with IR/far-ultraviolet (FUV) images is constructed, I will be able to identify and characterize individual star forming regions within their stellar disks. This multi-wavelength approach of quantifying star formation allows for both obscured and unobscured star formation to be traced to be used to construct SFR density maps. This sample can be crossmatched with galaxies that have optical integral field unit (IFU) observations in the Mapping Nearby Galaxies at APO (MaNGA; Bundy et al. 2015) survey. Using optical emission line diagnostics, these IFU observations will allow me to construct spatially-resolved maps of the ionization state of the ISM, to discern which regions of the galaxy are being ionized by newly formed stars, AGN activity, or both to determine how gas kinematics change depending on feedback source (e.g., Kewley et al. 2006; Juneau et al. 2011).

I will be able to measure low-ionization emission lines at each resolution element, such as [OII], to calculate their velocities from line profiles as well as be able to construct velocity maps for the various detected spectral features. I can then compare the SFR density maps, line velocities, and the spatially-resolved ionization and cold gas states with one another to constrain how gas kinematics vary with star formation rate and ionization source. These can then be compared the observed and simulated relationships between global star formation rate and outflow velocity to confirm the validity of using local star forming clumps as proxies for massive, compact nuclear starbursts.

The fact that there will be some regions in these sample galaxies that are ionized by star formation and others by the AGN will provide unique constraints on how much star formation is required for outflows to be mostly driven by stellar feedback in galaxies that are hosting low-luminosity AGN. Until we are able to consistently and systematically observe outflows in distant, compact star forming galaxies, understanding the role stellar feedback plays in impacting gas kinematics on local scales will be able to provide the most statistically robust insight as to whether stellar feedback can be a primary driver of galaxy-wide quenching.

Bibliography

Abraham, R. G., Valdes, F., Yee, H. K. C., & van den Bergh, S. 1994, ApJ, 432, 75, doi: 10.1086/174550

Abraham, R. G., van den Bergh, S., & Nair, P. 2003, ApJ, 588, 218, doi: 10.1086/373919

Adams, N. J., Bowler, R. A. A., Jarvis, M. J., Häußler, B., & Lagos, C. D. P. 2021, MNRAS, 506, 4933, doi: 10.1093/mnras/stab1956

Adelman-McCarthy, J. K., Agüeros, M. A., Allam, S. S., et al. 2006, ApJS, 162, 38, doi: 10.1086/497917

Aihara, H., Allende Prieto, C., An, D., et al. 2011, ApJS, 193, 29, doi: 10.1088/0067-0049/193/2/29

Aihara, H., Arimoto, N., Armstrong, R., et al. 2018, PASJ, 70, S4, doi: 10.1093/pasj/psx066

Alexander, D. M., & Hickox, R. C. 2012, New Astronomy Reviews, 56, 93, doi: 10.1016/j.newar.2011.11.003

Alexander, D. M., Brandt, W. N., Smail, I., et al. 2008, AJ, 135, 1968, doi: 10.1088/0004-6256/135/5/1968

Amorisco, N. C., & Loeb, A. 2016, MNRAS, 459, L51, doi: 10.1093/mnrasl/slw055

Angel, J. R. P., Hilliard, R. L., & Weymann, R. J. 1979, in The MMT and the Future of Ground-Based Astronomy, Vol. 385, 87

Antonucci, R. 1993, Annual Review of Astronomy and Astrophysics, 31, 473, doi: 10.1146/annurev.aa.31.090193.002353

Antonucci, R. R. J., & Miller, J. S. 1985, ApJ, 297, 621, doi: 10.1086/163559

Assef, R. J., Stern, D., Kochanek, C. S., et al. 2013, ApJ, 772, 26, doi: 10.1088/0004-637X/772/1/26

Astropy-Specutils Development Team. 2019, Specutils: Spectroscopic analysis and reduction, Astrophysics Source Code Library, record ascl:1902.012. http://ascl.net/1902.012

Baldry, I. K., Glazebrook, K., Brinkmann, J., et al. 2004, ApJ, 600, 681, doi: 10.1086/380092

Baldwin, J. A. 1977, ApJ, 214, 679, doi: 10.1086/155294

Balogh, M. L., Morris, S. L., Yee, H. K. C., Carlberg, R. G., & Ellingson, E. 1999, ApJ, 527, 54, doi: 10.1086/308056

Barden, M., Häußler, B., Peng, C. Y., McIntosh, D. H., & Guo, Y. 2012, MNRAS, 422, 449, doi: 10.1111/j.1365-2966.2012.20619.x

Barro, G., Faber, S. M., Pérez-González, P. G., et al. 2013, ApJ, 765, 104, doi: 10.1088/0004-637X/765/2/104

Barthelmy, S. D., Barbier, L. M., Cummings, J. R., et al. 2005, SSRv, 120, 143, doi: 10.1007/s11214-005-5096-3

Baumgartner, W. H., Tueller, J., Markwardt, C. B., et al. 2013, The Astrophysical Journal Supplement Series, 207, 19, doi: 10.1088/0067-0049/207/2/19

Baushev, A. N. 2018, New Astronomy, 60, 69, doi: 10.1016/j.newast.2017.10.008

Behroozi, P., Wechsler, R. H., Hearin, A. P., & Conroy, C. 2019, MNRAS, 488, 3143, doi: 10.1093/mnras/stz1182

Behroozi, P. S., Conroy, C., & Wechsler, R. H. 2010, ApJ, 717, 379, doi: 10.1088/0004-637X/717/1/379

Bekki, K. 2001, ApJ, 546, 189, doi: 10.1086/318231

Benavides, J. A., Sales, L. V., Abadi, M. G., et al. 2021, Nature Astronomy, 5, 1255, doi: 10.1038/s41550-021-01458-1

Bertin, E., & Arnouts, S. 1996, A&AS, 117, 393, doi: 10.1051/aas:1996164

Bertone, S., De Lucia, G., & Thomas, P. A. 2007, MNRAS, 379, 1143, doi: 10.1111/j.1365-2966.2007.11997.x

Best, P. N., Ker, L. M., Simpson, C., Rigby, E. E., & Sabater, J. 2014, MNRAS, 445, 955, doi: 10.1093/mnras/stu1776

Blanton, M. R., Kazin, E., Muna, D., Weaver, B. A., & Price-Whelan, A. 2011, AJ, 142, 31, doi: 10.1088/0004-6256/142/1/31

Blanton, M. R., Lupton, R. H., Schlegel, D. J., et al. 2005, ApJ, 631, 208, doi: 10.1086/431416

Blanton, M. R., Hogg, D. W., Bahcall, N. A., et al. 2003, ApJ, 594, 186, doi: 10.1086/375528

Blecha, L., Snyder, G. F., Satyapal, S., & Ellison, S. L. 2018, MNRAS, 478, 3056, doi: 10.1093/mnras/sty1274

Blitz, L., & Shu, F. H. 1980, ApJ, 238, 148, doi: 10.1086/157968

Bluck, A. F. L., Conselice, C. J., Bouwens, R. J., et al. 2009, MNRAS, 394, L51, doi: 10.1111/j.1745-3933.2008.00608.x

Brinchmann, J., Charlot, S., White, S. D. M., et al. 2004, MNRAS, 351, 1151, doi: 10.1111/j.1365-2966.2004.07881.x

Buchner, J., & Bauer, F. E. 2017, MNRAS, 465, 4348, doi: 10.1093/mnras/stw2955

Buchner, J., Schulze, S., & Bauer, F. E. 2017, MNRAS, 464, 4545, doi: 10.1093/mnras/stw2423

Bullock, J. S., & Boylan-Kolchin, M. 2017, ARA&A, 55, 343, doi: 10.1146/annurev-astro-091916-055313

Bundy, K., Bershady, M. A., Law, D. R., et al. 2015, ApJ, 798, 7, doi: 10.1088/0004-637X/798/1/7

Burtscher, L., Davies, R. I., Graciá-Carpio, J., et al. 2016, A&A, 586, A28, doi: 10.1051/0004-6361/201527575

Byler, N., Dalcanton, J. J., Conroy, C., & Johnson, B. D. 2017, ApJ, 840, 44, doi: 10.3847/1538-4357/aa6c66

Camps, P., & Baes, M. 2015, Astronomy and Computing, 9, 20, doi: 10.1016/j.ascom.2014.10.004

Carlsten, S. G., Greene, J. E., Beaton, R. L., & Greco, J. P. 2022, ApJ, 927, 44, doi: 10.3847/1538-4357/ac457e

Cattaneo, A., Faber, S. M., Binney, J., et al. 2009, Nature, 460, 213, doi: 10.1038/nature08135

Chabrier, G. 2003, PASP, 115, 763, doi: 10.1086/376392

Charlot, S., & Fall, S. M. 2000, ApJ, 539, 718, doi: 10.1086/309250

Choi, E., Naab, T., Ostriker, J. P., Johansson, P. H., & Moster, B. P. 2014, MNRAS, 442, 440, doi: 10.1093/mnras/stu874

Cohen, Y., van Dokkum, P., Danieli, S., et al. 2018, ApJ, 868, 96, doi: 10.3847/1538-4357/aae7c8

Coil, A. L., Hennawi, J. F., Newman, J. A., Cooper, M. C., & Davis, M. 2007, ApJ, 654, 115, doi: 10.1086/509099

Conroy, C., Gunn, J. E., & White, M. 2009, ApJ, 699, 486, doi: 10.1088/0004-637X/699/1/486

Conroy, C., & White, M. 2013, ApJ, 762, 70, doi: 10.1088/0004-637X/762/2/70

Conselice, C. J. 2009, MNRAS, 399, L16, doi: 10.1111/j.1745-3933.2009.00708.x

Croom, S. M., Smith, R. J., Boyle, B. J., et al. 2004, MNRAS, 349, 1397, doi: 10.1111/j.1365-2966.2004.07619.x

Croom, S. M., Boyle, B. J., Shanks, T., et al. 2005, MNRAS, 356, 415, doi: 10.1111/j.1365-2966.2004.08379.x

Croton, D. J. 2006, MNRAS, 369, 1808, doi: 10.1111/j.1365-2966.2006.10429.x

da Ângela, J., Shanks, T., Croom, S. M., et al. 2008, MNRAS, 383, 565, doi: 10.1111/j.1365-2966.2007.12552.x

Daddi, E., Bournaud, F., Walter, F., et al. 2010, ApJ, 713, 686, doi: 10.1088/0004-637X/713/1/686

Dark Energy Survey Collaboration, Abbott, T., Abdalla, F. B., et al. 2016, MNRAS, 460, 1270, doi: 10.1093/mnras/stw641

Davé, R., Anglés-Alcázar, D., Narayanan, D., et al. 2019, MNRAS, 486, 2827, doi: 10.1093/mnras/stz937

Davis, M., Huchra, J., Latham, D. W., & Tonry, J. 1982, ApJ, 253, 423, doi: 10.1086/159646

Davis et al., J. in prep, ApJ

Di Cintio, A., Brook, C. B., Dutton, A. A., et al. 2017, MNRAS, 466, L1, doi: 10.1093/mnrasl/slw210

Di Matteo, T., Springel, V., & Hernquist, L. 2005, Nature, 433, 604, doi: 10.1038/nature03335

Diamond-Stanic, A. M., Moustakas, J., Tremonti, C. A., et al. 2012, ApJL, 755, L26, doi: 10.1088/2041-8205/755/2/L26

Diamond-Stanic, A. M., Moustakas, J., Sell, P. H., et al. 2021, arXiv e-prints, arXiv:2102.11287. https://arxiv.org/abs/2102.11287

DiPompeo, M. A., Hickox, R. C., Eftekharzadeh, S., & Myers, A. D. 2017a, MNRAS, 469, 4630, doi: 10.1093/mnras/stx1215

DiPompeo, M. A., Hickox, R. C., & Myers, A. D. 2016a, MNRAS, 456, 924, doi: 10.1093/mnras/stv2681

DiPompeo, M. A., Hickox, R. C., Myers, A. D., & Geach, J. E. 2017b, MNRAS, 464, 3526, doi: 10.1093/mnras/stw2589

DiPompeo, M. A., Myers, A. D., Hickox, R. C., Geach, J. E., & Hainline, K. N. 2014, MNRAS, 442, 3443, doi: 10.1093/mnras/stu1115

DiPompeo, M. A., Runnoe, J. C., Hickox, R. C., Myers, A. D., & Geach, J. E. 2016b, MNRAS, 460, 175, doi: 10.1093/mnras/stw986

Disney, M. J. 1976, Nature, 263, 573, doi: 10.1038/263573a0

Donoso, E., Yan, L., Stern, D., & Assef, R. J. 2014, ApJ, 789, 44, doi: 10.1088/0004-637X/789/1/44

Draine, B. T. 2003, ARA&A, 41, 241, doi: 10.1146/annurev.astro.41.011802.094840

Earl, N., Tollerud, E., Jones, C., et al. 2022, astropy/specutils: V1.7.0, v1.7.0, Zenodo, doi: 10.5281/zenodo.6207491

Eftekharzadeh, S., Myers, A. D., White, M., et al. 2015, MNRAS, 453, 2779, doi: 10.1093/mnras/stv1763

Fabian, A. C. 2012, ARA&A, 50, 455, doi: 10.1146/annurev-astro-081811-125521

Fan, X. 2006, NewAR, 50, 665, doi: 10.1016/j.newar.2006.06.077

Farrah, D., Afonso, J., Efstathiou, A., et al. 2003, MNRAS, 343, 585, doi: 10.1046/j.1365-8711.2003.06696.x

Farrah, D., Rowan-Robinson, M., Oliver, S., et al. 2001, MNRAS, 326, 1333, doi: 10.1111/j.1365-2966.2001.04721.x

Ferrarese, L., & Merritt, D. 2000, ApJL, 539, L9, doi: 10.1086/312838

Fitzpatrick, E. L. 1999, PASP, 111, 63, doi: 10.1086/316293

Foreman-Mackey, D., Hogg, D. W., Lang, D., & Goodman, J. 2013, PASP, 125, 306, doi: 10.1086/670067

Frank, J., King, A., & Raine, D. J. 2002, Accretion Power in Astrophysics: Third Edition

French, K. D., Yang, Y., Zabludoff, A. I., & Tremonti, C. A. 2018, ApJ, 862, 2, doi: 10.3847/1538-4357/aacb2d

Gabor, J. M., & Bournaud, F. 2014, MNRAS, 441, 1615, doi: 10.1093/mnras/stu677

Geach, J. E., Hickox, R. C., Diamond-Stanic, A. M., et al. 2013, ApJL, 767, L17, doi: 10.1088/2041-8205/767/1/L17

—. 2014, Nature, 516, 68, doi: 10.1038/nature14012

Geach, J. E., Tremonti, C., Diamond-Stanic, A. M., et al. 2018, ApJL, 864, L1, doi: 10.3847/2041-8213/aad8b6

Gehrels, N., Chincarini, G., Giommi, P., et al. 2004, ApJ, 611, 1005, doi: 10.1086/422091

Gillman, S., Tiley, A. L., Swinbank, A. M., et al. 2021, MNRAS, 500, 4229, doi: 10.1093/mnras/staa3400

Goto, H., Zaritsky, D., Karunakaran, A., Donnerstein, R., & Sand, D. J. 2023, arXiv e-prints, arXiv:2303.00774, doi: 10.48550/arXiv.2303.00774

Goulding, A. D., Alexander, D. M., Bauer, F. E., et al. 2012, ApJ, 755, 5, doi: 10.1088/0004-637X/755/1/5

Greco, J. P., Goulding, A. D., Greene, J. E., et al. 2018, ApJ, 866, 112, doi: 10.3847/1538-4357/aae0f4

Greene, J. E., Danieli, S., Carlsten, S., et al. 2022, arXiv e-prints, arXiv:2210.14237, doi: 10.48550/arXiv.2210.14237

Gunn, J. E., & Gott, J. Richard, I. 1972, ApJ, 176, 1, doi: 10.1086/151605

Guo, Q., White, S., Li, C., & Boylan-Kolchin, M. 2010, MNRAS, 404, 1111, doi: 10.1111/j.1365-2966.2010.16341.x

Hainline, K. N., Hickox, R. C., Carroll, C. M., et al. 2014, ApJ, 795, 124, doi: 10.1088/0004-637X/795/2/124

Häring, N., & Rix, H.-W. 2004, ApJL, 604, L89, doi: 10.1086/383567

Harrison, C. M., Costa, T., Tadhunter, C. N., et al. 2018, Nature Astronomy, 2, 198, doi: 10.1038/s41550-018-0403-6

Heckman, T. M., Alexandroff, R. M., Borthakur, S., Overzier, R., & Leitherer, C. 2015, ApJ, 809, 147, doi: 10.1088/0004-637X/809/2/147

Heckman, T. M., & Best, P. N. 2014, ARA&A, 52, 589, doi: 10.1146/annurev-astro-081913-035722

Heckman, T. M., Lehnert, M. D., Strickland , D. K., & Armus, L. 2000, ApJS, 129, 493, doi: 10.1086/313421

Hickox, R. C., & Alexander, D. M. 2018, ArXiv e-prints, arXiv:1806.04680. https://arxiv.org/abs/1806.04680

Hickox, R. C., Mullaney, J. R., Alexander, D. M., et al. 2014, ApJ, 782, 9, doi: 10.1088/0004-637X/782/1/9

Hickox, R. C., Myers, A. D., Greene, J. E., et al. 2017, ApJ, 849, 53, doi: 10.3847/1538-4357/aa8c77

Hickox, R. C., Jones, C., Forman, W. R., et al. 2007, ApJ, 671, 1365, doi: 10.1086/523082

—. 2009, ApJ, 696, 891, doi: 10.1088/0004-637X/696/1/891

Hickox, R. C., Myers, A. D., Brodwin, M., et al. 2011, ApJ, 731, 117, doi: 10.1088/0004-637X/731/2/117

Hopkins, P. F., Hernquist, L., Cox, T. J., & Kereš, D. 2008, The Astrophysical Journal Supplement Series, 175, 356, doi: 10.1086/524362

Hopkins, P. F., Quataert, E., & Murray, N. 2012, MNRAS, 421, 3522, doi: 10.1111/j.1365-2966.2012.20593.x

Hopkins, P. F., Somerville, R. S., Hernquist, L., et al. 2006, ApJ, 652, 864, doi: 10.1086/508503

Hopkins, P. F., Wetzel, A., Kereš, D., et al. 2018, MNRAS, 480, 800, doi: 10.1093/mnras/sty1690

Humphrey, A., Villar-Martín, M., Ramos Almeida, C., et al. 2015, MNRAS, 454, 4452, doi: 10.1093/mnras/stv2177

Impey, C., & Bothun, G. 1997, Annual Review of Astronomy and Astrophysics, 35, 267, doi: 10.1146/annurev.astro.35.1.267

Impey, C., Bothun, G., & Malin, D. 1988, ApJ, 330, 634, doi: 10.1086/166500

Ishibashi, W., & Fabian, A. C. 2022, MNRAS, 516, 4963, doi: 10.1093/mnras/stac2614

Ivezić, Ž., Kahn, S. M., Tyson, J. A., et al. 2019, ApJ, 873, 111, doi: 10.3847/1538-4357/ab042c

Jiang, F., Dekel, A., Freundlich, J., et al. 2019, MNRAS, 487, 5272, doi: 10.1093/mnras/stz1499

Joh, K., Nagao, T., Wada, K., Terao, K., & Yamashita, T. 2021, PASJ, 73, 1152, doi: 10.1093/pasj/psab065

Johnson, B. D., Leja, J., Conroy, C., & Speagle, J. S. 2021, ApJS, 254, 22, doi: 10.3847/1538-4365/abef67

Jones, M. G., Papastergis, E., Pandya, V., et al. 2018, A&A, 614, A21, doi: 10.1051/0004-6361/201732409

Jones, M. L., Hickox, R. C., Black, C. S., et al. 2016, ApJ, 826, 12, doi: 10.3847/0004-637X/826/1/12

Jones, M. L., Hickox, R. C., Mutch, S. J., et al. 2019, ApJ, 881, 110, doi: 10.3847/1538-4357/ab2d9f

Juneau, S., Dickinson, M., Alexander, D. M., & Salim, S. 2011, ApJ, 736, 104, doi: 10.1088/0004-637X/736/2/104

Karunakaran, A., & Zaritsky, D. 2023, MNRAS, 519, 884, doi: 10.1093/mnras/stac3622

Kauffmann, G., White, S. D. M., & Guiderdoni, B. 1993, MNRAS, 264, 201, doi: 10.1093/mnras/264.1.201

Kauffmann, G., Heckman, T. M., White, S. D. M., et al. 2003a, MNRAS, 341, 54, doi: 10.1046/j.1365-8711.2003.06292.x

—. 2003b, MNRAS, 341, 33, doi: 10.1046/j.1365-8711.2003.06291.x

Kelly, B. C., & Merloni, A. 2012, Advances in Astronomy, 2012, 970858, doi: 10.1155/2012/970858

Kennicutt, Robert C., J. 1998, ApJ, 498, 541, doi: 10.1086/305588

Kereš, D., Katz, N., Davé, R., Fardal, M., & Weinberg, D. H. 2009, MNRAS, 396, 2332, doi: 10.1111/j.1365-2966.2009.14924.x

Kewley, L. J., Groves, B., Kauffmann, G., & Heckman, T. 2006, MNRAS, 372, 961, doi: 10.1111/j.1365-2966.2006.10859.x

Kim, C.-G., & Ostriker, E. C. 2015, ApJ, 802, 99, doi: 10.1088/0004-637X/802/2/99

Kim, D. C., & Sanders, D. B. 1998, ApJS, 119, 41, doi: 10.1086/313148

King, A. 2005, ApJL, 635, L121, doi: 10.1086/499430

King, A., & Pounds, K. 2015, ARA&A, 53, 115, doi: 10.1146/annurev-astro-082214-122316

King, A. R. 2010, MNRAS, 408, L95, doi: 10.1111/j.1745-3933.2010.00938.x

Kocevski, D. D., Barro, G., Faber, S. M., et al. 2017, ApJ, 846, 112, doi: 10.3847/1538-4357/aa8566

Koda, J., Yagi, M., Yamanoi, H., & Komiyama, Y. 2015, ApJ, 807, L2, doi: 10.1088/2041-8205/807/1/L2

Komatsu, E., Smith, K. M., Dunkley, J., et al. 2011, ApJS, 192, 18, doi: 10.1088/0067-0049/192/2/18

Kong, D., Kaplinghat, M., Yu, H.-B., Fraternali, F., & Mancera Piña, P. E. 2022, ApJ, 936, 166, doi: 10.3847/1538-4357/ac8875

Koopmann, R. A., & Kenney, J. D. P. 2004, ApJ, 613, 866, doi: 10.1086/423191

Koprowski, M. P., Dunlop, J. S., Micha lowski, M. J., et al. 2017, MNRAS, 471, 4155, doi: 10.1093/mnras/stx1843

Kormendy, J., & Ho, L. C. 2013, Annual Review of Astronomy and Astrophysics, 51, 511, doi: 10.1146/annurev-astro-082708-101811

Krimm, H. A., Holland, S. T., Corbet, R. H. D., et al. 2013, The Astrophysical Journal Supplement Series, 209, 14, doi: 10.1088/0067-0049/209/1/14

Krumholz, M. R., & McKee, C. F. 2005, ApJ, 630, 250, doi: 10.1086/431734

Krumpe, M., Miyaji, T., Coil, A. L., & Aceves, H. 2012, ApJ, 746, 1, doi: 10.1088/0004-637X/746/1/1

Lamastra, A., Menci, N., Maiolino, R., Fiore, F., & Merloni, A. 2010, MNRAS, 405, 29, doi: 10.1111/j.1365-2966.2010.16439.x

Larson, R. B., Tinsley, B. M., & Caldwell, C. N. 1980, ApJ, 237, 692, doi: 10.1086/157917

Le Fèvre, O., Abraham, R., Lilly, S. J., et al. 2000, MNRAS, 311, 565, doi: 10.1046/j.1365-8711.2000.03083.x

Leighly, K. M. 2004, ApJ, 611, 125, doi: 10.1086/422089

Leisman, L., Haynes, M. P., Janowiecki, S., et al. 2017, ApJ, 842, 133, doi: 10.3847/1538-4357/aa7575

Leja, J., Carnall, A. C., Johnson, B. D., Conroy, C., & Speagle, J. S. 2019, ApJ, 876, 3, doi: 10.3847/1538-4357/ab133c

Lewis, A., Challinor, A., & Lasenby, A. 2000, ApJ, 538, 473, doi: 10.1086/309179

Li, J., Greene, J. E., Greco, J., et al. 2023, arXiv e-prints, arXiv:2302.14108, doi: 10.48550/arXiv.2302.14108

Li, J., Greene, J. E., Greco, J. P., et al. 2022, arXiv e-prints, arXiv:2210.14994, doi: 10.48550/arXiv.2210.14994

Liao, S., Gao, L., Frenk, C. S., et al. 2019, MNRAS, 490, 5182, doi: 10.1093/mnras/stz2969

Lin, L., Cooper, M. C., Jian, H.-Y., et al. 2010, ApJ, 718, 1158, doi: 10.1088/0004-637X/718/2/1158

Lonsdale, C. J., Farrah, D., & Smith, H. E. 2006, Ultraluminous Infrared Galaxies, ed. J. W. Mason, 285, doi: 10.1007/3-540-30313-8_9

Lotz, J. M., Jonsson, P., Cox, T. J., et al. 2011, ApJ, 742, 103, doi: 10.1088/0004-637X/742/2/103

Lotz, J. M., Jonsson, P., Cox, T. J., & Primack, J. R. 2008, MNRAS, 391, 1137, doi: 10.1111/j.1365-2966.2008.14004.x

Luo, B., Brandt, W. N., Hall, P. B., et al. 2015, ApJ, 805, 122, doi: 10.1088/0004-637X/805/2/122

Lusso, E., & Risaliti, G. 2016, ApJ, 819, 154, doi: 10.3847/0004-637X/819/2/154

Madau, P., & Dickinson, M. 2014, ARA&A, 52, 415, doi: 10.1146/annurev-astro-081811-125615

Magnelli, B., Elbaz, D., Chary, R. R., et al. 2009, A&A, 496, 57, doi: 10.1051/0004-6361:200811443

—. 2011, A&A, 528, A35, doi: 10.1051/0004-6361/200913941

Mancera Piña, P. E., Fraternali, F., Oman, K. A., et al. 2020, MNRAS, 495, 3636, doi: 10.1093/mnras/staa1256

Mao, Y.-Y., Geha, M., Wechsler, R. H., et al. 2021, ApJ, 907, 85, doi: 10.3847/1538-4357/abce58

Marshall, J. L., Burles, S., Thompson, I. B., et al. 2008, in Society of Photo-Optical Instrumentation Engineers (SPIE) Conference Series, Vol. 7014, Ground-based and Airborne Instrumentation for Astronomy II, ed. I. S. McLean & M. M. Casali, 701454, doi: 10.1117/12.789972

Martínez-Delgado, D., Läsker, R., Sharina, M., et al. 2016, AJ, 151, 96, doi: 10.3847/0004-6256/151/4/96

McGaugh, S. S., Schombert, J. M., & Lelli, F. 2017, ApJ, 851, 22, doi: 10.3847/1538-4357/aa9790

McKee, C. F., & Ostriker, E. C. 2007, ARA&A, 45, 565, doi: 10.1146/annurev.astro.45.051806.110602

McNamara, B. R., & Nulsen, P. E. J. 2007, ARA&A, 45, 117, doi: 10.1146/annurev.astro.45.051806.110625

—. 2012a, New Journal of Physics, 14, 055023, doi: 10.1088/1367-2630/14/5/055023

—. 2012b, New Journal of Physics, 14, 055023, doi: 10.1088/1367-2630/14/5/055023

Melchior, P., Moolekamp, F., Jerdee, M., et al. 2018, Astronomy and Computing, 24, 129, doi: 10.1016/j.ascom.2018.07.001

Merloni, A., Bongiorno, A., Brusa, M., et al. 2014, MNRAS, 437, 3550, doi: 10.1093/mnras/stt2149

Metropolis, N., Rosenbluth, A. W., Rosenbluth, M. N., Teller, A. H., & Teller, E. 1953, JChPh, 21, 1087, doi: 10.1063/1.1699114

Mihos, J. C. 2004, in Clusters of Galaxies: Probes of Cosmological Structure and Galaxy Evolution, ed. J. S. Mulchaey, A. Dressler, & A. Oemler, 277

Mihos, J. C., & Hernquist, L. 1996, ApJ, 464, 641, doi: 10.1086/177353

Miyazaki, S., Komiyama, Y., Nakaya, H., et al. 2012, in Society of Photo-Optical Instrumentation Engineers (SPIE) Conference Series, Vol. 8446, Ground-based and Airborne Instrumentation for Astronomy IV, ed. I. S. McLean, S. K. Ramsay, & H. Takami, 84460Z, doi: 10.1117/12.926844

Miyazaki, S., Komiyama, Y., Kawanomoto, S., et al. 2018, PASJ, 70, S1, doi: 10.1093/pasj/psx063

Moster, B. P., Somerville, R. S., Maulbetsch, C., et al. 2010, ApJ, 710, 903, doi: 10.1088/0004-637X/710/2/903

Mould, J. R., Huchra, J. P., Freedman, W. L., et al. 2000, ApJ, 529, 786, doi: 10.1086/308304

Moustakas, J., Coil, A. L., Aird, J., et al. 2013, ApJ, 767, 50, doi: 10.1088/0004-637X/767/1/50

Mowla, L. A., van Dokkum, P., Brammer, G. B., et al. 2019, ApJ, 880, 57, doi: 10.3847/1538-4357/ab290a

Murphy, T. W., J., Soifer, B. T., Matthews, K., & Armus, L. 2001, ApJ, 559, 201, doi: 10.1086/322321

Murray, N., Ménard, B., & Thompson, T. A. 2011, ApJ, 735, 66, doi: 10.1088/0004-637X/735/1/66

Myers, A. D., Brunner, R. J., Nichol, R. C., et al. 2007, ApJ, 658, 85, doi: 10.1086/511519

Naab, T., Johansson, P. H., & Ostriker, J. P. 2009, ApJL, 699, L178, doi: 10.1088/0004-637X/699/2/L178

Nashimoto, M., Tanaka, M., Chiba, M., et al. 2022, ApJ, 936, 38, doi: 10.3847/1538-4357/ac83a4

Nelson, D., Pillepich, A., Springel, V., et al. 2019, MNRAS, 490, 3234, doi: 10.1093/mnras/stz2306

Netzer, H. 2015, Annual Review of Astronomy and Astrophysics, 53, 365, doi: 10.1146/annurev-astro-082214-122302

Netzer, H., & Trakhtenbrot, B. 2014, MNRAS, 438, 672, doi: 10.1093/mnras/stt2238

Newberg, H. J., & Yanny, B. 1997, ApJS, 113, 89, doi: 10.1086/313051

Newman, A. B., Ellis, R. S., Bundy, K., & Treu, T. 2012, ApJ, 746, 162, doi: 10.1088/0004-637X/746/2/162

Nogueira-Cavalcante, J. P., Gonçalves, T. S., Menéndez-Delmestre, K., & Sheth, K. 2018, MNRAS, 473, 1346, doi: 10.1093/mnras/stx2399

Oemler, Augustus, J., Abramson, L. E., Gladders, M. D., et al. 2017, ApJ, 844, 45, doi: 10.3847/1538-4357/aa789e

Oke, J. B., Cohen, J. G., Carr, M., et al. 1995, PASP, 107, 375, doi: 10.1086/133562

Ostriker, J. P., Choi, E., Ciotti, L., Novak, G. S., & Proga, D. 2010, ApJ, 722, 642, doi: 10.1088/0004-637X/722/1/642

Padovani, P., Alexander, D. M., Assef, R. J., et al. 2017, Astronomy and Astrophysics Review, 25, 2, doi: 10.1007/s00159-017-0102-9

Pakmor, R., Springel, V., Coles, J. P., et al. 2022, arXiv e-prints, arXiv:2210.10060, doi: 10.48550/arXiv.2210.10060

Pannella, M., Carilli, C. L., Daddi, E., et al. 2009, ApJL, 698, L116, doi: 10.1088/0004-637X/698/2/L116

Pattarakijwanich, P., Strauss, M. A., Ho, S., & Ross, N. P. 2016, ApJ, 833, 19, doi: 10.3847/0004-637X/833/1/19

Patton, D. R., Wilson, K. D., Metrow, C. J., et al. 2020, MNRAS, 494, 4969, doi: 10.1093/mnras/staa913

Pérez-González, P. G., Rieke, G. H., Villar, V., et al. 2008, ApJ, 675, 234, doi: 10.1086/523690

Pérez-Millán, D., Fritz, J., González-Lópezlira, R. A., et al. 2023, MNRAS, 521, 1292, doi: 10.1093/mnras/stad542

Perrotta, S., George, E. R., Coil, A. L., et al. 2021, arXiv e-prints, arXiv:2106.02366. https://arxiv.org/abs/2106.02366

Peterson, B. M., Ferrarese, L., Gilbert, K. M., et al. 2004, ApJ, 613, 682, doi: 10.1086/423269

Petter, G. C., Kepley, A. A., Hickox, R. C., et al. 2020, ApJ, 901, 138, doi: 10.3847/1538-4357/abb19d

Polletta, M., Weedman, D., Hönig, S., et al. 2008, ApJ, 675, 960, doi: 10.1086/524343

Powell, M. C., Cappelluti, N., Urry, C. M., et al. 2018, ApJ, 858, 110, doi: 10.3847/1538-4357/aabd7f

Predehl, P., & Schmitt, J. H. M. M. 1995, A&A, 500, 459

Prescott, M. K. M., Dey, A., & Jannuzi, B. T. 2012, ApJ, 748, 125, doi: 10.1088/0004-637X/748/2/125

Quai, S., Hani, M. H., Ellison, S. L., Patton, D. R., & Woo, J. 2021, MNRAS, 504, 1888, doi: 10.1093/mnras/stab988

Ramos Almeida, C., & Ricci, C. 2017, Nature Astronomy, 1, 679, doi: 10.1038/s41550-017-0232-z

Raskutti, S., Ostriker, E. C., & Skinner, M. A. 2017, ApJ, 850, 112, doi: 10.3847/1538-4357/aa965e

Ricci, C., Trakhtenbrot, B., Koss, M. J., et al. 2017, Nature, 549, 488, doi: 10.1038/nature23906

Richards, G. T., Fan, X., Newberg, H. J., et al. 2002, AJ, 123, 2945, doi: 10.1086/340187

Richards, G. T., Strauss, M. A., Fan, X., et al. 2006, AJ, 131, 2766, doi: 10.1086/503559

Riechers, D. A., Pavesi, R., Sharon, C. E., et al. 2019, ApJ, 872, 7, doi: 10.3847/1538-4357/aafc27

Rix, H.-W., Barden, M., Beckwith, S. V. W., et al. 2004, ApJS, 152, 163, doi: 10.1086/420885

Román, J., & Trujillo, I. 2017, MNRAS, 468, 4039, doi: 10.1093/mnras/stx694

Rong, Y., Guo, Q., Gao, L., et al. 2017, MNRAS, 470, 4231, doi: 10.1093/mnras/stx1440

Ross, N. P., Shen, Y., Strauss, M. A., et al. 2009, ApJ, 697, 1634, doi: 10.1088/0004-637X/697/2/1634

Ruiz-Lara, T., Gallart, C., Beasley, M., et al. 2018, A&A, 617, A18, doi: 10.1051/0004-6361/201732398

Rupke, D. 2018, Galaxies, 6, 138, doi: 10.3390/galaxies6040138

Rupke, D. S. N., Coil, A., Geach, J. E., et al. 2019, Nature, 574, 643, doi: 10.1038/s41586-019-1686-1

Sales, L. V., Wetzel, A., & Fattahi, A. 2022, Nature Astronomy, 6, 897, doi: 10.1038/s41550-022-01689-w

Sanders, D. B., Soifer, B. T., Elias, J. H., et al. 1988, ApJ, 325, 74, doi: 10.1086/165983

Schawinski, K., Urry, C. M., Simmons, B. D., et al. 2014, MNRAS, 440, 889, doi: 10.1093/mnras/stu327

Schmidt, M. 1959, ApJ, 129, 243, doi: 10.1086/146614

Schnorr-Müller, A., Davies, R. I., Korista, K. T., et al. 2016, MNRAS, 462, 3570, doi: 10.1093/mnras/stw1865

Science Software Branch at STScI. 2012, PyRAF: Python alternative for IRAF, Astrophysics Source Code Library, record ascl:1207.011. http://ascl.net/1207.011

Sell, P. H., Tremonti, C. A., Hickox, R. C., et al. 2014, MNRAS, 441, 3417, doi: 10.1093/mnras/stu636

Setton, D. J., Bezanson, R., Suess, K. A., et al. 2020, arXiv e-prints, arXiv:2010.04734. https://arxiv.org/abs/2010.04734

Shakura, N. I., & Sunyaev, R. A. 1973, A&A, 24, 337

Shankar, F., Weinberg, D. H., & Miralda-Escudé, J. 2009, ApJ, 690, 20, doi: 10.1088/0004-637X/690/1/20

Shen, Y., Strauss, M. A., Oguri, M., et al. 2007, AJ, 133, 2222, doi: 10.1086/513517

Shen, Y., Strauss, M. A., Ross, N. P., et al. 2009, ApJ, 697, 1656, doi: 10.1088/0004-637X/697/2/1656

Shi, Y., Yan, L., Armus, L., et al. 2018, ApJ, 853, 149, doi: 10.3847/1538-4357/aaa3e6

Sifón, C., van der Burg, R. F. J., Hoekstra, H., Muzzin, A., & Herbonnet, R. 2018, MNRAS, 473, 3747, doi: 10.1093/mnras/stx2648

Silk, J., & Rees, M. J. 1998, A&A, 331, L1

Simon, J. D. 2019, ARA&A, 57, 375, doi: 10.1146/annurev-astro-091918-104453

Smith, M. P., Nordsieck, K. H., Burgh, E. B., et al. 2006, in Society of Photo-Optical Instrumentation Engineers (SPIE) Conference Series, Vol. 6269, Society of Photo-Optical Instrumentation Engineers (SPIE) Conference Series, ed. I. S. McLean & M. Iye, 62692A, doi: 10.1117/12.672415

Somerville, R. S., & Davé, R. 2015, ARA&A, 53, 51, doi: 10.1146/annurev-astro-082812-140951

Springel, V., Di Matteo, T., & Hernquist, L. 2005a, MNRAS, 361, 776, doi: 10.1111/j.1365-2966.2005.09238.x

Springel, V., & Hernquist, L. 2003, MNRAS, 339, 312, doi: 10.1046/j.1365-8711.2003.06207.x

Springel, V., White, S. D. M., Jenkins, A., et al. 2005b, Nature, 435, 629, doi: 10.1038/nature03597

Stefanon, M., Marchesini, D., Rudnick, G. H., Brammer, G. B., & Whitaker, K. E. 2013, ApJ, 768, 92, doi: 10.1088/0004-637X/768/1/92

Stern, D., Assef, R. J., Benford, D. J., et al. 2012, ApJ, 753, 30, doi: 10.1088/0004-637X/753/1/30

Stott, J. P., Sobral, D., Smail, I., et al. 2013, MNRAS, 430, 1158, doi: 10.1093/mnras/sts684

Strauss, M. A., Weinberg, D. H., Lupton, R. H., et al. 2002, AJ, 124, 1810, doi: 10.1086/342343

Tacconi, L. J., Genzel, R., Neri, R., et al. 2010, Nature, 463, 781, doi: 10.1038/nature08773

Tacconi, L. J., Neri, R., Genzel, R., et al. 2013, ApJ, 768, 74, doi: 10.1088/0004-637X/768/1/74

Taylor, E. N., Franx, M., Glazebrook, K., et al. 2010, ApJ, 720, 723, doi: 10.1088/0004-637X/720/1/723

Thompson, T. A., Quataert, E., & Murray, N. 2005, ApJ, 630, 167, doi: 10.1086/431923

Thornley, M. D., Förster Schreiber, N. M., Lutz, D., et al. 2000, ApJ, 539, 641, doi: 10.1086/309261

Tinker, J. L., Robertson, B. E., Kravtsov, A. V., et al. 2010, ApJ, 724, 878, doi: 10.1088/0004-637X/724/2/878

Toomre, A. 1977, in Evolution of Galaxies and Stellar Populations, ed. B. M. Tinsley & D. C. Larson, Richard B. Gehret, 401

Treister, E., Krolik, J. H., & Dullemond, C. 2008, ApJ, 679, 140, doi: 10.1086/586698

Treister, E., Schawinski, K., Urry, C. M., & Simmons, B. D. 2012, ApJL, 758, L39, doi: 10.1088/2041-8205/758/2/L39

Tremmel, M., Wright, A. C., Brooks, A. M., et al. 2020, MNRAS, 497, 2786, doi: 10.1093/mnras/staa2015

Tremonti, C. A., Moustakas, J., & Diamond-Stanic, A. a. M. 2007, ApJL, 663, L77, doi: 10.1086/520083

Tremonti, C. A., Heckman, T. M., Kauffmann, G., et al. 2004, ApJ, 613, 898, doi: 10.1086/423264

Tremonti et al., C. in prep, ApJ

Urry, C. M., & Padovani, P. 1995, Publications of the Astronomical Society of the Pacific, 107, 803, doi: 10.1086/133630

Usman, S. M., Murray, S. S., Hickox, R. C., & Brodwin, M. 2014, ApJL, 788, L3, doi: 10.1088/2041-8205/788/1/L3

van der Burg, R. F. J., Muzzin, A., & Hoekstra, H. 2016, A&A, 590, A20, doi: 10.1051/0004-6361/201628222

van der Burg, R. F. J., Hoekstra, H., Muzzin, A., et al. 2017, A&A, 607, A79, doi: 10.1051/0004-6361/201731335

van der Wel, A., Franx, M., van Dokkum, P. G., et al. 2014, ApJ, 788, 28, doi: 10.1088/0004-637X/788/1/28

van Dokkum, P. G., Abraham, R., Merritt, A., et al. 2015a, ApJ, 798, L45, doi: 10.1088/2041-8205/798/2/L45

van Dokkum, P. G., Franx, M., Kriek, M., et al. 2008, ApJL, 677, L5, doi: 10.1086/587874

van Dokkum, P. G., Nelson, E. J., Franx, M., et al. 2015b, ApJ, 813, 23, doi: 10.1088/0004-637X/813/1/23

van Gorkom, J. H. 2004, in Clusters of Galaxies: Probes of Cosmological Structure and Galaxy Evolution, ed. J. S. Mulchaey, A. Dressler, & A. Oemler, 305. https://arxiv.org/abs/astro-ph/0308209

Vanden Berk, D. E., Schneider, D. P., Richards, G. T., et al. 2005, AJ, 129, 2047, doi: 10.1086/427856

Veale, M., White, M., & Conroy, C. 2014, MNRAS, 445, 1144, doi: 10.1093/mnras/stu1821

Veilleux, S., Cecil, G., & Bland-Hawthorn, J. 2005, ARA&A, 43, 769, doi: 10.1146/annurev.astro.43.072103.150610

Veilleux, S., Maiolino, R., Bolatto, A. D., & Aalto, S. 2020, A&A Rv, 28, 2, doi: 10.1007/s00159-019-0121-9

Villaume, A., Conroy, C., & Johnson, B. D. 2015, ApJ, 806, 82, doi: 10.1088/0004-637X/806/1/82

Vogelsberger, M., Genel, S., Springel, V., et al. 2014, MNRAS, 444, 1518, doi: 10.1093/mnras/stu1536

Vulcani, B., Poggianti, B. M., Fritz, J., et al. 2015, ApJ, 798, 52, doi: 10.1088/0004-637X/798/1/52

Weinberg, D. H., Bullock, J. S., Governato, F., Kuzio de Naray, R., & Peter, A. H. G. 2015, Proceedings of the National Academy of Science, 112, 12249, doi: 10.1073/pnas.1308716112

Werner, M. W., Roellig, T. L., Low, F. J., et al. 2004, The Astrophysical Journal Supplement Series, 154, 1, doi: 10.1086/422992

Whitaker, K. E., Pope, A., Cybulski, R., et al. 2017, ApJ, 850, 208, doi: 10.3847/1538-4357/aa94ce

Whitaker, K. E., Labbé, I., van Dokkum, P. G., et al. 2011, ApJ, 735, 86, doi: 10.1088/0004-637X/735/2/86

Wild, V., Almaini, O., Dunlop, J., et al. 2016, MNRAS, 463, 832, doi: 10.1093/mnras/stw1996

Wild, V., Charlot, S., Brinchmann, J., et al. 2011, MNRAS, 417, 1760, doi: 10.1111/j.1365-2966.2011.19367.x

Wild, V., Walcher, C. J., Johansson, P. H., et al. 2009, MNRAS, 395, 144, doi: 10.1111/j.1365-2966.2009.14537.x

Woo, J.-H., Treu, T., Malkan, M. A., & Blandford, R. D. 2008, ApJ, 681, 925, doi: 10.1086/588804

Wright, E. L., Eisenhardt, P. R. M., Mainzer, A. K., et al. 2010, AJ, 140, 1868, doi: 10.1088/0004-6256/140/6/1868

Yan, W., Hickox, R. C., Hainline, K. N., et al. 2019, ApJ, 870, 33, doi: 10.3847/1538-4357/aaeed4

York, D. G., Adelman, J., Anderson, John E., J., et al. 2000, AJ, 120, 1579, doi: 10.1086/301513

Yozin, C., & Bekki, K. 2015, MNRAS, 453, 2302, doi: 10.1093/mnras/stv1828

Zaritsky, D., Donnerstein, R., Karunakaran, A., et al. 2021, ApJS, 257, 60, doi: 10.3847/1538-4365/ac2607

—. 2022, ApJS, 261, 11, doi: 10.3847/1538-4365/ac6ceb

Zhang, D. 2018, Galaxies, 6, 114, doi: 10.3390/galaxies6040114

Zhuang, M.-Y., & Ho, L. C. 2020, ApJ, 896, 108, doi: 10.3847/1538-4357/ab8f2e

Zinger, E., Pillepich, A., Nelson, D., et al. 2020, MNRAS, 499, 768, doi: 10.1093/mnras/staa2607

Zirm, A. W., van der Wel, A., Franx, M., et al. 2007, ApJ, 656, 66, doi: 10.1086/510713